UNIVERSITÀ
DEGLI STUDI
DI PADOVA

Sede Amministrativa: Università degli Studi di Padova
CISAS Centro di Ateneo di Studi e Attività Spaziali G. Colombo

SCUOLA DI DOTTORATO DI RICERCA IN : SCIENZE TECNOLOGIE E MISURE SPAZIALI
INDIRIZZO: SCIENZE E TECNOLOGIE PER APPLICAZIONI SATELLITARI ED AERONAUTICHE
CICLO XXVIII

DEVELOPMENT OF GLOBAL MODELS OF PLASMA SYSTEMS FOR SPACE PROPULSION

Direttore della Scuola : Ch.mo Prof. Giampiero Naletto
Coordinatore d'indirizzo: Ch.mo Prof. Giampiero Naletto
Supervisore: Ch.mo Prof. Daniele Pavarin

Dottorando : Franco Javier Bosi

Abstract

The focus of this research work is to develop plasma global models, to support the investigations on argon and carbon dioxide helicon plasma thruster, carried out at CISAS research center. These models have been applied in three different and consecutive research programs, the EU FP7 HpH.com program, the AO7048 ESA program, and the SAPERE-STRONG MIUR program.

The models have been developed for the most general case of an electronegative magnetized discharge, therefore encompass all types of cold non magnetized or electropositive discharges. Furthermore, the models employs results from particle in cell simulations of the plasma exhaust plume, in order to account properly for the plasma detachment and acceleration provided by the so called magnetic nozzle effect. The simulations are in agreement with performed experiments on the laboratory set up, and allow prediction of the thruster propulsive performances.

The viability of plasma assisted combustion for monopropellant propulsion applications, is also investigated. An experimental proof of concept is provided with a nitrous oxide gliding arc experiment, carried out at Drexel Plasma Institute. The experiment shows that the plasma is effective in promoting catalytic decomposition and combustion of the gas.

A global model is developed to investigate the mechanism of nitrous oxide plasma assisted dissociation; the model implements non-equilibrium neutral gas phase reaction rates and a vibrational energy equation for the estimation of the vibrational temperature. The model is able to reveal the mechanism of plasma catalysis, and predicts good performances for an hypothetical nitrous oxide microwave discharge thruster.

Sommario

Obiettivo di questo lavoro è lo sviluppo di modelli globali di plasma atti a supportare lo studio della propulsione al plasma di tipo helicon, con propellente ad argon e anidride carbonica, portato avanti al centro di ricerca ed attività spaziali CISAS. I modelli sono stati applicati in tre progetti di ricerca consecutivi: il progetto HpH.com, finanziato nel contesto del programma europeo FP7, il progetto AO7048 finanziato da ESA ed il progetto STRONG-SAPERE finanziato dal MIUR.

I modelli sono sviluppati in via generale per plasmi di gas elettronegativo e magnetizzato, perciò sono applicabili alle sottocategorie di plasmi freddi, non magnetizzati o elettropositivi.

I modelli inoltre, incorporano risultati da simulazioni di tipo *paticle in cell*, della zona del plume del propulsore; in questo modo è possibile tener conto degli effetti di distacco e accelerazione del plasma, provocati dalla divergenza delle linee del campo magnetico; il cosidetto effetto di ugello magnetico.

E' inoltre studiata la fattibilità della combustione assistita da plasma, per applicazioni relative a propulsione monopropellente. Una verifica sperimentale di fattibilità è effettuata attraverso un esperimento di scarica di tipo gliding arc, di protossido d'azoto; l'esperimento è stato effettuato presso il Drexel Plasma Institute a Philadelphia.

Un modello globale di plasma è stato sviluppato per studiare i meccanismi della dissociazione assistita da plasma; il modello implementa reazioni di fase neutra di non equilibrio, e una equazione per l'evoluzione dell'energia vibrazionale delle molecole, che permette di tracciare l'andamento temporale della temperatura vibrazionale. Il modello è in grado di evidenziare i meccanismi di catalisi da plasma; inoltre, predice buone prestazioni per un eventuale propulsore di tipo plasma a microonde con protossido d'azoto.

Acknowledgements

I am using this opportunity to express my gratitude to everyone who supported me throughout the course of this PhD. I am thankful to my supervisor Daniele Pavarin and the guys from the lab, Marco, Davide and Fabio, who helped and advised me.

I'd like to thanks also professor Danil Dobrynin for the opportunity to spend a research period at Plasma Drexel Institute, and for the support during that experience.

A special thanks to Gary Nirenberg, pillar of the Drexel Plasma Institute, a patient and invaluable teacher.

Contents

List of Figures

List of Tables

Chapter 1

Introduction

In this thesis a series of plasma global models are presented; the work is performed in the framework of plasma propulsion, and the models are developed in order to support the investigations on argon and carbon dioxide helicon plasma thruster, carried out at CISAS research center.

1.1 Electric Propulsion Overview

Electric propulsion is a technology aimed at achieving thrust with high exhaust velocities, which results in a reduction in the amount of propellant required for a given space mission or application compared to other conventional propulsion methods; plasma propulsion uses electric energy to ionize the propellant and then impart kinetic energy to the resulting plasma. The primary attraction of electric propulsion is related to the high exhaust velocity, c_{ex}, of the propellant which gives an efficient utilization of the propellant mass. The propellant mass m_p required for a spacecraft to acquire a velocity increment Δv is given by the Tsiolkovsky equation:

$$\frac{m_p}{m_0} = 1 - \exp\left(-\frac{\Delta v}{c_e x}\right) \tag{1.1}$$

where m_0 is the spacecraft mass at the initial time; therefore high exhaust velocity reduce the mass cost of the mission, and for this reason electric propulsion has been studied for more than half a century; first flying electric thrusters date back to early 1960. The acceleration of the gas can be accomplished in many ways, and so plasma thrusters fall into different categories, mainly *electrostatic, electromagnetic or electrothermal.*

In electrostatic propulsion the propellant is ionized and accelerated through electrostatic forces, the chief example of these devices, and one of the first developed, is the ion thruster. In electromagnetic propulsion the ionized propellant is accelerated through the interactions between electrical currents and external or internal magnetic fields; in this category falls the Hall thruster, which is the major competitor of the ion thruster. In an electrothermal thruster the acceleration is provided by expansion of the gas through a nozzle, after being heated by an electrical source.

During the years many different concept of electric propulsion have been proposed and developed, partly to explore new capabilities of plasma devices, overcome limitations and extend the performances of existing models; in this regard there has been a recent development of plasma helicon sources for plasma propulsion applications.

Helicon sources are high ionization efficiency, cold plasma sources, developed for plasma industrial processing in the last two decades; this type of source is based on RF wave heating of the electrons, and subsequent ionization of the gas, in a cylindrical, axially magnetized plasma column. The excitation frequency lies typically in the range 1-50 MHz, with axial magnetization from 100-1000 Gauss, depending on operating conditions, and plasma densities from 10^{17} m^{-3} to 10^{19} m^{-3}.

1.2 Helicon Sources and HPT Thruster

In the helicon plasma thruster (HPT) concept, the gas is injected in a dielectric tube (made of quartz normally) wrapped by an RF excitation antenna, surrounded by coils or permanent magnets, which generates a magnetic field. The magnetic field serves different purposes, it allows propagation of the helicon waves and provides electron confinement in order to reduce losses.

The acceleration stage is provided by the natural electrostatic potential drop, at the boundary of the source ionization region, and by the divergence of the magnetic field lines in the plasma plume, the so-called magnetic nozzle effect. However,the magnetic field lines close themselves on the spacecraft structure, therefore plasma detachment becomes a critical issue in order to provide net momentum[2].

Acceleration grid erosion is a lifetime-limiting process in ion thrusters as is wall and cathode erosion in Hall thrusters; the HPT concept bypass these critical issues: the absence of electrodes, which bypass the problem of electrodes erosion, the absence of cathode emitters, since the beam expelled by the thruster is composed by electron-ion pairs, and the absence of acceleration grids.

There are several research projects, investigating the HPT concept, in Australia[3], USA[2], Europe[4] and Japan[5]; the Research Center for Space Studies and Activities (CISAS) has been investigating and developing helicon plasma propulsion systems since 2008, in the contest of three different, and consecutive, projects: the HpH.com project, the AO7048 project and the STRONG-SAPERE project.

1.3 HPT Investigation Carried at CISAS

The *Helicon Plasma Hydrazine.Combined Micro* (HpH.com) is a research project funded by the European Union within the 7th Framework Program and conducted by an international consortium during the period 2008 - 2012. It was devoted to the development of a plasma thruster, based on helicon-RF technology, for low thrust (1 mN) attitude control operations, at low power (50 W), using Argon as propellant. Moreover, a detailed feasibility study was performed to evaluate the possibility of using the plasma thruster to heat and decompose a secondary propellant (Nitrous oxide or Hydrazine) in order to develop a two mode thruster, characterized by an high-efficiency low-thrust plasma thruster mode and a low-efficiency high-trust secondary propellant plasma-enhanced mode.

The HPT is potentially suited for a variety of applications; scalability, throttability, versatility appear to be its major characteristics; in this perspective the project *Helicon Plasma Thruster for Space Missions* - AO7048, funded by the European Space Agency, started from the output of the HpH.com program; the project was carried out from 2012 to 2014, among the purposes of the project was the investigation of the behaviour of the thruster with different propellants, applicable to different mission scenarios, like utilization of the thruster with waste gases from the International Space Station (ISS), or utilization of the thruster with gases from planetary atmospheres (atmospheric breeding concept), during low orbit mission configurations. Indeed the use of the HPT thruster with molecular gases, have interested also other research groups, which have published studies on the subject[3, 6].

The AO7048 project identified carbon dioxide as gas with good propulsive performances. Furthermore, the use of the thruster with CO_2 is interesting for potential mission scenarios involving the ISS and the exploration of planet Mars, which has recently come to the attention of the space community. The *STRONG-SAPERE* program, funded by the Italian Ministry for University and Research (MIUR), and under development from 2015, starts from the results of the previous AO7048 and HpH.com programs and aims to develop a prototype of a high power HPT thruster working with Ar and CO_2.

Several numerical tools have been developed, within our research lab, in order to study the HPT discharge and its properties, for optimization purposes and to foresee performances, in parameter ranges and configurations not yet experimentally available. Particle in cell (PIC) simulations have been the numerical tool devoted to the study of the exhaust plume, a region characterized by complex interaction between particles, high electric fields and magnetic fields. The results of those analysis have been embedded within global plasma models, dedicated to the study of the variation of the discharge properties with its configuration parameters, i.e. gas flow rate, electrical power input and so on, in order to assess feasibility and propulsive performances.

1.4 Global Models

Global models have become popular tools in the last two decades[7], they have proven to be predictable, within a few multiplicative factors, and they are widely used to study discharges of many types[8–10].

In a volume average model densities and temperatures are spatially averaged and only their time dependency is considered. The spatial variation of the physical quantities, is accounted for by means of semi-empirical, and analytical, solutions of diffusion equations. This simplified mathematical environment, makes global models the ideal place for implementation of complex chemistry and plasma processes, making it the preferred tool of chemist and spectroscopist. Indeed, despite this apparent simplicity, global models can embeds hundreds or thousands of reactions, leading to strenuous literature compilation works.

We developed global average models in order to investigate the behaviour and performances of the plasma thruster fed with different gases. The models account for electronegativity and magnetization of the gas, in certain conditions neutral energy equation is implemented for estimation of the molecular gas temperature within the discharge. The model solutions allow tracking of the propulsive parameters and the discharge species densities and temperatures. Furthermore, the developed numerical models can be generalized to applications other than electric propulsion, such as plasma surface processing, waste treatment, and so on.

The nitrous oxide and hydrazine plasma ignition study, performed during the HpH.com, and reported in [11], triggered a study of the viability of the plasma as continuous acting catalyst, for nitrous oxide monopropellant propulsion (150-250 s specific impulse, 50-500 mN thrust range). Monopropellant thrusters are widely used in spacecraft attitude

control and station keeping for satellites. Hydrazine and hydrogen peroxide are among the most used in such propulsion systems and are a proven technology.

In recent years, researchers have committed into finding a green alternative to these propellants, because their toxicity and inherent flammability make them difficult and costly to handle[12, 13]. Nitrous oxide offers many inherent advantages as small satellite's propellant. It is non-toxic, non-corrosive and may be used with common structural materials. Indeed another research group[14], in the US, is working on the concept of a DBD plasma catalysis decomposition of N_2O for monopropellant propulsion applications.

In this thesis an experimental, preliminary, proof of concept of the beneficial plasma catalysis of N_2O is presented; furthermore, a global model is presented for the numerical investigation of the N_2O plasma assisted dissociation, that implements non-equilibrium neutral gas phase reaction rates and a vibrational energy equation for the estimation of the vibrational temperature.

1.5 Objectives

The main objective of this thesis is the development of global models to aid the HPT investigation carried out at CISAS. For this purpose an extensive literature review has been necessary, not only to retrieve all the available and relevant plasma-chemical processes to input in the discharge models, but also to verify the values of the reaction rates, some times reported erroneously in more recent literature.

Experimental measurements of the electron density and spectroscopic estimations of electron temperature are performed in order to gain confidence with the models; at this point we must point out that, unlike the electron density measurements, the estimation of electron temperatures, by means of optical emission spectroscopy, are subject to the inherent spectroscopic models uncertainties, that will always be; therefore electron temperature estimations are given, here, in a qualitative way.

Experimental proof of concept of the viability of plasma assisted combustion, as a mean to promote dissociation of N_2O for monopropellant applications is given; a global model is developed to investigate the plasma-chemical decomposition of N_2O in non equilibrium conditions, with vibrational temperature higher than gas temperature.

1.6 Thesis Outline

The thesis organization is briefly summarized:

- Chapter [2] presents the numerical global model in the general case, not dependent from the gas; the chapter describes the model input and output, discharge parameters, continuity and energy equations. Bulk plasma processes, wall diffusion of charge and neutrals and assessment of the exhaust beam produced by the thruster, are described, together with the respective assumptions and the relevant references.

- Chapter [3] enters the details pertaining to the considered gases: first the Ar thruster model, then the multi-species thruster model and the CO_2 thruster model at the end. A comparison with other helicon sources is performed based on a source efficiency parameter; the agreement of the Ar and CO_2 models with the experiments, and the influence of the discharge parameters is discussed; propulsive performances are presented.

- Chapter [4] describes the numerical characterization of the Ar and CO_2 discharges; electron density measurements and electron temperature estimations.

- Chapter [5] presents, in the first part, an experimental proof of concept of for N_2O plasma assisted decomposition, obtained with a gliding arc discharge; in the second part a global model is derived for numerical investigation purposes; the model employs an additional vibrational energy equation and a set of non equilibrium neutral gas phase reactions. The model, though its purpose its theoretical, can be applied to microwave N_2O discharges.

Chapter 2

Numerical Model

Global models have become popular tools in the last two decades[7], they have proven to be predictable, within a few multiplicative factors, and they are widely used to study discharges of many types[8–10], inductively coupled, capacitively coupled, hollow cathodes, *etc.* In a volume average model densities and temperatures are spatially averaged and only their time dependency is considered. We developed a global average model in order to investigate the behaviour and performances of the plasma thruster fed with different gases. The thruster geometry is a cylindrical chamber with an inflow section and an exhaust nozzle; an axial magnetic field is set in order to (1) reduce charge surface losses, and (2) create a magnetic nozzle able to deliver momentum to the charges leaving the exit section.

The exhaust plume of a plasma thruster is a region characterized by complex interaction between particles, high electric fields and magnetic fields; in order to study the properties of the ejected ion beam in the thruster plume *Particle in cell* (PIC) simulations have been performed[15].

The results of the PIC simulations, are then parametrized in proper coefficients, that are implemented within the global model, in order to account for the particles and energy losses in the plume.

The inputs of the model are: (1) the mass flow rate entering the system, (2) the dimensions of the chamber (radius R and length L), (3) the nozzle throat-to-chamber section ratio and (4) the electrical power deposited into the plasma. The output parameters are the density of each species, the electron temperature and the homogeneous neutral-ion temperature inside the chamber.

2.1 Model formulation

The model geometry is a cylindrical reactor with an injection aperture (of negligible area) and an exhaust section at the diaphragm interface; a schematic of the source is shown in figure[2.1]. The input parameters of the model are the chamber dimensions D and L, the ϱ^* exhaust-to-chamber section ratio, the mass flow $\dot{m}$, and the deposited power P_W. The magnetic field is assumed to be axial and uniform with a value corresponding to the average value of the actual field provided by the system of magnets[4.1].

The electron temperature is determined by solving the time-dependent electron energy equation:

$$\frac{\mathrm{d}}{\mathrm{dt}}\left(\frac{3}{2}n_e k_b \mathrm{T_e}\right) = P_W - P_{col} - \Gamma_w \cdot \varepsilon_w - \Gamma_{exh} \cdot \varepsilon_{exh} \tag{2.1}$$

In the above formula P_{col} is the loss by elastic and inelastic collisions, Γ_w and Γ_{exh} are the wall and exhaust flux of electrons; ε_w and ε_{exh} are the wall and exhaust energy loss for each electron leaving the boundaries of the discharge[8]. The species densities are determined solving the time dependent mass balance equations:

$$\frac{\mathrm{d}n_i}{\mathrm{dt}} = \Phi_i + \dot{m}_{in} - \dot{m}_{out} \tag{2.2}$$

Where Φ_i is a source term containing production and loss of the i-th species by volume and surface reactions; $\dot{m}_{in}$ and $\dot{m}_{out}$ are the mass flow entering and exiting the system.

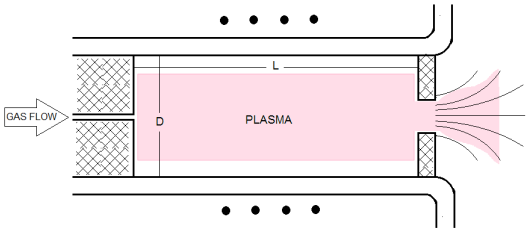

FIGURE 2.1: Schematic of the source considered for the numerical model.

In this model, neutral and ion particles are assumed to share a common temperature T. Atomic plasmas are not subject to considerable heating in low pressure non equilibrium discharges; a value for the gas temperature can be assumed based on estimation from literature, numerical formulas, experimental measurements (use of the wall temperature is common approach). In any case, in atomic low pressure non equilibrium plasmas, the

neutral gas temperature has a weak influence on the chemistry of the discharge, which instead is controlled by the electron temperature T_e.

Low pressure molecular gases, instead, are subject to considerable heating, mostly due to electron impact dissociation reactions. A high molecular gas temperature can affect the chemistry of the discharge in a way that is not negligible, compared to the influence of the electron temperature. A neutral-ion energy equation has been implemented for estimation of the gas temperature for the CO_2 model in section[3.3].

The rate of change of the neutral-ion temperature is estimated by the following energy balance:

$$\frac{\mathrm{d}}{\mathrm{d}t}\left(\sum n_i u_i\right) = \dot{m}_{in} h_{in} - \sum \Gamma^i_{exh} h_i - \Delta H_0 + \sum(\varepsilon_j - \delta h_{0j}) \tag{2.3}$$

The left hand side of the above equation is the change of internal energy of the mixture (summation is on the i-th species); in the right hand side, the first two terms are the entering and exiting fluxes of enthalpy, $\dot{m}_{in}$ is the input flow rate, u_i and h_i are *sensible* specific internal energy and enthalpy[16]. ΔH_0 represent the energy resulting from chemical reactions, and is written as the sum of the *standard enthalpy of reaction* of all reactions between heavy species[16].

$$\Delta H_0 = \sum H_{0j}(\text{reactants}) - \sum \mathrm{H_{0j}}(\text{products}) \tag{2.4}$$

Where H_0 is the enthalpy of formation of the considered species (summation is on the j-th reaction). The last term in equation(2.3) represent the energy resulting chemical reactions involving electrons and heavy particles; it is composed by an electron energy term ε (a potential threshold relative to the specific reaction, or an average electron energy) minus the enthalpy balance δh between heavy particles products and reactants [7, 11, 17].

2.1.1 Plasma and chemical volume reactions

In the computation of rate constants involving electron collisions, the heavy particle is considered at rest since the electron thermal velocity is much higher than neutral and ion thermal motion. The rate constant is computed averaging the cross section over the electron distribution function.

It is assumed that all species, electrons, neutrals and ions, have Maxwell-Boltzmann distribution at the relative temperature. Electron-electron collisions play the role of thermalization of the electron energy distribution function (EEDF), criteria for the establishment of a Maxwell distribution are found in [18, 19]. Consider the numerical factor $a = \nu_{ee}/(\delta\nu_e)$, where ν_{ee} and ν_e are electron-electron and electron-neutral collision frequencies, δ is the average fraction of electron energy transferred to a neutral particle during collision; Maxwell EEDF is attained at high values of the factor $a >> 1$, for instance, an Ar plasma at $2-4$ eV, $0.1-3\%$ ionization degree at 30 mTorr (typical for our experiment conditions), gives $a \sim 20-200$. Rate constants results:

$$K(\mathrm{T_e}) = \left[\frac{8e}{\pi m_e}\right]^{1/2} \frac{1}{\mathrm{T_e}^{3/2}} \int U\sigma(U) \exp\left(-\frac{U}{\mathrm{T_e}}\right) dU \tag{2.5}$$

With $\sigma(U)$ the impact cross section, e, m_e electron charge and mass, and $\mathrm{T_e}$[eV]. In case of reactions between heavy particles, the relation is modified with the reduced mass of the system and the relative kinetic energy between the particles:

$$K(T) = \left[\frac{8}{\pi M_R}\right]^{1/2} \frac{1}{(k_b T)^{3/2}} \int U_{rel}\sigma(U_{rel}) \exp(-\frac{U_{rel}}{T}) dU_{rel} \tag{2.6}$$

Whenever available in literature, measured rate constants are used. The energy loss by an electron upon elastic collision with a neutral is $3\mathrm{T_e}m_e/M$. The energy lost by an electron upon inelastic collision with a neutral correspond to the potential threshold of the reaction.

2.2 Surface plasma processes

2.2.1 Charged particles processes

The rate of electron-ion recombination at the wall is proportional to the ion density at the sheath. Charge density at the sheath is evaluated with semi-empirical solutions of the diffusion equation developed by Godyak[20] and reported also for electropositive and electronegative gases in [7, 8].

h_L and h_R are the ratio of the sheath to bulk positive ion densities in the axial and radial diffusion direction, the sheath densities can be calculated from the bulk charge densities; relevant material is found also in [21–23].

For clarity we will refer to positive ions with the subscript 'p', negative ions 'n', electrons 'e'; we report formulas implemented for the general case of a electronegative discharge, with $\alpha = \sum n_{n,i}/n_e$ the *electronegativity* parameter of the discharge (i.e. the negative ion to electron density ratio); if the parameter $\alpha \to 0$ the formulas for electropositive discharge are recovered.

In a *non magnetized* electronegative discharge the h_L and h_R parameters are:

$$h_L = \left[\frac{n_p^s}{n_p}\right]_{l=L} = \frac{1+3\overline{\alpha}/\gamma}{1+\overline{\alpha}} \frac{0.86}{[3+L/(2\lambda_p)+(0.86Lu_b/(\pi D_a^p))^2]^{1/2}} \tag{2.7}$$

$$h_R = \left[\frac{n_p^s}{n_p}\right]_{r=R} = \frac{1+3\overline{\alpha}/\gamma}{1+\overline{\alpha}} \frac{0.8}{[4+R/\lambda_p+(0.8Ru_b/(2.405J_1(2.405)D_a^p))^2]^{1/2}} \tag{2.8}$$

In the above formula u_b, λ_p are the Bohm velocity and the mean free path of the positive ion; $\gamma = T_e/T$ and $\overline{\alpha}$ is the average value of α [8]. The coefficient D_a^p is the effective ambipolar coefficient for the positive ion diffusion[22]:

$$D_a^p = D_p - \mu_p \frac{D_p(\overline{\alpha}+1) - \overline{\alpha}D_n - D_e}{\mu_p(\overline{\alpha}+1) + \overline{\alpha}\mu_n + \mu_e} \tag{2.9}$$

The expression for D_a^p results from conservation of charge fluxes and quasi-neutrality condition, it implements the diffusion and mobility coefficients for positive, negative charges and electrons; in the limit of electropositive discharge ($n_n \to 0$) becomes the classic ambipolar coefficient [7].

Ion and electron mobilities are calculated as $\mu_e = e/(m_e\nu_e)$, $\mu_{p,n} = e/(M_{p,n}\nu_{p,n})$; diffusivity is related to mobility by the *Einstein relation* $D/\mu = k_bT/e$. The Ion collision frequency is calculated as the ratio between thermal velocity and mean free path $v = v_{th}/\lambda$; electron collision frequency is evaluated with the electron elastic scattering rate constant $\nu_e = n_0K(\mathrm{T_e})$, with n_0 the neutral background density.

The ion mean free path results from elastic scattering and charge transfer, the cross sections for elastic scattering, $\sigma_{ES}/2$, and charge transfer, σ_{CT}, are estimated with the Langevine cross section formula, as explained in [7].

The rate of loss of positive ions by diffusion toward the surface is then expressed by

$$\Gamma_p = n_p u_b A_{eff} \tag{2.10}$$

The Bohm velocity of a electronegative discharge is modified as reported in [7], with α_s the electronegativity at the plasma-sheath interface:

$$u_b = \left[\frac{(1+\alpha_s)}{(1+\alpha_s\gamma)}\frac{e\mathrm{T_e}}{M_p}\right]^{1/2} \tag{2.11}$$

The rate of loss of negative ions on the wall is proportional to the Γ_n and is:

$$\Gamma_n = \frac{\Lambda^s_{ne}}{1+\Lambda^s_{ne}}\Gamma_p \tag{2.12}$$

Where $\Lambda^s_{ne} = \Gamma^s_n/\Gamma^s_e$ is the ratio of negative ion to electron flux at the sheath interface

$$\Lambda^s_{ne} = \frac{n^s_n v_{th,n}}{n^s_e v_{th,e}} = \alpha_s\left(\frac{m_e}{\gamma M_n}\right)^{1/2} \tag{2.13}$$

The rate of loss of electrons on the wall results from the continuity of charge flux condition: $\Gamma_e = \Gamma_p - \Gamma_n$.

The energy loss associated to the wall loss of electrons, is given by the potential drop in the sheath and the pre-sheath region plus the average thermal energy $2\mathrm{T_e}$. The collision-less sheath model is used to evaluate the potential drop trough the plasma and the sheath[7]; the loss term results:

$$\epsilon_w = 2\mathrm{T_e} + \frac{\mathrm{T_e}}{2}\left[\frac{(1+\alpha_s)}{(1+\alpha_s\gamma)} + \ln\left(\frac{M_p}{2\pi m_e}\right)\right] \tag{2.14}$$

2.2.2 Ambipolar cross diffusion and anomalous diffusion

The introduction of an axial magnetic field changes the diffusion conditions toward the lateral wall of the discharge. Electrons are filtered during cross-field transport as their mobility is strongly reduced while negative ions remain mostly unaffected [23]. A

characteristic of non magnetized electronegative discharge is the formation of a negative ions core, with the result that the loss of electrons to the lateral wall is several orders greater than the loss of negative ions; in magnetized discharges the situation is reversed, and the electrons are kept within the core of the plasma. Fluid and particle in cell simulations agree with analytical models in this respect [22, 23], and the ratio of negative ion to electron flux, $\Lambda_{ne\perp}$, is approximated by:

$$\Lambda_{ne\perp} \simeq \frac{D^n_{a\perp}\overline{\alpha}}{D^e_{a\perp}} \tag{2.15}$$

With $D^n_{a\perp}$ and $D^e_{a\perp}$ the effective *cross* ambipolar diffusion coefficients for the negative ions and electrons [22].

$$D^n_{a\perp} = D_{n\perp} + \mu_{n\perp}\frac{D_{p\perp}(\overline{\alpha}+1) - \overline{\alpha}D_{n\perp} - D_{e\perp}}{\mu_{p\perp}(\overline{\alpha}+1) + \overline{\alpha}\mu_{n\perp} + \mu_{e\perp}} \tag{2.16}$$

$$D^e_{a\perp} = D_{e\perp} + \mu_{e\perp}\frac{D_{p\perp}(\overline{\alpha}+1) - \overline{\alpha}D_{n\perp} - D_{e\perp}}{\mu_{p\perp}(\overline{\alpha}+1) + \overline{\alpha}\mu_{n\perp} + \mu_{e\perp}} \tag{2.17}$$

Cross diffusion and mobility coefficients are obtained from the unmagnetized ones by multiplication with the magnetic factor[7, 24] $f = [1 + \omega_c^2/\nu^2]^{-1}$.

In this frame the flux of charged particles within the source is split into two components: a *parallel* component follows the rules of unmagnetized discharge to describe the flux toward the base surfaces of the cylindrical chamber, a *transverse* component follows the rules of magnetized discharge to describe the flux toward the lateral surfaces of the cylindrical chamber. The underlying approximation is that the flux of each specie is parallel to each other [24]: $\Gamma_n + \Gamma_e \equiv \Gamma_p$. This is true in a one dimensional problem; approximate one-dimensional congruence will apply for sufficiently extreme geometries, such as very long cylinders or very short cylinders. Various experimental results indicate that the actual effective perpendicular electron diffusion coefficient is, in fact, much greater than that of equation(2.17) by several orders of magnitude [7, 24]. *Short circuit* effects can take place at the boundary of the plasma, a conducting wall or the plasma sheath, that deteriorates the confinement capability of the magnetic field; a good review of the problem is given by Vidal[24]. Lieberman and Lichtenberg [7] have proposed a diffusion coefficient $D_{L\perp}$, based on considerations on the divergence of the charged flux $\nabla \cdot (\Gamma_p - \Gamma_n - \Gamma_e) = 0$, that explains better several experimental results.

$$D_{L\perp} \simeq \mu_{p\perp} \mathrm{T_e} \tag{2.18}$$

The coefficient $D_{L\perp}$ is approximately two orders of magnitude higher than $D_{a\perp}$; with mid values of magnetic fields (B $\leq$ 400 G), in low source pressure conditions (p $\leq$ 10 mTorr), the condition $D_{a\perp} << D_{L\perp} < D_a$ is met. The cross diffusion coefficient is related to the wall losses and therefore to the power balance of the discharge; The adoption of a coefficient instead of another, leads to electron densities that differ, at least, by one order of magnitude, and electron temperatures ranging from 2 to 4 eV.

In such a situation it is useful to define a coefficient that, in the average, better fits the experimental results. We employ an *effective* cross diffusion that is defined as weighted average between $D_{a\perp}$ and $D_{L\perp}$; the average is on the order of magnitude of the coefficients and the expression is:

$$\log D_{R\perp} = (1-\lambda) \log D_{a\perp} + \lambda \log D_{L\perp} \tag{2.19}$$

The parameter λ indicates how close we are to the classical ambipolar conditions, $\lambda = 0$, or to the anomalous diffusion conditions, $\lambda = 1$. Based on the experimental results that will be presented on chapter[4], and the numerical simulations presented on section[3.1.1], the parameter sets to the value $\lambda = 0.3$, with $D_{R\perp} \sim 3.4 D_{a\perp}$ and $D_{R\perp} \sim 6 \cdot 10^{-2} D_{L\perp}$, thus the confinement is very close to the ideal one.

2.2.3 Neutral particles processes

The neutral surface processes relevant in this work are are de-activation of metastable excited states and recombination of atomic radicals; the rates are proportional to the species flux toward the surface. A dimensionless loss probability or recombination factor γ express the probability of the reaction to occurs; this coefficient depends on the specific atom or molecule under consideration and the surface material properties.

The probability for deactivation of an atomic excited state is, with good approximation[25], unitary; for molecular metastable excited states literature data has to be used when available. As for recombination of atomic oxygen and nitrogen into diatomic O_2 and N_2 the wall surface acts as a partner for a three body recombination process. In order

to calculate the flux of species impinging on the wall we consider the analytical solution of the diffusion equation in cylindrical geometry[26]. The rate of recombination or de-activation of a neutral radicals and metastable excited species is expressed by:

$$\Gamma = \gamma D_{eff}/\Lambda^2 \tag{2.20}$$

Λ is a diffusion length that for cylindrical vessel is defined as

$$\frac{1}{\Lambda^2} = \frac{\pi}{L^2} + \frac{2.405}{R^2} \tag{2.21}$$

D_{eff} is the effective diffusion coefficient of the neutral species of interest which has the expression

$$\frac{1}{D_{eff}} = \frac{1}{D_{CE}} + \frac{1}{D_{KN}} \tag{2.22}$$

with D_{CE} the diffusion coefficient estimated using the Chapman-Enskog equation for gas diffusivity[27] and $D_{KN} = v_{th}\lambda/3$ is the Knudsen free-diffusion coefficient.

2.3 Plasma exhaust

Since the gas is exhausted into the vacuum chamber, the neutral flow exiting through the diaphragm is assumed to be choked. The flow rate of each neutral species is given by the isentropic relation of the mass flow through a choked section:

$$\Gamma_i = n_i \left[\frac{k_b T k_i}{m_i} \left(\frac{2}{k_i + 1} \right)^{\frac{k_i+1}{k_i-1}} \right]^{1/2} \tag{2.23}$$

Where k_b is the Boltzmann constant, n_i, m_i and k_i are the density, mass and specific heat ratio of the neutral i-th specie.

The ejection of charged particles and its properties have been investigated by means of 3D PIC (particle in cell) simulations; the code used is F3MPIC [28, 29]. The code can manage geometries of arbitrary complexity and an arbitrary number of particle species, both charged and neutral. The unstructured tetrahedral mesh is generated by GMSH, a three-dimensional mesh generator developed by C. Geuzaine[30]. The characteristic dimension of the unstructured mesh (edge size) is set in order to be less than the Debye length of the plasma.

The electro-magnetic fields are solved separately with a finite element solver (FEM) called GetDP[31, 32].
The purpose of the PIC simulations is to get physical insight of the plasma ejection mechanism in the thruster plume; in the plume region the RF electrostatic component of the field is predominant, and contributes mainly to the acceleration of the particles. In the simulations only the electrostatic field is solved, allowing also to reduce the computational effort; the stationary magnetic field is solved at the beginning of the simulations. These simulations were performed by Lucca Fabbris and reported in [15, 33].

A series of control surfaces, figure[2.2], normal to the axial flow direction, are placed along the simulation domain, for particle monitoring purposes; the properties of the ejected plasma beam are evaluated by analysis of the position and momentum of particles crossing the control surfaces at each time step. The particles momentum and mass flow rate at a given time step i are expressed as:

$$\dot{m}_{(i)} = \frac{1}{\Delta t_{(i)}} \sum M_j^{(i)} \tag{2.24}$$

$$p_{(i)} = \frac{1}{\Delta t_{(i)}} \sum M_j^{(i)} v_j^{(i)} \tag{2.25}$$

The properties of the ejected beam (ion flux and velocity) are expressed in terms of the two dimensionless parameters: the extraction coefficient β and the acceleration coefficient α.

The extraction coefficient is the ratio between the flux ejected and the flux of ions entering a planar electropositive collisionless sheath[7], $\Gamma_p = n_p^s u_b$; n_p^s is the density at the plasma-sheath interface determined from the theory, $n_s = \exp(-1/2) n_p$, where n_p is the bulk average density.

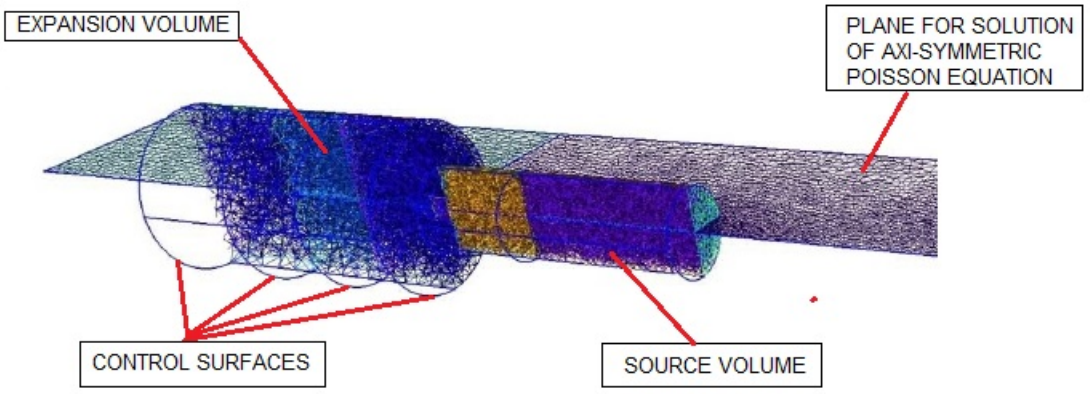

FIGURE 2.2: PIC simulation domain example.

$$\beta = \frac{\Gamma_{exh}}{\Gamma_b} = \frac{\Gamma_{exh}}{n_p^s u_b} \tag{2.26}$$

The acceleration coefficient is the ion Mach number evaluated downstream the thruster plume.

$$\alpha = \frac{u}{u_b} \tag{2.27}$$

Several simulations have been performed varying magneto-static field strength, figure [2.3] shows the exhaust and acceleration coefficients for Ar ions as a function of the average magnetic field intensity. Both coefficients are approximatively constants for values of average magnetic field strength ranging from 200 to 600 Gauss.

The energy cost that the system has to sustain, in order to accelerate one particle to a value $u = \alpha u_b$ is:

$$\varepsilon_{exh} = \frac{1}{2} M_p u^2 = \frac{1}{2} e \mathrm{T_e} \alpha^2 \tag{2.28}$$

with e the electron charge and T_e expressed in eV.

The force exerted by the thruster is $F = \dot{m} u_{ex}$; this general expression include the thrust exerted by the ions and also the thrust exerted by the neutral particles (most of the times negligible). Substituting for the acceleration coefficient becomes:

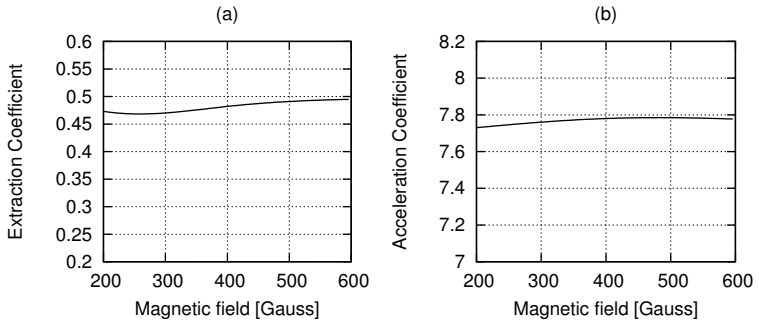

FIGURE 2.3: Extraction coefficient(a) and acceleration coefficient(b), for Ar ions, function of the average magnetic field intensity.

$$F = \dot{m}_p \alpha u_b + \dot{m}_g c_{ex} \tag{2.29}$$

Where the subscript p and g are for ions and neutrals, and c_{ex} is the exhaust velocity of the neutral gas. The specific impulse is the thrust produced per unit mass flow rate of propellant ejected, and divided by the earth gravity constant; higher specific impulse results in lower propellant consumption. The propulsive efficiency refers to the ratio of the jet power over the electric power deposited into the plasma:

$$I_{SP} = \frac{F}{g_0 \dot{m}} \tag{2.30}$$

$$\eta_P = \frac{I_{SP} F g_0}{2 P_W} \tag{2.31}$$

Chapter 3

Numerical analysis

The European project Helicon Plasma Hydrazine Combined Micro (HpH.com) [34], was devoted to the development of a plasma thruster for low thrust (1mN) attitude control operations at low power (50 W), using Argon as propellant. The project was carried out from year 2008 to 2012, during this time an innovative and high performance RF plasma source was developed [35]. In the first section of this chapter validation of the discharge model is performed with Argon gas; the model is then used for demonstration of the good efficiency of the source developed at CISAS.

The HPT is potentially suited for a variety of applications; scalability, throttability, versatility appear to be its major characteristics; in this perspective the project Helicon Plasma Thruster for Space Missions - AO7048 started from the output of the HpH.com program; the project was carried out from 2012 to 2014, among the purposes of the project was the investigation of the behaviour of the thruster with different propellants, applicable to different mission scenarios ranging from Low Earth Orbit to Mars exploration missions. In the second part of this chapter several simulation models are presented for different gases; the behaviour of each gas is compared in terms of propulsive performances of the thruster.

The AO7048 project identified carbon dioxide as gas with good propulsive performances. Furthermore the use of the thruster with CO_2 is interesting for potential mission scenarios involving the International Space Station (ISS) and the exploration of planet Mars, which has recently come to the attention of the space community. The STRONG SAPERE program starts on the results of the previous AO7048 and HpH.com programs and aims to develop a prototype of a high power HPT thruster working with Ar and CO_2. In the third part of this chapter the CO_2 model is presented, together with experimental validation and numerical analysis.

3.1 Ar Thruster Model

The HpH.com project developed a plasma thruster for low thrust (1mN) attitude control operations at low power (50 W), using Argon as propellant; the design process started from a standard four-loop helicon antenna and added several improvements [35].

The work resulted in the development of a source capable of achieving high plasma density with low power consumption; in the experiments described in chapter 4, and used here for validation purposes, density is achieved in the range from $6 \cdot 10^{18} - 1.6 \cdot 10^{19} \mathrm{m}^{-3}$ with deposited power from 40-130 W.

It is clear that a source capable of producing high density, with low power consumption, and with the ability to accelerate a beam of charged particles, it is not only interesting for generating thrust in space environment, but can find also its application in the field of industrial processing. Argon is one of the most used gas for plasma source operations, the great availability of physical and chemical data concerning impact cross sections, radiative transitions, *etc*, make of it the ideal gas for plasma sources investigation. Reactions data set for Ar plasma modeling can be found in many articles or textbooks, for instance [7, 8, 36]. In this work we adopted the reaction dataset reported in [7]; the species considered are Ar, Ar($_4$s), Ar($_4$p), Ar^+, the reaction set is reported in table[A.1] in Appendix; the table reports also the extraction and acceleration coefficients, α and β, resulting from PIC simulations. The simulations are able to predict the experimental results, and to demonstrate the high efficiency of the source, in terms of wall diffusion losses and power loss per charge pair created.

3.1.1 Validation

In section[2.2.2] we saw that magnetized discharges are usually subject to anomalous diffusion effects; these effects deteriorate the confinement capability of the magnetic field, allowing higher electron fluxes to the wall, and therefore higher losses, affecting the power balance of the discharge.

This topic is well discussed by Vidal[24], and Lieberman[7] suggest the use of a coefficient $D_{L\perp}$ that fits better the experiments in literature. $D_{L\perp}$ is roughly two orders of magnitude greater than $D_{a\perp}$; with mid-high magnetic fields (B $\leq$ 400 G), and depending on the source pressure, the condition $D_{a\perp} << D_{L\perp} < D_a$ is easily met. In such a situation it is useful to define a coefficient that, in the average, matches the experimental results. We defined an effective cross diffusion $\log D_{R\perp} = (1-\lambda)\log D_{a\perp} + \lambda \log D_{L\perp}$ (see section[2.2.2]) that is a logarithmic weighted average between $D_{a\perp}$ and $D_{L\perp}$. We have found that the electron density measurements are well matched with $\lambda \sim 0.3$, which

means that $D_{R\perp} \sim 3.4 D_{a\perp}$ and $D_{R\perp} \sim 6 \cdot 10^{-2} D_{L\perp}$, thus the confinement is very close to the ideal one.

Table[3.1] reports the source confisuration, Table[4.2] reports the six test case, flow rate and deposited power, used for validation. Table[3.3] reports the results of the numerical simulations compared with the experimental values; the calculated electron densities are within a factor 1.0-1.5 to the measured ones, while the electron temperature results smaller of a 10 to 32% of the experimentally estimated values.

TABLE 3.1: Plasma source configuration

Parameter	Description
Discharge chamber length	135 mm
Discharge chamber inner diameter	19 mm
Outlet diaphragm diameter	5 mm
Magnetic system	Two radially-polarized rings (diameters of 39 mm and 86 mm, respectively) composed of cubic (edge length of 20 mm) SmCo permanent magnets with radial magnetization

TABLE 3.2: Argon test matrix.

Test	Mass Flow Rate [mg/s]	Deposited Power [W]
01	0.20	38
02	0.20	59
03	0.20	122
04	0.17	39
05	0.17	59
06	0.17	97

TABLE 3.3: Comparison between numerical and experimental values for electron densities and temperatures.

Test	n_e (measured) [m^{-3}]	n_e (calculated) [m^{-3}]	T_e (estimated) [eV]	T_e (calculated) [eV]
01	$9.0 \cdot 10^{+18}$	$5.6 \cdot 10^{+18}$	2.8	1.9
02	$8.0 \cdot 10^{+18}$	$8.7 \cdot 10^{+18}$	2.4	1.9
03	$1.6 \cdot 10^{+19}$	$1.7 \cdot 10^{+19}$	2.5	1.9
04	$6.0 \cdot 10^{+18}$	$5.8 \cdot 10^{+18}$	2.4	2.0
05	$9.2 \cdot 10^{+18}$	$8.8 \cdot 10^{+18}$	2.5	2.0
06	$1.5 \cdot 10^{+19}$	$1.4 \cdot 10^{+19}$	2.3	2.0

It is important to point out that the single value of $\lambda = 0.3$ matches the tests with different flow rates and electrical power; it is therefore reasonable to assume that its value depends on magnetic field configuration and source geometry, rather than operative flow power conditions. Figure[3.1] show the variation with λ of the ratio between the calculated and the measured electron densities for each test case. The only case that presents a marked deviation is test 01; this test realized an exceptional high density with a parameter λ close to 0.2.

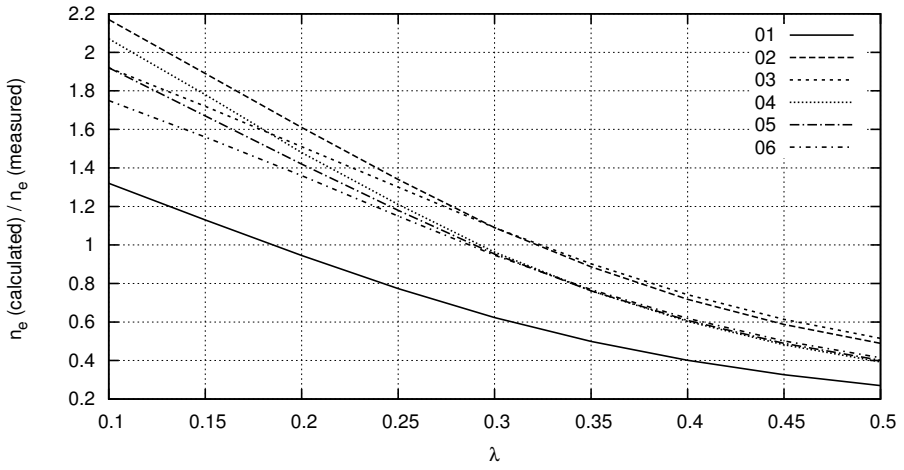

FIGURE 3.1: Calculated and the measured electron density ratio versus λ parameter for each test case.

3.1.2 Comparison with standard Helicon sources

It can be useful to compare the source to other magnetized sources reported in literature; this would provide a more practical picture in terms of source performances. Unfortunately several difficulties arise since operating conditions and configurations, of the experiments in literature, vary widely; also many published works don't reports all the necessary data for a comparison. For these reasons, comparison with other experiments, is only qualitative. The question arise of what are suitable parameters for indication of good source performances; for instance the electron density is not an indicative parameter, since higher volume reactors would require higher powers in order to reach the same density. If our goal is simply to achieve high density with low power consumption, than a good parameter, suggested by Vidal[24], is the absorbed power per ion-electron pair created, $\Theta = P_W/N_e$, with P_W the absorbed power and N_e the total number of electrons within the source volume. This parameter accounts for the creation of the whole plasma volume; the ionizing and confinement capability of the system are implicit in it, because it contains the surface energy losses. Calculation of the Θ parameter for the six test cases reported in the previous paragraph, with the source dimension reported in table[3.1], and the average densities obtained with the interferometer, gives values of Θ ranging from 0.11 to 0.2 pW; discharge pressure ranges fro 25 to 30 mTorr.

We have selected several works on Argon helicon discharges from literature; the selection is based on the availability of experimental data; many papers reports only peak densities measured at the center of the discharge volume, in these cases we estimate the average values assuming a density profile resulting from the classical anisotropic diffusion equation with uniform coefficients in cylindrical coordinates:

$$n_e(r,z) = n_{e0} \sin\left(\frac{\pi z}{L}\right) J_0\left(\frac{2.405r}{R}\right) \tag{3.1}$$

Where J_0 is the zero order bessel function of the first kind evaluated at $(2.405r/R)$, and n_{e0} is the peak central electron density; the average density results from integration and is $\bar{n}_e = 0.2741 n_{e0}$. We report the better-case estimation of Θ for all the works considered and based on the available data;the only exception is the work from Vidal[24], which specifically reports the obtained values of the parameter Θ.

Vidal *et al*[24] studied the cross diffusion of charges in magnetized discharges; they made measurements in a reactor, 67 cm length and 14 cm radius; the tests were conducted at a fixed absorbed power of 270 W, 1 mTorr discharge pressure, while varying the magnetic field (100-1000 Gauss). They observed that the experimental data were best fitted using the Lieberman diffusion coefficient, and obtained Θ values ranging from 0.8 pW, at 100 Gauss, to 0.12 pW at 1000 Gauss; they observed that at sufficiently high fields, the Lieberman cross diffusion approaches the classic ambipolar cross diffusion ($D_{L\perp} \to D_{a\perp}$); this limit corresponds, in their tests, to the value of 0.12 pW.

Lafteur *et al*[37] performed measurements on a helicon reactor, 20 cm length and 6.8 cm radius, for propulsion applications; they measured peak densities in the center of the discharge while varying magnetic field (10-160 Gauss), input power (50-400 W), and chamber pressure (0.3-3 mTorr). The highest peak density was $1.8 \cdot 10^{17} \mathrm{m}^{-3}$, and was obtained at 3 mTorr, with 30 Gauss magnetic field and 250 W input power. They reported an efficiency of antenna coupling of 0.6 for this pressure, resulting in a Θ value of $\sim$1 pW.

Chen[38] designed a helicon reactor, 5 cm length and 2.5 cm radius, with permanent magnets, for industrial processing applications; the discharge is run at 15 mTorr for different values of magnetic field (50-200 Gauss), and input power (200-1000 W). The higher densities where found for an average field of 60 Gauss at 400 W input power. Probe measurements in the center of the discharge reported a peak density of $1.6 \cdot 10^{18} \mathrm{m}^{-3}$, which results, assuming 0.6 coupling efficiency, in a Θ value of $\sim$5 pW. However, measurements made outside the source region (6.8 cm below the source, along the exhaust of the plasma flow), report peak densities of $5.3 \cdot 10^{17} \mathrm{m}^{-3}$, therefore it is possible that the ionizing action of the antenna extends beyond the source region, and therefore the Θ value should be lower.

Kaeppelin *et al*[39] performed measurements on a helicon reactor, 20 cm length and 7.5 cm radius; they measured peak densities in the center of the discharge while varying

magnetic field (0-150 Gauss), input power (100-2500 W), and chamber pressure (0.37-3.7 mTorr). They observed three discharge modes: a low density capacitive mode (E-mode), a medium density inductive mode (H-mode) and a high density helicon mode (W-mode). The W-mode appeared at high input powers ($\geq$ 900 W). They reported peak density values obtained with the Langmuir probe tip placed at the center of the discharge; $1.6 \cdot 10^{17}\mathrm{m}^{-3}$ ion density, was obtained at 3 mTorr, with 80 Gauss magnetic field and 1500 W input power; assuming an efficiency of antenna coupling of 0.6 this leads to a Θ value of $\sim$1.5 pW.

The last work considered is from Tysk *et al*[40]; their discharge is realized inside a Pyrex tube, 1.75 m length and 5 cm radius, the 20 cm length antenna is placed at a certain axial coordinate close to the left end of the tube, the diagnostic probe is introduced from the right end of the tube. An uniform magnetic field is produced by a series of coils deployed along the tube, and the discharge is run at 3 mTorr pressure. The authors evidenced three regimes of low, medium and high ionization, associated with values of increasing magnetic field and input power. The plasma volume appears to extend beyond the source region, using the radial density profile (at $z = 15$cm from the right end of the antenna), with 600 Gauss magnetic field and 800 W deposited power, we estimate a value of $\Theta \sim 0.095$ pW.

It is necessary to point out that the comparison is merely qualitative, many aspects cannot be taken into account; for instance as pointed out by Chen, helicon reactors designed for propulsive applications have high exhaust rates, which depletes the source of charge particles more severely resulting in a lowering of the bulk density. A more thorough comparison would require also the consideration of a parameter that describes the influence of the exhaust of charge particles, important for instance in sputtering applications; however these kind of data are usually not available. Figure[3.2] summarize the data resulting from the comparison of the different experiments.

3.1.3 Parameters investigation with Ar discharge model

In this section we draw some considerations with the help of the numerical model. Simulations investigating the effect of different power inputs, have confirmed the general trend that at higher powers correspond higher electron densities and temperatures. Less straightforward is the effect of the chamber pressure. Figure[3.3] shows the diffusion coefficients with variation of the pressure within the source, for different values of the magnetic field; the curves were obtained fixing the ionization degree, within the discharge tube, to 1%, and the electron temperature to 2 eV. In Figure[3.3.a] the ambipolar diffusion coefficient (D_a) decreases with increasing pressure (due an increasing

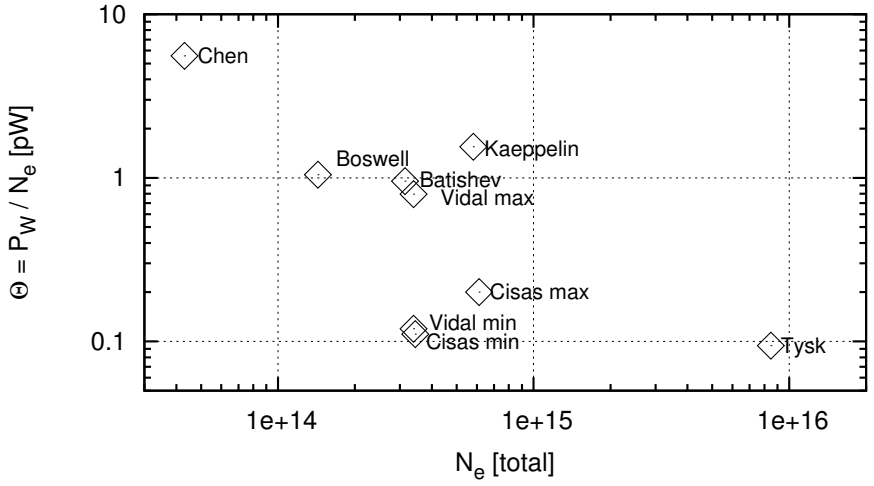

FIGURE 3.2: Θ values versus absolute number of electron particles in the source chamber for different experiments in literature. Vidal and our (Cisas) experiment are reported with the minimum and maximum achieved Θ.

of the collision frequency). Figure[3.3.b] shows the trend for the effective cross diffusion coefficient ($D_{R\perp}$) as the pressure rises, starting from the lowest values, the degradation of the confinement become apparent (due to an increase of the collision frequency); it reaches a maximum, associated with a value of the magnetic field, and then start decreasing again, as the confinement of the magnetic field become ineffective with increasing pressure. This trend is known in literature [41], in the absence of magnetic field the diffusion coefficient decreases with collision frequency; on the other hand, when the effect of the magnetic field is dominant, the cross diffusion is enhanced by collisions.

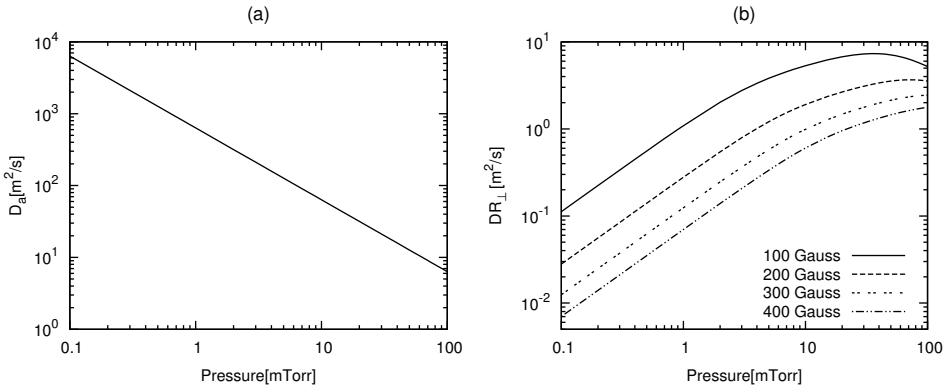

FIGURE 3.3: Variation of the diffusion coefficients with chamber pressures: (a) effective cross diffusion $D_{R\perp}$ and (b) ambipolar diffusion D_a; numerical values are obtained for a fixed ionization degree of 1%, T_e = 2 eV and T = 400 K.

Pressure variation at fixed input power and mass flow rate: the previous curves showed the correlation between source pressure and the diffusion coefficients;

in a system with gas flow, the build-up of pressure results from external controllable parameters (vessel geometry and flow rate). In Figure[3.4] we report the effect of the pressure (1-20 mTorr range) on the electron density and the Θ parameter for a fixed input power of 60 W, in this case different values of pressure, within the source, are achieved by variation of the exhaust-to-chamber ratio ϱ^*; the gas flow rate is set to 0.1 mg/s, source length and diameter are 135 mm and 19 mm respectively.

Figure[3.4a] shows a maximum of the electron density that depends on the strength of the confinement; this maximum moves toward higher pressures as the strength of the magnetic field is increased. After the maximum is reached the electron density starts decreasing because of confinement degradation. The 100 Gauss curve has the maximum at lower pressures, not shown in the graph; the mild increase of density that follows is due to an increase of the efficiency of the discharge in terms of *power-dissipation channels* that will be explained shortly. Figure[3.4b] shows the expected reverse trend of the Θ parameter compared to the electron density.

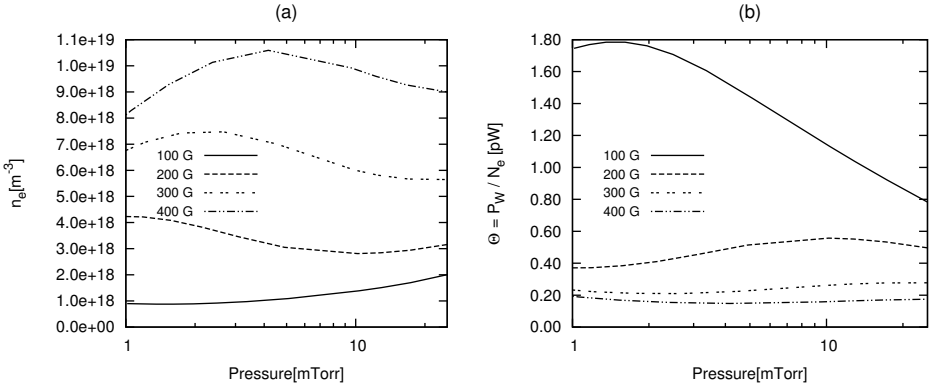

FIGURE 3.4: Variation of the electron density(a) and Θ parameter(b) with chamber pressures; numerical values are obtained for a fixed input power of 60 W, gas flow rate 0.10 mg/s, source length and diameter are 135 mm and 19 mm.

Efficiency within the discharge is affected by the proportion between the different channels of power dissipation. Electrical power is transferred to the electrons by EM excitation; this energy is then expended in bulk plasma collisions (responsible for charges creation) and lost through flux at the boundaries of the discharge volume. Figure[3.5a] shows the variation of the power expended in bulk plasma collisions over the total dissipated power (collision, wall and exhaust losses). It can be seen that, as the pressure increases, the weight of the surface and exhaust losses, on the total expended power, is diminished in favour of the collisional losses.

Figure[3.5b] reports the ionization degree achieved within the discharge, conditions are the same of Figure[3.4]. Higher ionization degree is achieved at lower pressures by virtue of hgher electron temperatures and better confinement. The ionization degree express

an efficiency by its own in terms of gas utilization (if the purpose of the discharge is to maximise the number of ions produced); however, it is different from the energetic efficiency represented by the θ parameter.

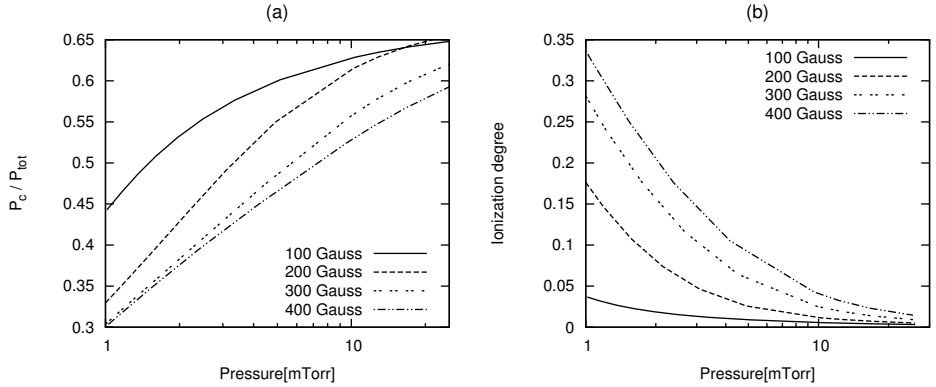

FIGURE 3.5: Variation with chamber pressures of the (a) collisions-to-total power ratio and (b) ionization degree; numerical values are obtained for a fixed input power of 60 W, gas flow rate 0.10 mg/s, source length and diameter are 135 mm and 19 mm.

Now we turn our attention to the range 10-100 mTorr setting the input power to 200 W, the gas flow rate to 0.3 mg/s and changing the pressure inside the source by altering the exhaust-to-chamber ratio ϱ^*. We can observe, in Figure[3.6a], that the increasing trend of the electron density and the decreasing trend of the Θ parameter is still maintained at higher pressures, thanks to the increase of the collisional losses on the total dissipated power; this effect is less pronounced for high magnetic fields.

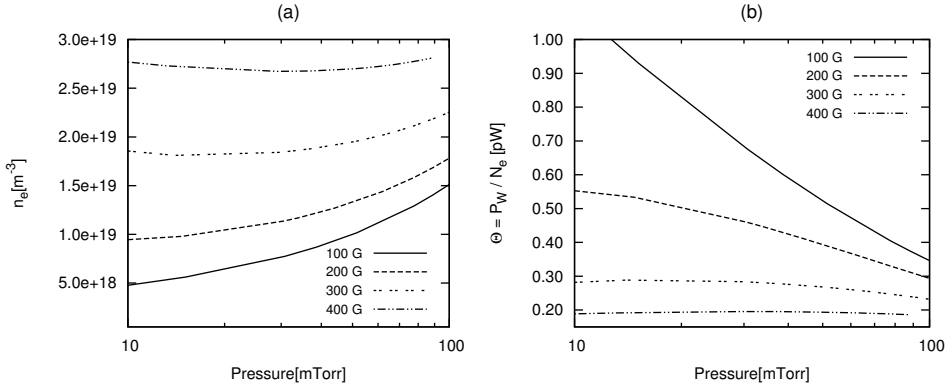

FIGURE 3.6: Variation of the electron density(a) and Θ parameter(b) with chamber pressures; numerical values are obtained for a fixed input power of 200 W, gas flow rate 0.30 mg/s, source length and diameter are 135 mm and 19 mm.

Pressure variation at variable input power and mass flow rate: in these simulation we want to see the effect of pressure variation due to an increase of flow rate; we do so keeping constant the specific power to mass flow input within the discharge to the value of 600 $Wmg^{-1}s^{-1}$, changing the mass flow rate and power accordingly. We also

fix the exhaust-to-chamber ratio ϱ^* to the value of 0.07 (the value implemented in the experimental tests), source length and diameter are 135 mm and 19 mm respectively.

Figure[3.7] displays the change of electron density and temperature within the discharge. The increase of n_e and the decrease of T_e are due to the increase of the collisional losses, compared to the exhaust and wall losses, on the total power budget of the discharge.

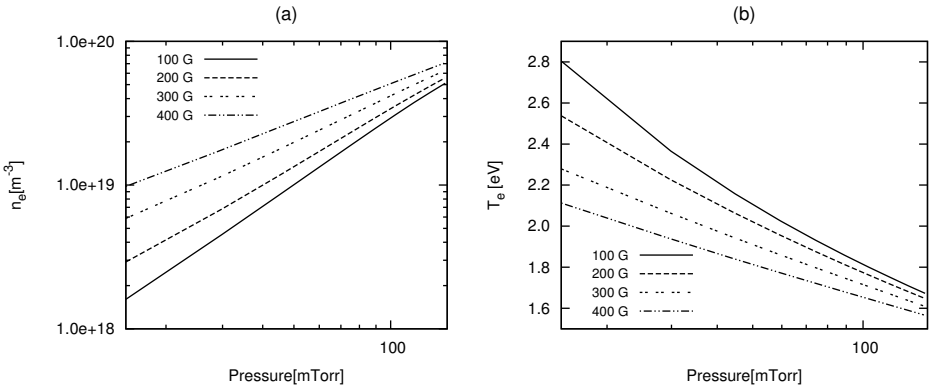

FIGURE 3.7: Variation of the electron density(a) and electron temperature(b) with chamber pressures; numerical values are obtained for a fixed specific power to mass flow of 600 $Wmg^{-1}s^{-1}$, source length, diameter and exhaust-to-chamber ratio are 135 mm, 19 mm and 0.07.

Figure[3.8] shows the degree of ionization and the Θ parameter; we can see that for a weak confinement, working at higher pressure is beneficial for the discharge; the reverse happens at higher field when the confinement is still enforcing its effect.

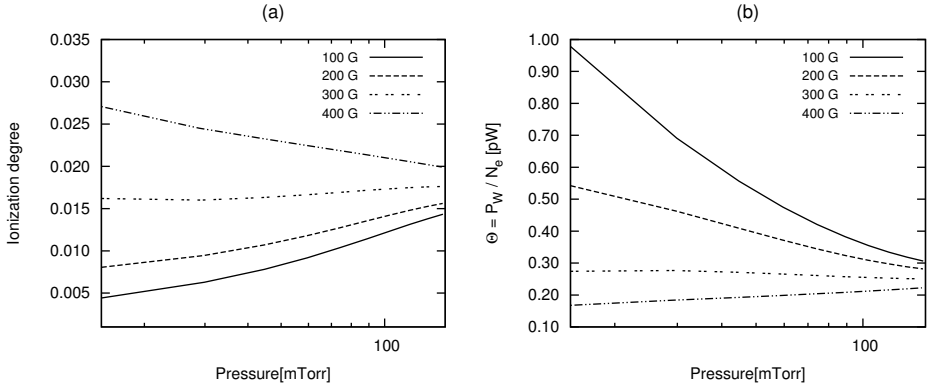

FIGURE 3.8: Variation of the ionization degree(a) and Θ parameter(b) with chamber pressures; numerical values are obtained for a fixed specific power to mass flow of 600 $Wmg^{-1}s^{-1}$, source length, diameter and exhaust-to-chamber ratio are 135 mm, 19 mm and 0.07.

From the performed parameter investigation we can draw the following conclusions:

- Low values of the Θ parameter are obtained at low pressure ($<$ 10 mTorr) by virtue of the confinement effect of the magnetic field (with $B \geq 200$) Gauss; low

Θ is obtained also at high pressures ($>$ 40 mTorr) because of a decrease of the weight of the boundary losses on the total power budget of the discharge. In the mid pressure region the value of Θ is more affected by the strength of the magnetic field.

- In the range of power ($P_W < 200$ W) high ionization degrees with high temperatures and low Θ values are achievable at low pressures implementing a moderate magnetic field (400 Gauss).

3.1.4 Propulsive performances

In order to obtain good thruster performances, high specific impulse and propulsive efficiency, it should be necessary to achieve high electron temperatures and ionization degrees. In the range of available power from 50 to 200 W good performances can be achieved at low pressures exploiting the confinement capability of the magnetic field; we use the model to show that is possible to increase the electron temperature and the ionization degree for this purpose.

We fix the magnetic field to the value of 400 Gauss, the source length and diameter to 135 mm and 19 mm respectively, as in the experimental conditions, and change the power input in the discharge in the range 50-200 W; different chamber pressures can be achieved with different values of the exhaust-to-chamber ratio ϱ^*. Simulations for a mass flow rate of 0.1 mg/s are reported in figure[3.9]; the figure shows that the increase of power and ϱ^* are both beneficial in terms of propulsive performances.

Figure[3.10] reports simulations for a mass flow rate of 0.2 mg/s, and figure[3.11] reports the ionization degree and the electron temperature for the same case. Chamber pressure ranges between 0.5 and 5 mTorr, Θ span from 0.2 - 0.6 pW.

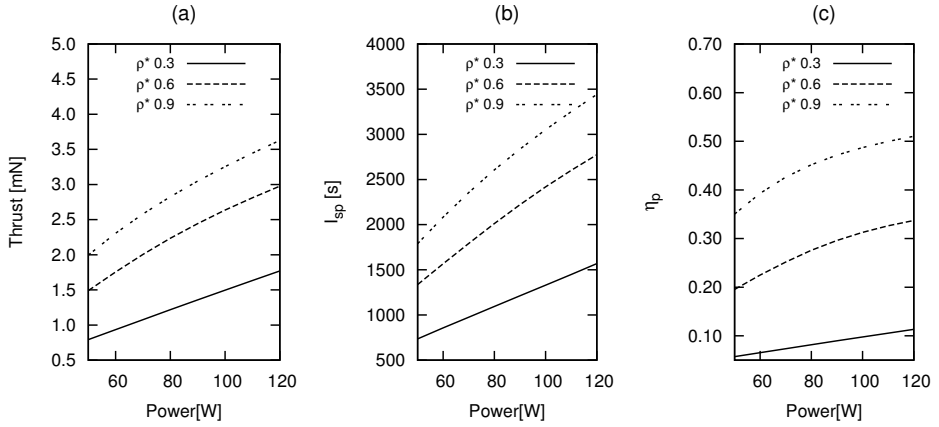

FIGURE 3.9: Thrust(a), specific impulse(b) and propulsive efficiency(c): variation versus power input, for different values of ϱ^*; numerical values are obtained for a fixed mass flow rate of 0.1 mg/s, magnetic field, source length, and diameter are 400 Gauss, 135 mm and 19 mm.

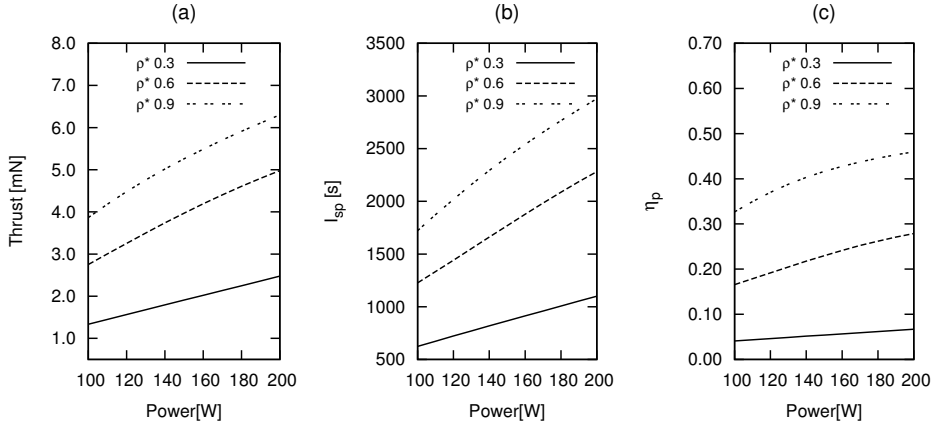

FIGURE 3.10: Thrust(a), specific impulse(b) and propulsive efficiency(c): variation versus power input, for different values of ϱ^*; numerical values are obtained for a fixed mass flow rate of 0.2 mg/s, magnetic field, source length, and diameter are 400 Gauss, 135 mm and 19 mm.

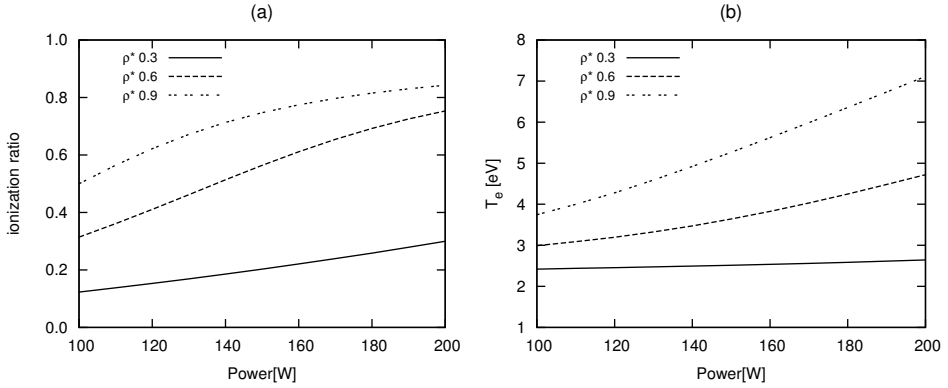

FIGURE 3.11: Ionization degree(a) and electron temperature(b): variation versus power input, for different values of ϱ^*; numerical values are obtained for a fixed mass flow rate of 0.2 mg/s, magnetic field, source length, and diameter are 400 Gauss, 135 mm and 19 mm.

3.2 Multi Species Model

The project "Helicon Plasma Thruster for Space Missions - AO7048" funded by the European Space Agency, starts from the output of the HpH.com program; its purpose is the numerical investigation, from the point of view of concept and feasibility, of a versatile thruster that can work with different propellants, and therefore applicable to different mission scenarios. Different propellants are identified for different scenarios: air-breathing permanent orbiting on Jupiter (hydrogen), Mars (carbon dioxide) and Titan (nitrogen); low earth orbit (air) and international space station utilization and waste gases (air, nitrous oxide, carbon dioxide). The final phase of the project involved the selection of a gas based on a comparison of the performances between the considered gases, and based also on the attractiveness of the different scenarios proposed.

This section describes the numerical model used to estimate the performances of the thruster with H_2, O_2, N_2, N_2O, and CO_2.
The input parameters of the model are the thruster geometry, the feeding mass flow rate, the average magnetic field strength and the electron temperature, T_e, of the plasma inside the source. We did not use the electrical power as input for reason that will be explained later. The axial magnetic field strength is fixed to a value of 1100 Gauss in order to ensure an adequate confinement for the resulting source pressures. The output parameters are the density of the species generated within the discharge, and the required electrical power, P_W, necessary to sustain the plasma at the given electron temperature; with these outputs the thruster performances can be evaluated.

PIC simulations have been performed in order to determine the extraction and acceleration coefficients, α and β, of the various ions considered in the discharge. The model makes use of a numerical simulation tool called ZDPlaskin (Zero-Dimensional Plasma Kinetics solver) [42]; this package was developed by researchers at LAPLACE (Laboratoire des Plasmas et Conversion d'Energie). It is composed by set of numerical routines written in Fortran, useful to interpret and compile large kinetic schemes common to molecular plasma discharges.

Given the kinetic scheme, consisting of all the relevant chemical and physical processes, the utility is able to:

- compute rates of chemical processes, performing also integration of cross sections with Maxwell and non-Maxwell electron distribution function;
- compute rates of variation of chemical species and determine time evolution of the species densities.

Plasma-chemical problems are known to be *stiff*; unfortunately the DVODE F90 solver routine, implemented by ZDPlaskin for the time evolution integration of the chemical species, is not robust enough to solve the majority of plasma-chemical problems that we submitted to it; for this reason we decided to handle the numerical integration of the differential equations in Matlab environment. In these conditions numerical integration of the electron energy equation was too far time consuming to be feasible, therefore the electron temperature was considered an input parameter of the model; however, this is acceptable since the objective of the work is a comparison between different gases, and the model is able to provide useful informations for this purpose.

The model is then fed to the genetic algorithm optimization toolbox, in Matlab environment, in order to find *optimum* efficiency configurations in terms of thruster performances; the target of the optimization is a thrust level of 5 mN, with maximization of thruster efficiency.

3.2.1 Kinetic scheme

Tables of the implemented kinetic schemes, along with rate constants and references for the plasma chemical reactions, are reported in appendix.

Integration of cross sections with a Maxwellian distribution is performed by *Bolsig+* (Electron Boltzmann Equation Solver), utility embedded in the ZDPlaskin package. For each gas a discharge model has been developed, table[3.4] reports all the species considered for each model.

Most of the cross section are taken from the *LXcat online database*[43]; O_2 and N_2 kinetic schemes were based on the work reported in [44], where reactions mostly comes from [25].

3.2.2 Results

The purpose of these simulations is to compare different gases in terms of propulsive performances for the HPT thruster. The axial magnetic field strength is fixed to a value of 1100 Gauss in order to ensure an adequate confinement for the resulting source pressures, and the cross diffusion of charged particles is assumed to follow the classic ambipolar formulation.

The input parameters of the model are the gas mass flow rate, the geometrical dimensions of the chamber, the throat-to-chamber section ratio, and the electron temperature within the plasma source. Each model is embedded into the genetic algorithm toolbox

TABLE 3.4: Species considered for each model

GAS	SPECIES					
H_2	H_2	$H_2(B^1)$	$H_2(A^3-C^3)$			
	H	$H(_2s)$	$H(_2p)$			
	H_3^+	H_2^+	H^+			
N_2	N_2	$N_2(A^3)$	$N_2(B^3)$	$N_2(a'^1)$	$N_2(C^3)$	
	N	$N(_2D)$	$N(_2P)$			
	N_2^+	N^+				
O_2	O_3	O_2	$O_2(a^1)$	$O_2(b^1)$	$O_2(_4 \cdot 5\,eV)$	
	O	$O(_1D)$	$O(_1S)$			
	O_4^-	O_3^-	O_2^-	O^-		
	O_4^+	O_2^+	O^+			
N_2O	N_2O	N_2	O_2	NO		
	O	$O(_1D)$	N	$N(_2D)$		
	N_2O^+	N_2^+	O_2^+	NO^+	O^+	
CO_2	CO_2	CO	O_3	O_2	C	
	$O_2(a^1)$	$O_2(b^1)$	$O_2(_4 \cdot 5\,eV)$	O	$O(_1D)$	$O(_1S)$
	O_4^-	O_3^-	O_2^-	O^-		
	CO_2^+	CO^+	O_4^+	O_2^+	O^+	C^+

1. $H_2(A^3-C^3)$ is a generic excited state comprehensive of both the $H_2(A^3\Sigma)$ and $H_2(C^3\Pi)$ states.
2. $O_2(_4 \cdot 5\,eV)$ is a generic excited state representative of $O_2(A^3\Sigma)$, $O_2(C^3\Delta)$, $O_2(c^1\Sigma)$ states.

TABLE 3.5: Range of variation of the input parameters for genetic optimization.

	R (cm)	L (cm)	ϱ^*	$\dot{m}$ kg/s	T_e (eV)
Upper Limit	3.0	8.0	1.0	$5 \cdot 10^{-7}$	10
Lower Limit	1.0	15.0	0.2	$5 \cdot 10^{-8}$	3

under Matlab environment, in order to find best performing configurations. The input parameters are changed within the genetic algorithm in order to maximize efficiency targeting a thrust level of 5 mN. The range of variation of the input parameters are chosen close to the developed HpH.com experiment, for consistency. Table(3.5) shows the range of variation of the input parameters for the optimization process.

Table[3.6] reports the thruster geometry and operation parameters resulting from the optimization process, table[3.7] reports the discharge properties, source pressure, electron density, ionization degree and dissociation degree resulting from the simulations run with the optimized parameters, and table[3.8] reports the propulsive performances resulting from these configurations. Results shows CO_2 and N_2O perform well, while H_2 is the worst performing because of the high cost of molecule excitation, dissociation and ionization.

TABLE 3.6: Optimized thruster parameters.

GAS	R (cm)	L (cm)	ϱ^*	$\dot{m}$ (kg/s)	T_e (eV)
H_2	1.4	11.8	0.67	$1.10 \cdot 10^{-7}$	9.6
O_2	1.8	12.5	0.93	$3.20 \cdot 10^{-7}$	6.1
N_2	1.2	13.6	0.95	$1.75 \cdot 10^{-7}$	7.9
N_2O	2.7	12.1	0.79	$3.02 \cdot 10^{-7}$	6.6
CO_2	2.3	14.8	0.83	$2.64 \cdot 10^{-7}$	5.4

TABLE 3.7: Thruster source chamber conditions.

GAS	Pressure (mTorr)	Ionization	Dissociation	P_W (W)
H_2	5.24	0.015	0.51	482
O_2	1.72	0.104	0.84	109
N_2	1.73	0.210	0.80	127
N_2O	1.12	0.070	0.78	89
CO_2	0.50	0.41	0.62	93

TABLE 3.8: Propulsive performances.

GAS	Thrust (mN)	I_{SP} (s)	η_P
H_2	4.35	4005	0.18
O_2	4.71	1489	0.32
N_2	4.64	2699	0.48
N_2O	4.42	1698	0.46
CO_2	5.20	1997	0.55

Higher neutral gas temperature are to be expected in molecular plasma because electron impact dissociation processes are exothermic and heat the gas. During the simulations the neutral gas temperature has been set to $1000K$; this value has been chosen based on approximate calculations with a previous developed model that implements a neutral gas energy equation [11]; however, it has to be pointed out that as the resulting chamber pressure spans 1 - 6 mTorr, the gas temperature affects weakly the chemistry of the discharge.

Absorbed power curves for each gas are reported in figure[3.12]; note that, since the electron temperature it's been held constant, the power at any time equals the power losses within the discharge, and depends on the time varying gas composition of the discharge.

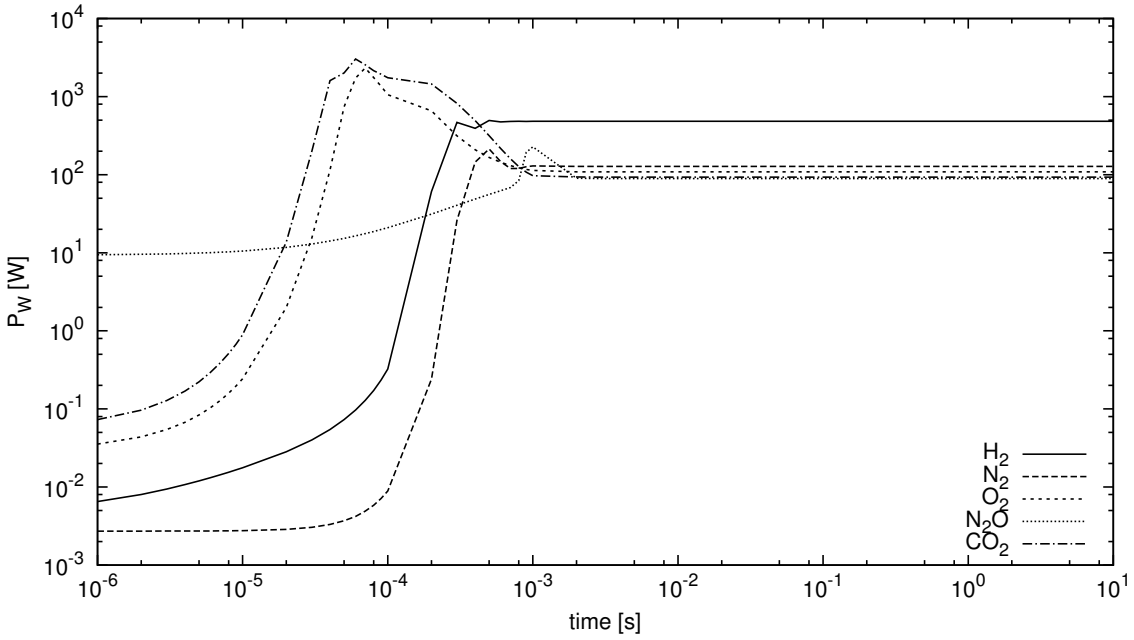

FIGURE 3.12: Absorbed power time profile of the optimized configurations.

The overshoot of power at the beginning of the transient of the discharge is a consequent of the constant electron temperature; it is due to the loss of energy by electron vibrational excitation of the molecules and to build up of electron population. Almost simultaneously, dissociation by electron impact reduces the number of molecules within the discharge, and making so, it reduces the sink terms associated to electron vibrational excitation. Figure[3.13] reports the absorbed power, the electron density and the dissociation within the N_2O discharge in the overshoot region; it can be seen that as the electron density increase within the discharge, also the expended power increases. Dissociation follows with small delay and has a peak when the power it's already decreased.

As example of the transient evolution of the species density within the discharge, we report time profiles for the simulation of the N_2 case in figure[3.14] Initial conditions are set as $10^{18}m^{-3}$ for N_2 ground state and $10^{10}m^{-3}$ for all the other species.

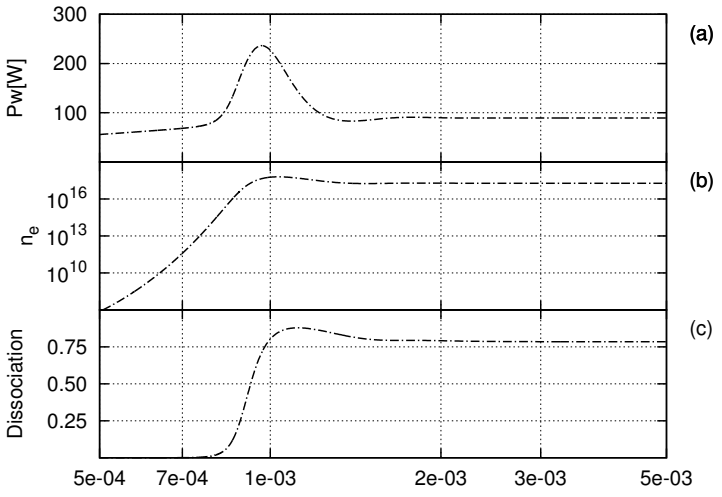

FIGURE 3.13: Absorbed power time profile (a), electron density (b) and dissociation (c) within the N_2O discharge.

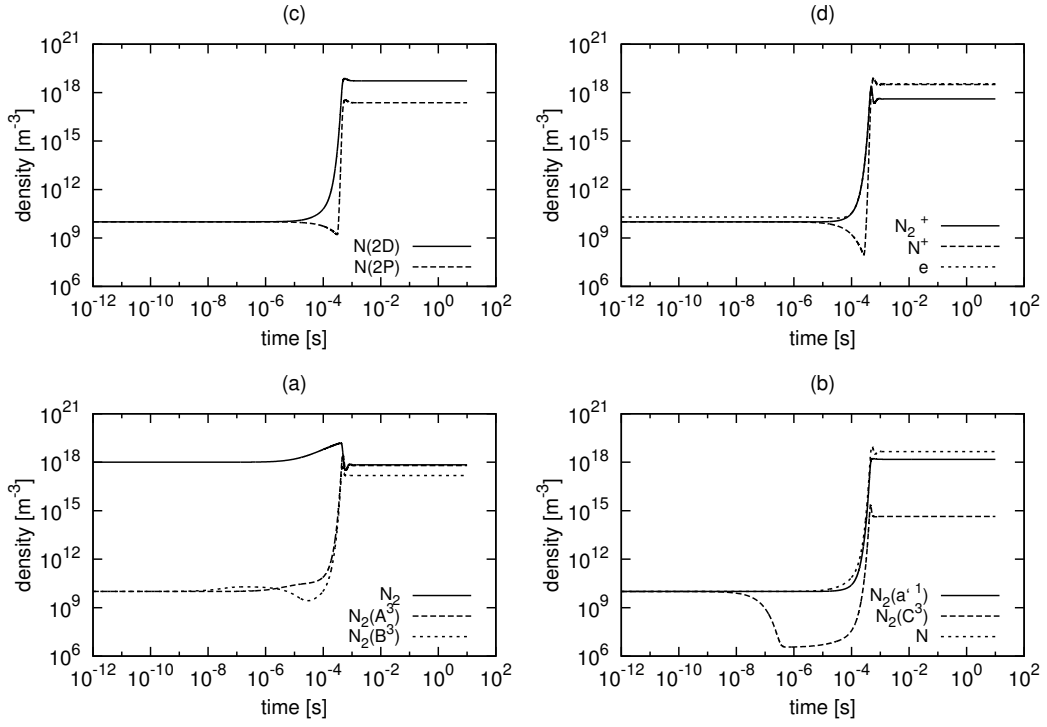

FIGURE 3.14: Species density transient for N_2 optimized configuration simulation: (a) N_2, $N_2(A^3)$, $N_2(B^3)$; (b) $N_2(a'^1)$, $N_2(C^3)$, N; (c) $N(_2D)$, $N(_2P)$; (d) N_2^+, N^+.

3.3 CO2 Thruster Model

The previous section described a preliminary evaluation of the thruster performance with different propellants, a work performed within the AO7048 program. The end of the program resulted in the identification of CO_2 as well performing propellant and interesting from the point of view of the recent interest of the space community in Mars related space missions. The SAPERE-STRONG program, funded by the Italian Ministry for University and Research (MIUR), starts on the results of the previous AO7048 and HpH.com programs and aims to develop a kW-level plasma thruster operating with Ar and CO_2. The propulsive objectives of the program include: (1) the design and construction of a prototype thruster working at a power level between 1 and 1.5 kW, a thrust level between 75 an 100 mN with a specific impulse $I_{SP} > 2000$ s; (2) numerical investigation and design of a HPT thruster working in the 5 kW power range. The program is actually under development.

In order to perform the necessary studies and analysis, we developed a plasma chemical model for a magnetized CO_2 discharge to apply to the thruster system. The model is more detailed than the one presented in the previous section , and it incorporates an electron energy equation in order to properly account for the injected power into the system. In this case we implemented also an energy equation for the neutral and ion particles in order to have an estimation of the gas temperature within the discharge.

Several works on plasma kinetic modelling for CO2 have been published; plasma chemical reactions for CO_2 discharges can be found in papers dedicated to CO_2 lasers[45, 46] and thermal-plasma discharge modelling [47]. Rusanov, Fridman *et al.* [48] have worked on CO_2 plasma assisted dissociation in the 1980s; CO_2 dissociation can be useful for CO_2 sequestration for environmental issues, and for fuel conversion[18]. There has been a renew interest on these topics recently; Bogaerts's group [49, 50] have published detailed kinetic schemes for CO_2 plasma discharges. These works concern sub-atmospheric and atmospheric discharges, where bulk chemical reactions play a major role, they do not take into account wall diffusion and magnetic confinement effects.

Authors in [6] developed a global model for CO_2 thrusters, that can be used to estimate discharge chemical composition given a set of discharge parameters, as the electron temperature and the source pressure. However, their model lacks some more appropriate features, the capability to account for input parameters as the mass flow rate or the electrical power, the latter is due to the fact that T_e does not results from the solution of a time varying equation, and P_W is not an input of the model, rather, it results from the computation of the losses of the discharge given a specific value of T_e (the same approach followed in the multi-species model of the previous section); also, it seems they

use diffusion formulas that don't account for electronegativity and magnetic confinement of the plasma. Finally their model does not account for magnetic detachment in helicon thruster [2] or any modelling of the thruster plume.

We developed a model for electronegative magnetized discharges that uses the reactions listed in the above reported papers, and considers wall diffusion and magnetic confinement effects, which are important at low pressures; extraction and acceleration coefficients , α and β, are used to account for particles and energy losses at the exhaust plume of the thruster.

The first part of this section describes the kinetic scheme and the species considered in the discharge model; the second part reports the validation of the model. Then we proceed with an investigation of the propulsive performances varying the thruster parameters, in the low power and high power range; at the end we present the results of the optimization projections for the high power thruster that will be constructed in the final phase of the project.

3.3.1 Kinetic scheme

The considered species are listed in table[3.9]. CO_2 and CO electronic excited levels are considered following the same approach presented in [50]; regarding CO_2 electronic excitation we consider two electronic excited states, namely $CO_2(e_1)$ and $CO_2(e_2)$, that corresponds to the cross sections reported by Lowke and Phelps [51]. Authors in [50] identified e_1 and e_2 states as $CO_2(^1\Pi)$ and $CO_2(^1\Delta)$.

Regarding CO electronic excitation we consider four electronic excited states, $CO(A^1\Pi)$, $CO(a^3\Pi)$, $CO_2(e_1)$ and $CO_2(e_2)$; $CO_2(e_1)$ is a group of four different singlet states, $CO(I^1\Sigma)$, $CO(B^1\Sigma)$, $CO(C^1\Sigma)$ and $CO(E^1\Pi)$; $CO_2(e_2)$ is a group of four triplet states, $CO(a'^3\Sigma)$, $CO(d^3\Delta)$, $CO(e^3\Sigma)$ and $CO(b^3\Sigma)$. Cross sections for excitation of the CO states are reported by Liu [52].

Electron impact reactions are reported in table[A.7] in appendix, cross sections are integrated over a Maxwellian electron distribution function. Electronically excited states can have a stimulated ionization, i.e. the activation barriers of ionization and dissociation are lowered as a consequence of the higher energy level of the excited reactants[50]; cross sections for ionization and dissociative ionization proceeding from excited reactants are obtained from the relative ground state cross sections lowering the impact energy by the relative excited state electronic energy, $\sigma_{ex} = \sigma_{ground}(U - \varepsilon_{ex})$.

Dissociative ionization of CO_2 appears to be one of the major contribution to heating of the gas; the implemented cross sections give no indication regarding the excitation state

TABLE 3.9: Species considered for the CO_2 model

GAS	SPECIES					
CO_2	CO_2	$CO_2(e_1)$	$CO_2(e_2)$	CO_2^+		
	CO	$CO(A^1\Pi)$	$CO(a^3\Pi)$	$CO(e_1)$	$CO(e_2)$	CO^+
	O_2	$O_2(a^1)$	$O_2(b^1)$	$O_2(_4 \cdot 5\,eV)$	O_2^+	O_2^-
	O	$O(_1D)$	$O(_1S)$	O^+	O^-	
	C	C^+	O_4^+	O_4^-	O_3	O_3^-

1. $CO_2(e_1)$ and $CO_2(e_2)$ corresponds to $CO_2(^1\Pi)$ and $CO_2(^1\Delta)$.
2. $CO(e_1)$ is a generic excited state representative of $CO(I^1\Sigma)$, $CO(B^1\Sigma)$, $CO(C^1\Sigma)$, $CO(E^1\Pi)$.
3. $CO(e_2)$ is a generic excited state representative of $CO(a'^3\Sigma)$, $CO(d^3\Delta)$, $CO(e^3\Sigma)$, $CO(b^3\Sigma)$.
4. $O_2(_4 \cdot 5\,eV)$ is a generic excited state representative of $O_2(A^3\Sigma)$, $O_2(C^3\Delta)$, $O_2(c^1\Sigma)$ states.

of the products; assumptions on the the excitation state of the products are necessary, in order not to add electronic excitation energy to the gas neutral energy equation. We refer to the work of Locht and Davister[53] in order to estimate the energy released for each one of the dissociative ionization processes. The authors used photo-ion and photo-electron impact techniques and mass spectrometry in order to determine the appearance energy and the products of dissociative ionization impacts on CO_2 target molecules. They observed three channels:

1. The CO^+ channel is observed with AE (appearance energies) of 19.56, 22.18, 23.9, 26.1, 30.4 eV. The authors assign the 26.1 threshold to the process $CO_2 \rightarrow CO^+(X^2\Sigma) + O(_3P)$, both products appear in their ground state. The implemented cross section from Itikawa[54], has a threshold of 26.41 eV; we assign this process to the CO^+ dissociative ionization cross section.

2. The O^+ channel is observed with AE of 19.04, 22.21, 24.74, 30.32 eV. The authors assign the 30.32 threshold to the process $CO_2 \rightarrow O^+(_4S) + CO(A^1\Pi)$, in this case only the oxygen ion is produced in its ground state. The implemented cross section from Itikawa has a threshold of 29.1 eV; we assign this process to the O^+ dissociative ionization cross section.

3. The C^+ channel is observed with AE of 23.04, 25.3, 26.9, 28.3, 29.2, 31.27 eV. The authors assign the 31.27 threshold to the process $CO_2 \rightarrow C^+(_4P) + O_2(a^1\Delta[v=0-3])$. The implemented cross section from Itikawa has a threshold of 33.68 eV; we assign this process to the C^+ dissociative ionization cross section.

The energy loss for electron-ion recombination is assumed to be the average electron energy $\varepsilon = (3/2)\mathrm{T_e}$; when the process results in formation of a single particle, the excess energy is radiated away; if the process results in dissociation of the ion, there is a transfer of energy to the heavy particles that we estimate as the difference between the average electron energy and the enthalpy balance of the reaction, $(3/2)\mathrm{T_e} - \delta h_0$. There is a transfer of energy to the heavy particles also in third body electron-ion recombination, the exceeding energy is carried away by the third body[7]. Attachment is a resonant process with threshold energy, ε_{th}, that involves electrons in a narrow energy range[7]. Heating of the gas results with dissociative attachment, the energy released is $\varepsilon_{th} + \varepsilon_{aff} - \varepsilon_{diss}$, with ε_{aff} and ε_{diss} the electron affinity and the dissociation energy of the molecule; energy release can results also in third body attachment reactions, where the excess energy is carried away by the third body.

Table[A.8] reports reaction rates for electron detachment, charge exchange reactions and ion-ion reactions. We assume, for simplicity, that electrons are created at zero energy in detachment processes. Table[A.9] reports reaction rates for metastable activation and deactivation reactions, and neutral gas phase reactions. Main source for neutral gas phase processes is NIST kinetic database[55]. Several neutral gas phase reaction rates, not available in the database, are calculated from the corresponding reverse reaction with the law of mass action and the assumption of thermodynamic equilibrium, as explained in [16].

3.3.2 Validation

Validation of the model has been performed with the experimental data obtained from characterization of the plasma source operated with CO_2 and described in section[4]. In the experimental characterization, the plasma thruster is fed with CO_2 gas, a magnetic field is applied, with an average axial value of about ~ 700 Gauss; the source chamber is constituted by a cylindrical pyrex tube of 19 mm inner diameter; the chamber length is 140 mm, sufficient to accommodate the RF exciting antenna and the plasma diagnostic (i.e. microwave interferometer and optical fiber to collect the spectra). In the experiment, optical emission spectroscopy analysis is performed on the plasma spectra, electron density is measured by microwave interferometry and the electron temperature is estimated by absolute irradiance measurements.

The test matrix is composed by eight cases at three different mass flow regimes, and different power levels; the source configuration and test conditions are reported in table[4.4] and table[4.5].

TABLE 3.10: Experimental CO_2 test matrix; source configuration is radius $R = 9.5$ mm, length $L = 140$ mm, nozzle section ratio $\varrho^* = 0.07$; magnetic field $B \sim 700$ Gauss.

Test	Mass Flow Rate [mg/s]	Deposited Power [W]
01	0.25	36
02	0.25	72
03	0.25	132
04	0.13	33
05	0.13	62
06	0.18	54
07	0.18	81
08	0.18	133

Running the CO_2 model with an effective cross diffusion coefficient, D_R, defined by the same λ parameter obtained in section[Ar validation], $\lambda = 0.3$, a very good agreement with the experimental data is obtained.

Table[3.11] compares the experimental and numerical values of the electron density and electron temperature for each test case. We see from table[3.11] that simulated electron densities are within a factor 0.6 - 1.5 to the measured ones, and electron temperatures are within a factor 0.9 - 1.1 to the estimated ones.

TABLE 3.11: Comparison between numerical and experimental values for electron densities and temperatures.

Test	n_e (measured) [m^{-3}]	n_e (calculated) [m^{-3}]	T_e (estimated) [eV]	T_e (calculated) [eV]
01	$1.2 \cdot 10^{+18}$	$7.5 \cdot 10^{+17}$	2.0	2.1
02	$2.5 \cdot 10^{+18}$	$1.5 \cdot 10^{+18}$	2.0	2.1
03	$3.8 \cdot 10^{+18}$	$3.0 \cdot 10^{+18}$	2.0	2.1
04	$8.0 \cdot 10^{+17}$	$1.1 \cdot 10^{+18}$	2.5	2.2
05	$1.4 \cdot 10^{+18}$	$2.2 \cdot 10^{+18}$	2.5	2.4
06	$2.4 \cdot 10^{+18}$	$1.4 \cdot 10^{+18}$	2.1	2.2
07	$3.4 \cdot 10^{+18}$	$2.2 \cdot 10^{+18}$	2.1	2.2
08	$4.3 \cdot 10^{+18}$	$3.9 \cdot 10^{+18}$	2.1	2.3

The neutral thermal decomposition scheme (the neutral gas phase reactions set), has also been validated by closed volume steady state simulations, at temperatures in the range 1000-5000 K; results has been compared with equilibrium compositions calculated with CPROPEP software[56]. Steady state compositions have been found in agreement with CPROPEP within 0.01%; as example we report in figure[3.15] the time evolution of the concentration of the neutral species versus the equilibrium composition resulting from CPROPEP, of CO_2 at 5000 K temperature and 1.97 bar pressure. As the simulation time proceeds, the time varying concentrations approach the equilibrium values of obtained with CPROPEP.

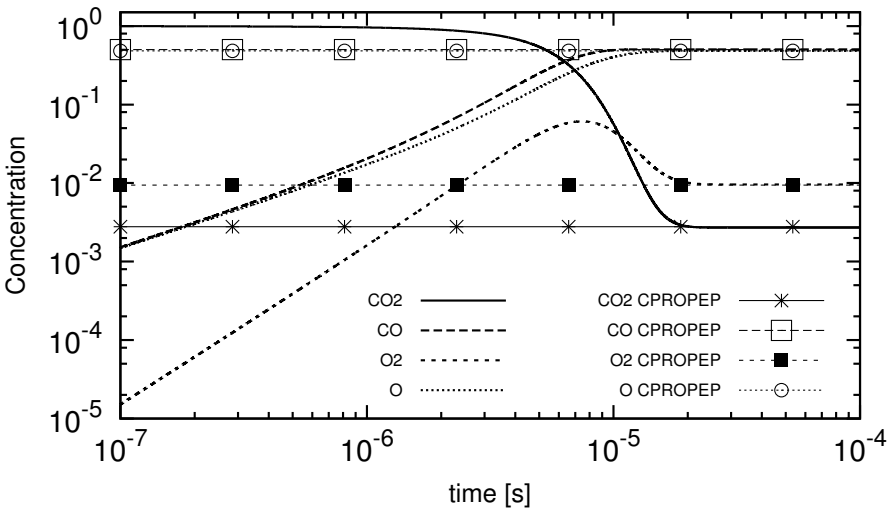

FIGURE 3.15: Thermal decomposition scheme: time evolution concentrations(kinetics) versus equilibrium composition(CPROPEP). Simulation at 5000K, 1.97 bar.

3.3.3 Propulsive performances

The same considerations drawn for Argon in section [3.1.3] and [3.1.4], should hold for CO_2, keeping in mind that, being CO_2 a molecular gas, we expect higher power losses due to vibrational excitation and electron impact dissociation; the former being relevant at lower electron temperatures and the latter at higher electron temperatures. We expect a considerable heating of the gas due to energy liberated in electron impact dissociation processes; a high gas temperature can give a minor contribution to the overall thrust, especially at low ionization degrees.

In this section we show simulations at three power regimes: (1) low power regime simulations, 50 - 200 W, which is in the same power range of the experimental tests in section[CO2 test]; (2) medium power regime, 1 - 1.5 kW, which is the power range of design and construction of a prototype HPT thruster for the STRONG-SAPERE program; (3) high power regime, 5 kW, which is the power range of numerical investigation and design of a HPT thruster for the same program.

In order to obtain good thruster performances, high electron temperatures and ionization degrees are necessary; these can be achieved at low pressures exploiting the confinement capability of the magnetic field.

Low power regime simulations: we fix the magnetic field to the value of 700 Gauss, the source length and diameter to 140 mm and 19 mm respectively, as in the experimental conditions, and change the power input in the discharge from 50 to 200 W; different chamber pressures can be achieved with different values of the exhaust-to-chamber ratio

ϱ^*. Propulsive performances for a mass flow rate of 0.1 mg/s and 0.2 mg/s, are reported in figure[3.16] and figure[3.17] respectively; in the simulations, chamber pressure ranges between 0.5 and 5 mTorr.

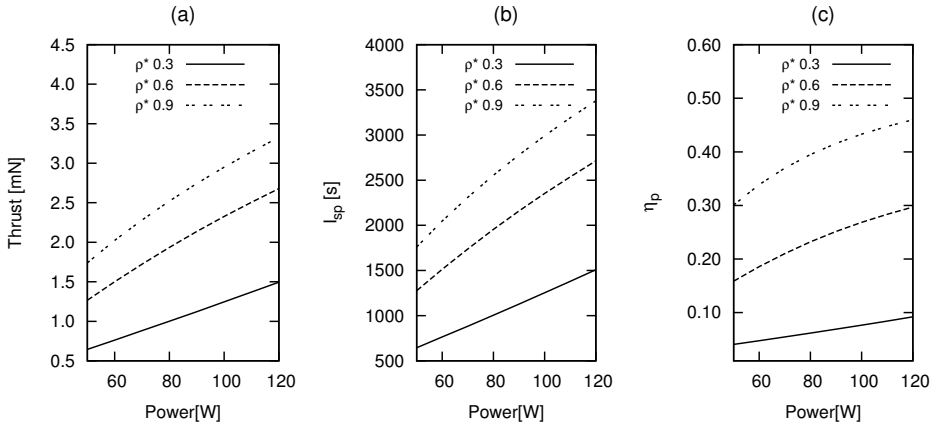

FIGURE 3.16: Thrust(a), specific impulse(b) and propulsive efficiency(c): variation versus power input, for different values of ϱ^*; numerical values are obtained for a fixed CO_2 mass flow rate of 0.1 mg/s, magnetic field, source length, and diameter are 700 Gauss, 140 mm and 19 mm.

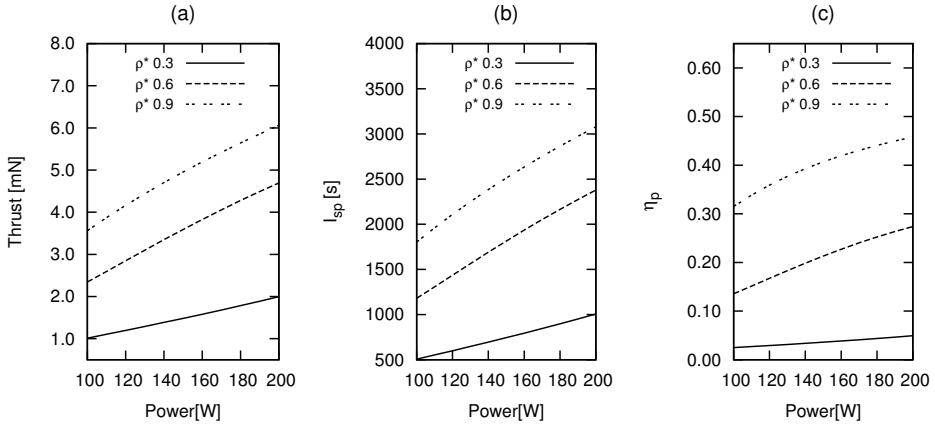

FIGURE 3.17: Thrust(a), specific impulse(b) and propulsive efficiency(c): variation versus power input, for different values of ϱ^*; numerical values are obtained for a fixed CO_2 mass flow rate of 0.2 mg/s, magnetic field, source length, and diameter are 700 Gauss, 140 mm and 19 mm.

Figure[3.18] reports the electron temperature and the neutral temperature for the 0.2 mg/s case, neutral temperature shows in the range 1000-3000 K degrees; figure[3.19] reports, for the same case, the ionization degree and the electronegativity, which results less than $2 \cdot 10^{-4}$, and figure[3.20] reports the fraction of the collisional to total expended power, and the resulting Θ parameter, which span from 0.2 - 0.6 pW. Finally, in figure[3.21], we shows the fraction of thrust due to high temperature gas, over the total thrust provided by the thruster, for the two cases; at low power, where the ionization is low, and at high pressures ($\varrho^* = 0.3$), the thrust from neutral particles is $\sim 30\%$ of the

total thrust; as the pressure decreases and the ionization degree increases, the fraction becomes negligible.

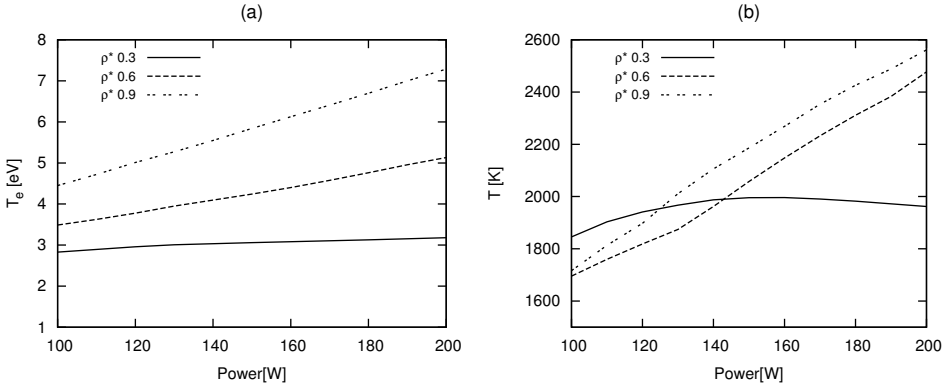

FIGURE 3.18: Electron temperature(a) and neutral temperature(b): variation versus power input, for different values of ϱ^*; numerical values are obtained for a fixed mass flow rate of 0.2 mg/s, magnetic field, source length, and diameter are 700 Gauss, 140 mm and 19 mm.

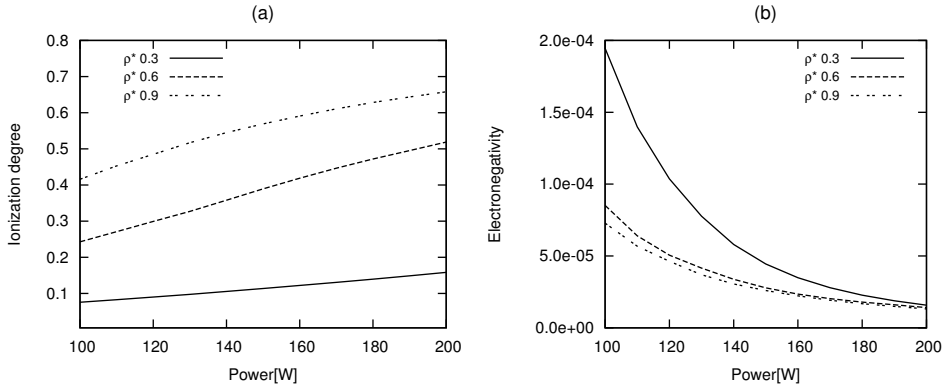

FIGURE 3.19: Ionization degree(a) and electronegativity(b): variation versus power input, for different values of ϱ^*; numerical values are obtained for a fixed mass flow rate of 0.2 mg/s, magnetic field, source length, and diameter are 700 Gauss, 140 mm and 19 mm.

Medium-High power regime simulations: we performed simulations at medium (1-1.5 kW), and high (4.5-5 kW) power regimes; average magnetic field strength is set to 1100 and 1500 Gauss respectively. Chamber dimensions and mass flow rates parameters are set based on the results obtained with genetic algorithm optimization; they are reported in table[3.12]. Propulsive performances are reported in figure[3.22] and figure[3.23]; chamber pressure ranges between 2 and 15 mTorr; pressure variation is achieved with different values of the exhaust-to-chamber ratio ϱ^*.

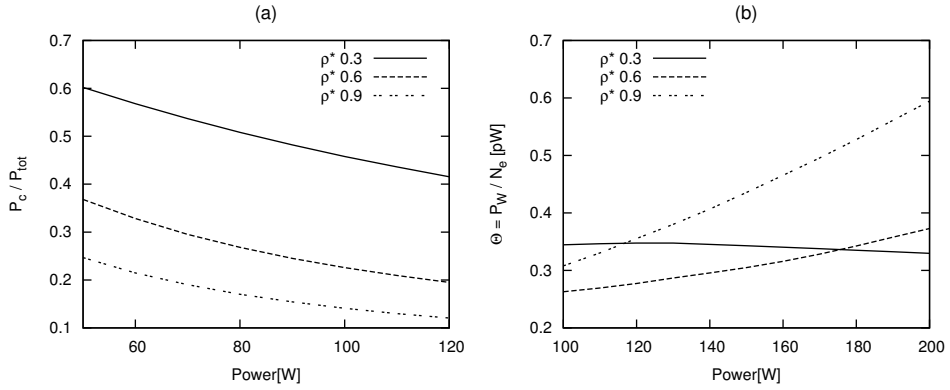

FIGURE 3.20: Fraction of the collisional to total expended power (a), and the Θ parameter (b): variation versus power input, for different values of ϱ^*; numerical values are obtained for a fixed mass flow rate of 0.2 mg/s, magnetic field, source length, and diameter are 700 Gauss, 140 mm and 19 mm.

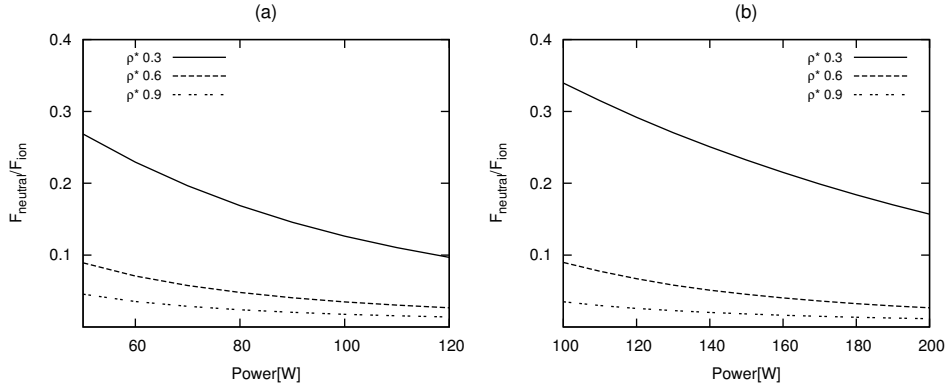

FIGURE 3.21: Fraction of thrust due to high temperature gas, over the total thrust, for 0.1 mg/s case (a) and 0.2 mg/s case (b); variation versus power input, for different values of ϱ^*; numerical values are obtained for a magnetic field, source length, and diameter are 700 Gauss, 140 mm and 19 mm.

TABLE 3.12: CO_2 high power regime simulations parameters.

	Chamber Radius [mm]	Chamber Length [mm]	Mass Flow Rate [mg/s]	Magnetic field [Gauss]
1.0 - 1.5 kW	160	30	1.6	1100
4.5 - 5.0 kW	190	50	7.0	1500

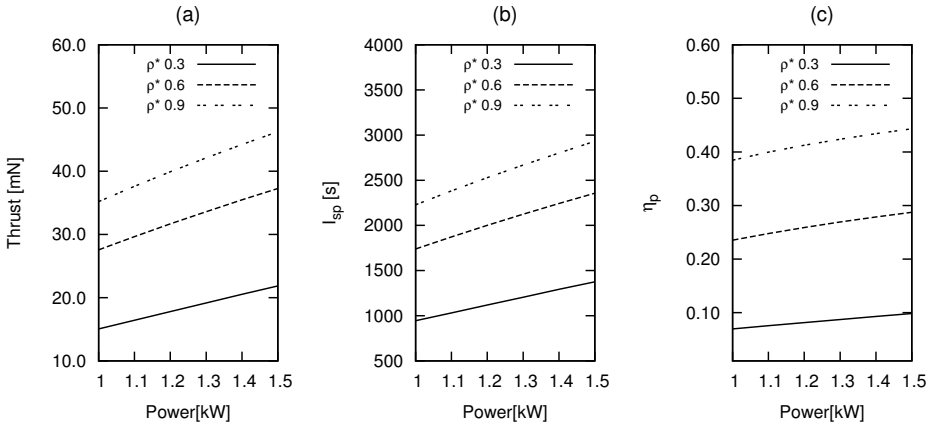

FIGURE 3.22: Thrust(a), specific impulse(b) and propulsive efficiency(c): variation versus power input, for different values of ϱ^*; numerical values are obtained for a fixed CO_2 mass flow rate of 1.6 mg/s, magnetic field, source length, and diameter are 1100 Gauss, 160 mm and 60 mm.

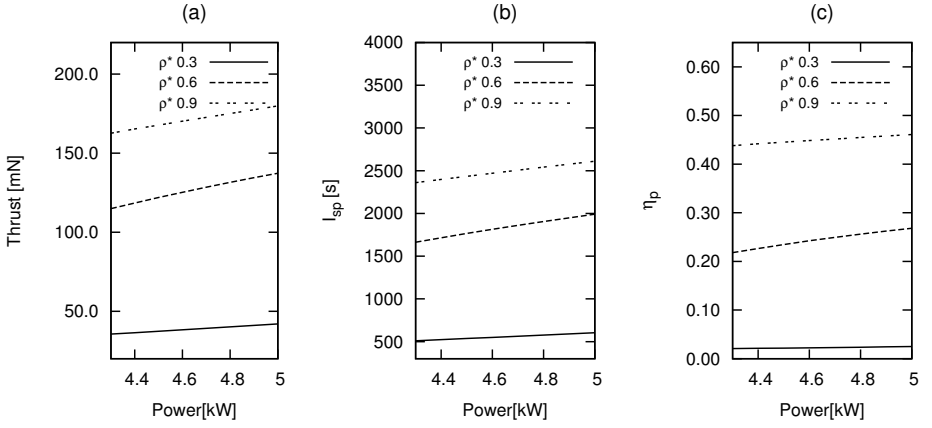

FIGURE 3.23: Thrust(a), specific impulse(b) and propulsive efficiency(c): variation versus power input, for different values of ϱ^*; numerical values are obtained for a fixed CO_2 mass flow rate of 7.0 mg/s, magnetic field, source length, and diameter are 1500 Gauss, 190 mm and 100 mm.

Chapter 4

Thruster Source Experimental Charachterization

In this chapter we describe the experimental measurements carried out at the high vacuum facility available at the Centre for Space Research (CISAS) at University of Padova.

A schematic of the experimental set-up is proposed in Figure[4.1]; with reference to Figure[4.1], from left to right, a gas injection system, provided with pressure gauges and mass flow controller, injects a stream of gas in a cylindrical Pyrex tube, where the plasma discharge is realized; the excitation antenna and the magnetic system are wrapped around the Pyrex tube; the ionized gas is then expelled through an expansion bell which connects to a vacuum chamber (2 m length, 0.6 m diameter) where the gas is pumped out by the vacuum pumping system.

The entire system is operated under continuous mass flow in order to simulate thruster operations. The build up pressure within the plasma discharge (the Pyrex tube) ranges from 20-60 mTorr, depending on the imposed gas flow rate. During source operation, the pressure inside the vacuum chamber, where the gas is exhausted, is maintained below $7 \cdot 10^{-2}$mTorr (10^{-4} mbar).

An interchangeable ceramic diaphragm is placed between the Pyrex tube and the expansion bell with the purpose of mechanically focusing the exiting gas and build up additional pressure within the discharge. The overall system was designed in order to be highly reconfigurable in terms of source length, outlet section diameter (diaphragm), and magneto-static field shape and intensity.

The first part of the chapter describes the plasma generation source, composed by an RF excitation antenna and the magnetic system, and the diagnostic composed by a

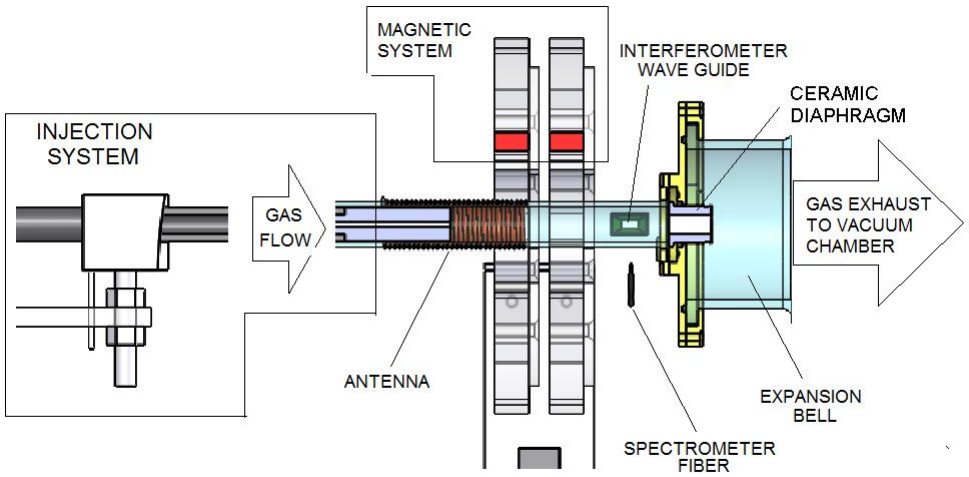

FIGURE 4.1: Experimental set-up configuration.

microwave interferometer and an optical spectrometer. The second part of the chapter describes the tests conducted with Ar and CO_2 gases; the measurement of the electron density is performed by microwave interferometry, previous estimation of the plasma column diameter; estimation of the electron temperature is performed by optical emission spectroscopy, with line ratio method for Ar and absolute irradiance for CO_2.

4.1 RF Antenna and Magnetic system

The key features of the system that were developed and optimized during the project HpH.com are the antenna and the magneto-static system. The magnetic system is necessary in order to provide confinement within the discharge and impart momentum to the exiting plasma beam (i.e. the so called magnetic nozzle effect). The design procedure, along with the experimental tests and numerical simulations, was aimed to achieve high plasma densities and high electrical power deposition efficiency.

The first antenna configuration was based on a simple four-loops helical antenna; this configuration was modified successively, during the HpH.com project, either in the number of loops and the shape of the antenna. The actual antenna is designed to operate in the range of frequency from 1.8 MHz to 30 MHz, and is currently under patenting procedure. The system includes a signal(RF) generator, a power amplifier, a custom-built matching device, the RF antenna, and a set of custom-built voltage and current probes. The latter can be placed along the RF network allowing estimation of both the power coupling and the complex impedance at different circuit locations.

The magnetostatic field has been initially generated by four electromagnets, independently powered in order to produce different field patterns with an intensity up to 1250 Gauss. Subsequently, they have been replaced by samarium-cobalt permanent magnets which can be arranged in several configurations, both with radial and axial magnetization; the use of permanent magnets allows for a passive and more compact design; more detailed informations on the RF antenna and the magnetic field optimization can be found in [57].

Figure[4.2] shows a schematic of the source with the positioning of the magnetic rings relative to the discharge tube and the RF antenna. In the figure, the intensity of the axial component of the magnetic field, along the source axis, is superimposed; the absolute maximum value is approximately 700 Gauss, the average value is about 400 Gauss, and the field presents an inversion of the axial component along the discharge tube.

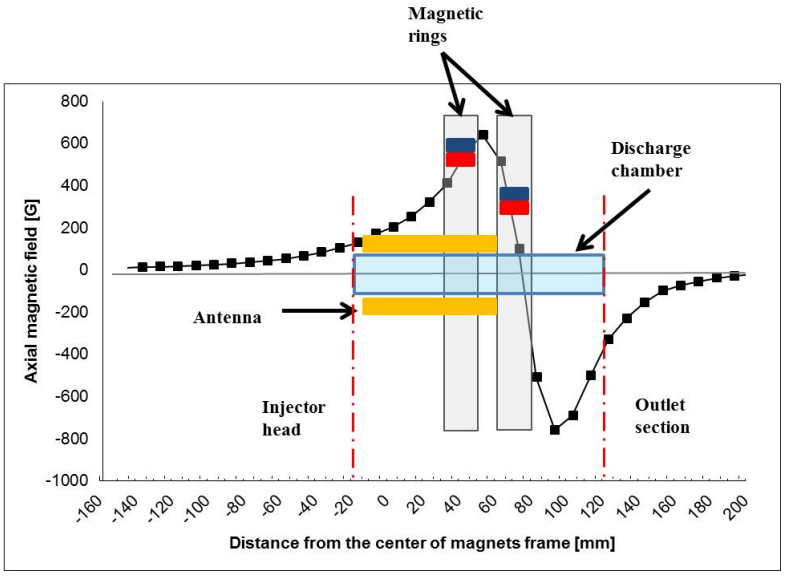

FIGURE 4.2: Magnetic system and its placement with respect to the plasma discharge, inlet and outlet sections; the system is comprised of two rings with radially-magnetized permanent magnets. The axial component of the magnetic field produced along the axis is superimposed.

4.2 Plasma Diagnostics

The experimental diagnostic is constituted by a microwave interferometer and an optical spectrometer. The former allows the evaluation of the plasma density, whereas the latter allows an estimation of the electron temperature and an indication of the main excited species within the discharge.

The microwave interferometer was designed during the project HpH.com, and it is described thoroughly in [58]. The interferometer works with a 75 GHz microwave signal

modulated at 100 MHz frequency; it is capable of detecting electron density values ranging from $3 \cdot 10^{16}\mathrm{m}^{-3}$ to $7 \cdot 10^{19}\mathrm{m}^{-3}$ (cut-off density).

The optical spectrometer belongs to the Ocean Optics HR4000 series, characterized by a 3648 pixel CCD sensor; it operates in the 220-650 nm wavelength range, with a wavelength resolution $\delta\lambda \approx 0.118$ nm. An optical fiber collects the emission of the plasma through the 2.5 mm thick pyrex wall, whose UV-filtering effect has been accounted in the calibration phase of the instrument. The optical system was calibrated by means of an Ocean Optics DH2000 light source, featuring a deuterium lamp and a tungsten halogen lamp providing a known and stable calibration spectrum covering the operating range of the spectrometer; the lamp features a special SMA connector for optical fibers, in which a 2.5 mm thick pyrex slab was placed in order to reproduce the effect of the discharge chamber wall; because of the pyrex opacity in the UV region, the calibration was successfully carried out only in the 270-650 nm range, which was, however, sufficient for the identification of species and the estimation of electron temperature.

4.3 Experimental Tests and Results

The characterization of the plasma source is performed by determination of the electron density, identification of the line emission systems and estimation of the electron temperature by line ratio method. The electron density is determined by interferometric measurements, which relates the phase shift ($\Delta\phi$) experienced by the microwave signal, travelling through the plasma column, to the average electron density and the plasma column diameter by the following relation:

$$\Delta\phi = \frac{e^2}{4\pi c^2 \epsilon_0 m_e} \lambda D \bar{n}_e \tag{4.1}$$

Here m_e and e are the electron mass and charge, c is the speed of light, ϵ_0 is the vacuum permittivity, λ is the microwave wavelength, $\bar{n}_e$ is the average plasma density along the line of sight of the interferometer.

Equation(4.1) is valid within a 4% error up to a density of $1 \cdot 10^{19} m^{-3}$ and for a value of D ranging from 20 mm down to 8 mm; for higher densities and lower diameters the relation becomes nonlinear. However, ray tracing techniques[58] shows that a linear region is still present for $\bar{n}_e < 2 \cdot 10^{19} m^{-3}$, but with a different slope than equation(4.1). For $D = 6$ mm and $D = 7$ mm, we have the following relations:

$$\begin{aligned}\Delta\phi(6\text{mm}) &= 4 \cdot 10^{-20}\bar{n}_e \\ \Delta\phi(7\text{mm}) &= 6.5 \cdot 10^{-20}\bar{n}_e\end{aligned} \tag{4.2}$$

4.3.1 Column diameter estimation

The plasma column diameter is determined by processing filtered images of the discharge; we applied a band pass filter centered at 488±10 nm, which is peculiar of the strong emission[59] ArII[$^2D_{5/2}-^2P_{3/2}$].

The luminescence of the plasma is mostly confined in a cylindrical column around the axis of the discharge chamber; the charged particles appears to be tightly wrapped around the axis, while neutral excited species are allowed to diffuse through the volume of the Pyrex tube; Figure[4.3] shows filtered and unfiltered images of the discharge that explain this feature.

Previous experiments[57], have confirmed that the plasma cylindrical column feature, depends mainly on the outlet diaphragm diameter and the magneto-static field, while the mass flow rate and the power coupled by the antenna show no significant influence.

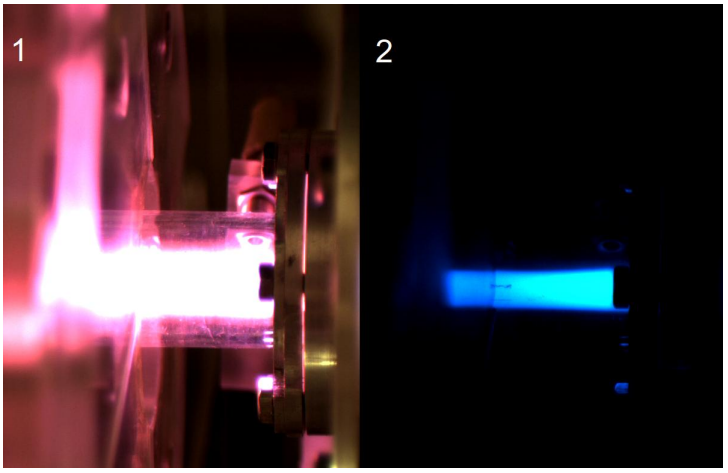

FIGURE 4.3: Unfiltered and filtered pictures of Ar discharge: (1) unfiltered image.(2) Filtered image at 488 nm.

A similar analysis has been performed here for the case of CO_2, employing the same filter. Since in CO_2 plasma the emission at 488 nm is typical of both ionized and excited species, we adopted the following procedure: (1) an unfiltered image was taken as reference, with the plasma turned off, in order to estimate the scale of the pictures; (2) a filtered image of only Ar plasma was taken with a power level of 50W in order to verify the configuration found in the previous Ar experiment; (3) at the same conditions

an image was taken of a 50% Ar, 50% CO_2 mixture plasma; (4) a third image of a pure CO_2 discharge.

In figure[4.4.2] Ar produces the aforementioned discharge structure, the blue emission is concentrated in the core; as the CO_2 percentage is raised, the outer zones of the volume are progressively filled with blue emissions, due to excited neutrals, however the strongest part of the emission is still concentrated in the core, indicating the region populated by the charged particles, figure[4.4.3] and figure[4.4.4].

Core diameters, ranging between 5-7 mm, were estimated in the zone covered by the interferometer waveguides, resulting in a mean value of 6 mm.

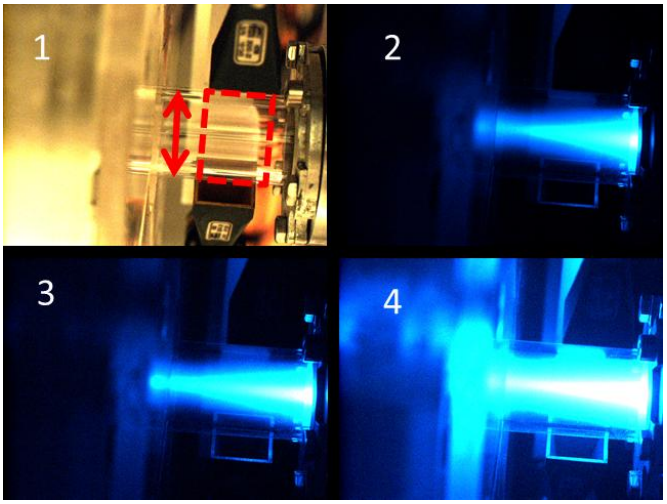

FIGURE 4.4: (1) Unfiltered reference frame. The red arrow evidences the external diameter of the discharge chamber (24 mm); the interferometer waveguides are visible, the zone covered by them is dashed. (2) Filtered image of Ar discharge. (3) Filtered image of Ar-CO_2 mixture. (4) Filtered image of pure CO_2 discharge.

4.3.2 Experiments with Ar gas

4.3.2.1 Ar electron temperature estimation

The plasma UV-Vis spectrum of our Argon discharges, is dominated by emission from the Ar first ionized states; an example of the acquired spectra is shown in Figure[4.5], for the second test case; test cases are reported in table[4.2] in the next paragraph. Several lines from the ArI excited state are detected also, together with few (not reported in the figure) from ArIII states. Note that the higher peak pertains to the selected ArII($^2D_{5/2}-^2P_{3/2}$) transition at 488 nm, for filtered imaging of the discharge.

An estimation of the electron temperature can be given by the line ratio procedure indicated by Boffard *et al.* [60]. The authors identify the line pair constituted by the

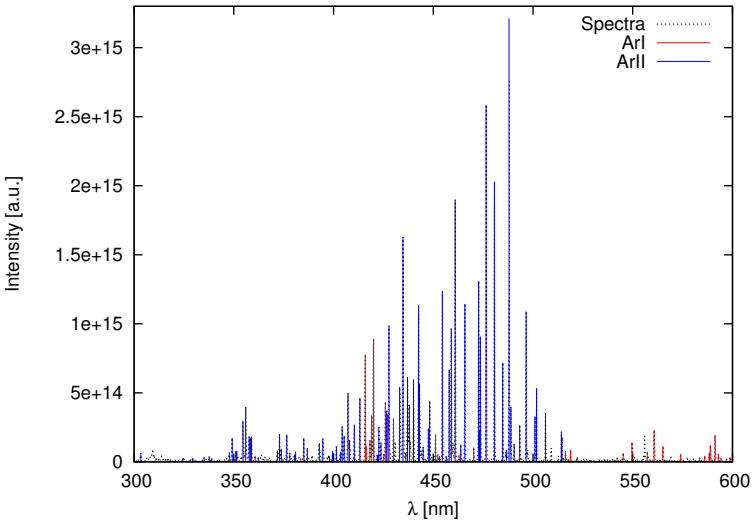

FIGURE 4.5: Emission spectra of Ar plasma for test case 2.

419.83 nm, ArI($5p\ [1/2]_0 - 4s\ [3/2]^o_1$), and 420.07 nm, ArI($5p\ [5/2]_3 - 4s\ [3/2]^o_2$) transitions, and implement them in an extended corona model; the model uses optical emission cross section and take into account the excitation produced from the ArI($4s\ [3/2]^o_2$) metastable state.

Note that such corona model depends (indirectly) on the electron density, which is responsible for the population of the metastable levels. The authors tested their model against experimental probe measurements in an ICP discharge reactor, obtaining good agreement with the data; the accuracy of this method, based on the probe measurements reported in their paper, is determined to be ±20%; they also compared the results with a more refined kinetic model (including excitation from other levels, radiation trapping, *etc.*), concluding that the increase in complexity follows a gain in accuracy of ±15%.

Assuming a Maxwellian electron distribution, and using the optical emission cross sections in [60], the integrated line intensities ratio is defined by:

$$\frac{I_{420}}{I_{419}} = \frac{K^0_{420}(\mathrm{T_e}) + (\mathrm{n_m/n_0})\mathrm{K^m_{420}(T_e)}}{K^0_{419}(\mathrm{T_e}) + (\mathrm{n_m/n_0})\mathrm{K^m_{419}(T_e)}} \tag{4.3}$$

Where n_m/n_0 is the ratio of metastable ($4s$) to ground population density, and $K(T_e)$ is the average, over a Maxwell distribution, of the optical emission cross section. The line pair ratio has a linear dependence on the metastable density in equation(4.3), it has a near exponential dependence on $\mathrm{T_e}$ (via excitation rates). As a consequence, when one uses the inverted relation to find $\mathrm{T_e}$ from the line pair ratio and metastable fraction, the results generally turn out to be less sensitive to the value of n_m/n_0 [60]; in this regard,

the authors reports that a 50% uncertainty on n_m/n_0 resolves to a 10% uncertainty on the determination of T_e.

The assumption of a Maxwell distribution was discussed in section[2.1.1]. Figure[4.6] shows the optical emission rate constants implemented in equation(4.3) and the integrated line intensity ratio as function of T_e, and for different values of n_m/n_0 in the range relevant to our work.

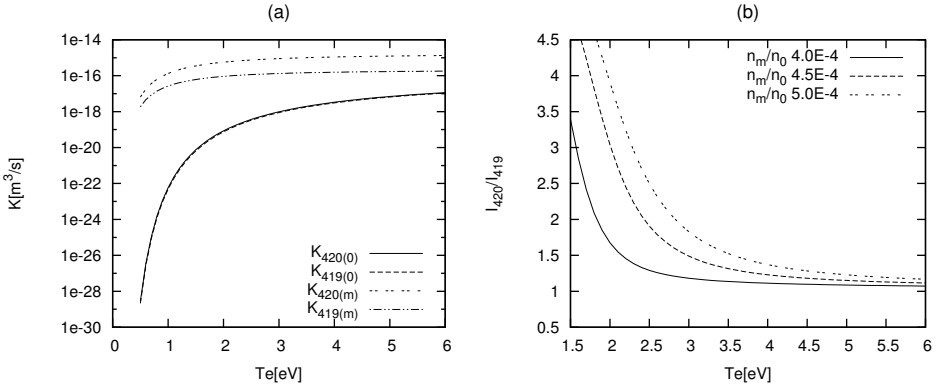

FIGURE 4.6: (a) Optical emission rates for a Maxwellian electron distribution; (b) integrated intensities line ratio for different values of n_m/n_0.

The spectrometer resolution allows to resolve separately the two wavelengths, 420.07 and 419.83, however there is partial overlap of the lines due to broadening mechanism. The major contribution to broadening affecting the two Ar lines, in these experimental conditions, is instrumental broadening; other broadening mechanism are negligible: natural broadening, estimated with formula in [61], is 10^{-5} nm order of magnitude; Doppler broadening, estimated with formula in [62], is 10^{-3} nm order of magnitude.

Instrumental broadening is described by a Gaussian profile[63], with I_0 the peak intensity and FWHM the full width at half maximum.

$$I_\lambda(I_0, \mathrm{FWHM}) = \frac{I_0}{\mathrm{FWHM}\left(\frac{\pi}{4\lg 2}\right)^{1/2}} \exp\left[-\frac{4\lg 2}{\mathrm{FWHM}^2}(\lambda-\lambda_0)^2\right] \tag{4.4}$$

We fit, in a least square sense, the sum of two line profiles to the experimental profile, as depicted in figure[4.7]; fitting parameters are the FWHW and the peak intensity of the 419 and 420 nm lines.

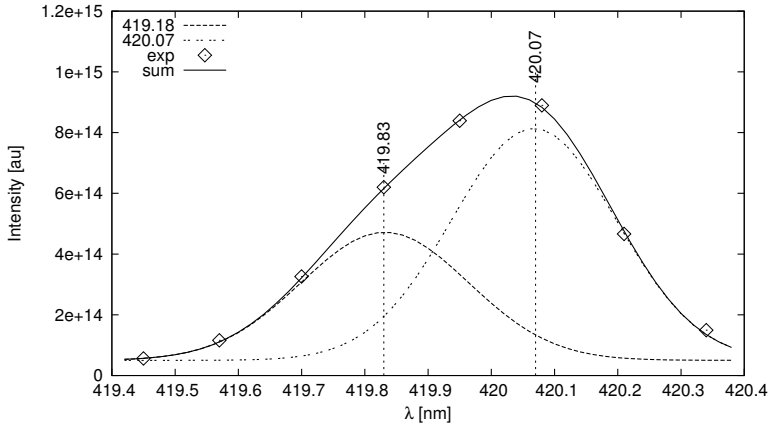

FIGURE 4.7: Fitting of two Gaussian profiles at 419.18 and 420.07 nm, to the experimental spectrum (test case 2).

4.3.2.2 Ar test matrix and results

Experimental source configuration, for Argon tests, is reported in Table[4.1]. Two mass flow rates were tested, corresponding to 0.20 and 0.17 mg/s. For each mass flow rate a power scan was performed in the range from 30 to 130 W of absorbed power by the plasma. Table[4.2] reports these parameters, together with the electron density obtained with the microwave interferometer, and the deposited power determined by current-voltage measurements.

TABLE 4.1: Plasma source configuration for Ar tests

Parameter	Description
Discharge chamber length	135 mm
Discharge chamber inner diameter	19 mm
Outlet diaphragm diameter	5 mm
Magnetic system	Two radially-polarized rings (diameters of 39 mm and 86 mm, respectively) composed of cubic (edge length of 20 mm) SmCo permanent magnets with radial magnetization

TABLE 4.2: Ar test matrix: mass flow rates, electron density by microwave interferometer, and deposited power by current-voltage measurements.

Test	Mass Flow Rate [mg/s]	P_W [W]	$\bar{n}_e$ [m^{-3}]
01	0.20	38	$9.0 \cdot 10^{+18}$
02	0.20	59	$8.0 \cdot 10^{+18}$
03	0.20	122	$1.6 \cdot 10^{+19}$
04	0.17	39	$6.0 \cdot 10^{+18}$
05	0.17	59	$9.3 \cdot 10^{+18}$
06	0.17	97	$1.5 \cdot 10^{+19}$

The ratio of metastable to ground population density, n_m/n_0, is evaluated, for each test, by means of the numerical model described in the previous section[3.1]. The electron temperature estimated by line ratio method is reported in Table[4.3] together with the n_m/n_0 parameter determined by numerical simulation.

The uncertainty of the numerical model, in section[3.1], in predicting the electron density, can be estimated, by comparison with the interferometric measurements, to be on the order of ±40%; it is actually ±10% if we exclude the exceptional high density measured in test 01.

If we assume this ±40% uncertainty, to be affecting the determination of all the output densities of the model, then the uncertainty on the metastable ratio n_m/n_0 is also ±40%. The total uncertainty on the estimation of the electron temperature, from line ratios, becomes then ±30%.

TABLE 4.3: Estimated electron temperature (line intensity ratio), and calculated (Ar model) ratio of metastable to ground population density.

Test	n_m/n_0	Electron Temperature [eV]
01	$4.1 \cdot 10^{-4}$	2.8
02	$4.2 \cdot 10^{-4}$	2.4
03	$4.4 \cdot 10^{-4}$	2.5
04	$4.6 \cdot 10^{-4}$	2.4
05	$4.7 \cdot 10^{-4}$	2.5
06	$4.8 \cdot 10^{-4}$	2.3

4.3.3 Experiments with CO_2 gas

4.3.3.1 CO_2 electron temperature estimation

Absolute and relative irradiance measurements have been performed with the HR4000 spectrometer. Several emission system are expected for a carbon dioxide plasma, as reported in Pearse's compilation[64], and in Ajello[65].

Following the observations made by Ajello, the UV-visible emission spectrum can be divided into three regions, namely:

1. The first region (126-195 nm) is characterized by the emission of the fourth positive system of CO($A^1\Pi - X^1\Sigma^+$); this system is often used for the determination of the vibrational temperature [66, 67] because of the small overlap of vibrational bandheads in this region.

2. The second region (195-250 nm) is characterized by the emission of the first negative system of $CO^+(B^2\Sigma^+ - X^2\Sigma^+)$, and the Cameron system $CO(a^3\Pi - X^1\Sigma^+)$.

3. The third region (250-450 nm), which is in the range of our spectrometer, is characterized by the emissions of the FDB (Fox, Duffendack and Barker[68]) system, and the doublet system. In this region, the presence of the $CO^+(A^2\Pi - X^2\Sigma)$ transition (Comet Tail system) is also reported by Pearse[64], though it is not observed by Ajello. The FDB and the doublet are the strongest emission features of our CO_2 discharge.

The $A - X$ (FDB) system is produced by electron impact excitation of the ground state and subsequent photon emission

$$\begin{aligned} e + CO_2(X^1\Sigma_g) &\rightarrow 2e + CO_2^+(A^2\Pi_u) \\ CO_2^+(A^2\Pi_u) &\rightarrow CO_2(X^2\Sigma_g) + h\nu_{v'v"} \end{aligned}$$

The $A-X$ system consists of strong transitions $(v', 0, 0) \rightarrow (v'', 0, 0)$, and weak $(v', 0, 0) \rightarrow (v'', 0, 2)$, transitions; additionally, this system is doubly degenerate in the component of the total angular momentum along the internuclear axis ($\Omega = 1/2, 3/2$), generating a total of four sub-systems.

The doublet $CO_2^+(B^2\Sigma_u - X^2\Sigma_g)$ system consists of two strong emission lines at 288.2 and 289.6 nm, respectively; it is produced in the same way as the $A - X$ system, and it is also doubly degenerate. The two lines of the $B - X$ system were clearly visible in every test, providing wavelength shifting calibration for the spectra acquisition.

Other emission features relative to the CO molecule have been detected, specifically: (i) the Angstrom system relative to the $CO(B^1\Pi - A^1\Pi)$ transition from 410 nm to 660 nm, (ii) the third positive system relative to the $CO(b^3\Sigma - a^3\Pi)$ transition from 265 nm to 380 nm, (iii) the triplet bands of the $CO(d^3\Delta - a^3\Pi)$ transition, from 410 nm to 650 nm. All these features indicate a certain degree of dissociation of the mixture. CO emission lines identification is based on the compilation reported in [69].

Figure[4.8] shows the spectra acquisition from 250 to 400 nm (no baseline correction), corresponding to the 2nd test case in table[4.5]; the figure features the CO_2^+ FDB and doublet, and the CO third positive systems. It can be noticed that the majority of lines in the UV region ($\lambda < 400$nm) pertains to the FDB system, and the strong emission of the doublet systems.

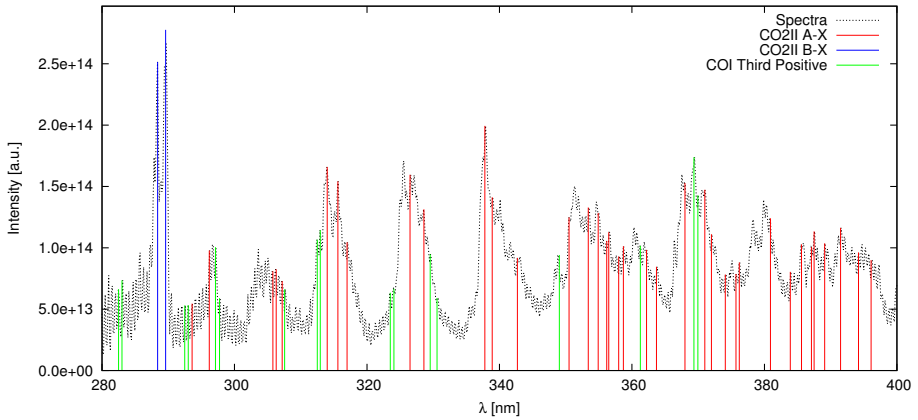

FIGURE 4.8: CO_2 discharge spectra in the 250-400 nm range (no baseline correction); spectra obtained for 72 W deposited power and 0.25 mg/s CO_2 mass flow rate, corresponding to the 2nd test case in table[4.5].

The electron temperature can be estimated by absolute irradiance measurements; for this purpose, it is necessary to correlate the irradiance to the plasma source dimensions and to the emitting volume observed by the fiber. The geometrical parameters needed are: the collection angle of the fiber, and the plasma column radius.

The electron temperature can be estimated by absolute irradiance measurements; for this purpose, it is necessary to correlate the irradiance to the emitting plasma volume observed by the fiber.The geometrical parameters needed are: the collection angle of the fiber, and the plasma column radius.

We have determined the fiber collection angle, conducting a light through the fiber and measuring the spot size generated on a paper sheet, whose normal was aligned with the axis of the fiber. Consider the schematic pictured in Figure [4.9]: the diameter of the plasma column is enclosed in the field of view of the fiber.

Consider now figure[4.10]: we have introduced an auxiliary cartesian coordinate system (x, y, z), so that the emission area, $S(L(y), R(y))$ of a plasma sheet, located at the plasma column vertical coordinate y from the axis of the discharge, is given by:

$$\begin{aligned} S(L(y), R(y)) &= 2\left(R(L^2 - R^2)^{1/2} + L^2 \tan^{-1}\left[\frac{R}{(L^2 - R^2)^{1/2}}\right]\right) \\ R(y) &= \left(R_0^2 - y^2\right)^{1/2} \\ L(y) &= \left(L_0 - y\ \tan(\theta_0)\right)^{1/2} \end{aligned} \tag{4.5}$$

where R_0 is the radius of the plasma column, L_0 is the radius of the collection cone measured at the axis of the discharge and θ_0 is the collection angle. $R(y)$ and $L(y)$ are

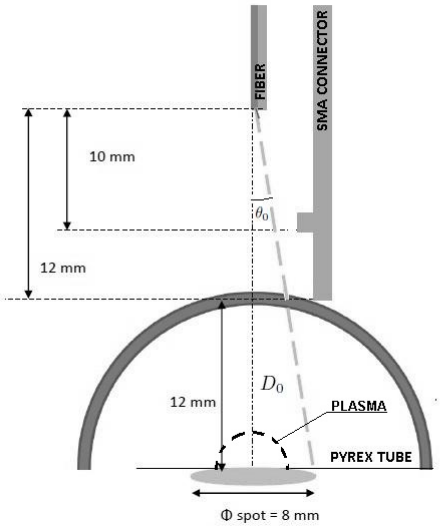

FIGURE 4.9: Schematic of the SMA connector over the pyrex tube; spot area generated by the fiber light.

the transversal and longitudinal dimension of the *local* plasma sheet at the y coordinate.

The (local) solid angle relative to an emitting plasma sheet is defined as the ratio of the local plasma sheet and the distance from the sheet to the fiber entrance:

$$\Omega(y) = \frac{S(y)}{(D_0 - y)^2} \tag{4.6}$$

with D_0 the distance between the fiber and the axis of the discharge (see Figure [4.9]).

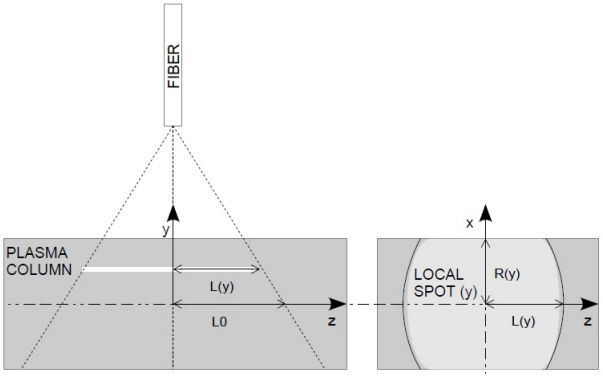

FIGURE 4.10: Geometrical model for the estimation of the emission plasma sheet area, function of the vertical coordinate y.

The measurement output of the spectrometer is the radiant flux per unit area, per unit wavelength, I_λ, with units [W/(m^2 nm)]; the wavelength specific radiance, L_λ, with

units [W/(m^2 nm sr)] is a local quantity defined on the emitting plasma sheet. The relation between these two quantities is:

$$I_\lambda = \frac{1}{2R_0} \int_{-R_0}^{+R_0} L_\lambda(y)\Omega(y)dy \tag{4.7}$$

By assuming isotropic emission and homogeneous plasma, L_λ results constant, and can be carried outside the integral:

$$L_\lambda = \frac{I_\lambda}{\frac{1}{2R_0}\int_{-R_0}^{+R_0}\Omega(y)dy} = \frac{I_\lambda}{\Omega_{avg}} \tag{4.8}$$

The radiance L is obtained integrating L_λ over the wavelength of interest:

$$L = \int_{\lambda_0-\delta\lambda}^{\lambda_0+\delta\lambda} L_\lambda d\lambda \tag{4.9}$$

$\delta\lambda$ is chosen as twice the variance of the Gaussian line profile, in order to enclose 95% of the energy radiated by the transition at λ_0; the variance of the profile is related to the FWHM by $FWHM = 2\sigma\sqrt{2\ln 2}$.

We are interested in the energy emitted by the two lines of the CO_2^+(B−X) system, at 288.2 and 289.6 nm. Little overlap from other emissions is expected in this range, and none particularly between the two lines; therefore we can carry the integration over the two peaks of the doublet as follows:

$$L_{BX} = \int_{\lambda_{288}-\delta\lambda_{288}}^{\lambda_{289}+\delta\lambda_{289}} L_\lambda d\lambda \tag{4.10}$$

The $\delta\lambda$ quantities are determined from the FWHM widths of the two lines, obtained by fitting the spectra with two overlapping Gaussian profiles, in the same manner as was done with Argon in section[4.3.2.1]. Assuming no absorption within the plasma, the average emission coefficient can be determined by [61]:

$$\bar{\varepsilon}_{BX} = \frac{L_{BX}}{s_2 - s_1} \tag{4.11}$$

where $(s_2 - s_1)$ is the depth of the plasma along the line of sight, corresponding in this case to the plasma column diameter.

The emission coefficient of a transition from a state p to a state q, at frequency ν_{pq}, is determined by the Einstein coefficient $A(p \to q)$ and the population of the upper state $n(p)$, as follows

$$\varepsilon(p \to q) = \frac{h\nu_{pq}}{4\pi} A(p \to q) n(p) \tag{4.12}$$

In the hypothesis of coronal equilibrium, the population of the upper state, $CO_2^+(B^2\Sigma_u)$, proceeds mainly from the CO_2 ground level by electron impact reactions; using optical emission excitation cross sections, the additional population, resulting from radiative cascade from upper levels, is also accounted in the coronal model. The emission coefficient, relative to the doublet CO_2^+(B−X) transitions, results:

$$\varepsilon_{BX} = n_0 \bar{n}_e K(\mathrm{T_e}) \frac{h}{4\pi} (\nu_{288} f_{288} + \nu_{289} f_{289}) \tag{4.13}$$

Where $K(\mathrm{T_e})$ is the optical emission rate constant of the CO_2^+(B−X) transitions, obtained by averaging the Tsurubuchi and Iwai's [70] optical emission cross section, over a Maxwellian electron distribution function; f_1 and f_2 are branching ratios, from Ajello[65], they represent the probability of the energy to be radiated by the 288 channel or the 289 channel. $\nu_1 = c/\lambda(288.2)$ and $\nu_2 = c/\lambda(289.6)$ are the transition frequencies.

The electron density, $\bar{n}_e$, is determined by interferometric measurements; n_0 is the CO_2 neutral density, it is estimated by means of the CO_2 global discharge model described in section[3.3]. Combining equations (4.11) and (4.13), the electron temperature can be determined; figure[] reports the optical emission rate constant of the CO_2^+(B−X) transitions.

$$K(\mathrm{T_e}) = \frac{L_{BX}}{s_2 - s_1} \frac{4\pi}{h n_0 \bar{n}_e (\nu_{288} f_{288} + \nu_{289} f_{289})} \tag{4.14}$$

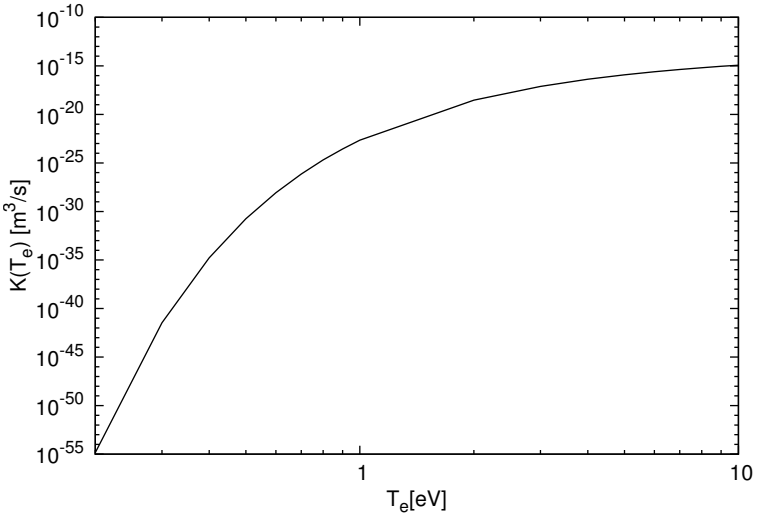

FIGURE 4.11: Optical emission rate constant of the CO_2^+(B−X) transitions.

4.3.3.2 CO2 test matrix and results

The source configuration, for CO_2 tests, is reported in table[4.1]; three mass flow rates were tested: (1) the maximum allowed by the controller that corresponds to 0.25 mg/s, (2) the minimum mass flow rate sustainable by the discharge, and (3) an intermediate mass flow rate. For each mass flow rate a power scan was performed in the range from 30 to 130 W of deposited power; the experimental test are listed in table[4.5], together with the electron density measured by microwave interferometry and the deposited power obtained from current voltage measurements.

TABLE 4.4: Plasma source configuration

Parameter	Description
Discharge chamber length	140 mm
Discharge chamber inner diameter	19 mm
Outlet diaphragm diameter	5 mm
Magnetic system	Two radially-polarized rings (diameters of 39 mm and 86 mm, respectively) composed of cubic (edge length of 20 mm) SmCo permanent magnets with radial magnetization

The electron temperature, estimated by absolute irradiance measurements is reported in table[4.6], together with the CO_2 neutral ground state density determined with numerical simulation with the CO_2 model. The temperature is approximately ~ 2 eV for all test

TABLE 4.5: CO_2 test matrix: mass flow rates, electron density by microwave interferometer, and deposited power by current-voltage measurements.

Test	Mass Flow Rate [mg/s]	P_W [W]	$\bar{n}_e$ [m^{-3}]
01	0.25	36	$1.20 \cdot 10^{+18}$
02	0.25	72	$2.50 \cdot 10^{+18}$
03	0.25	132	$3.80 \cdot 10^{+18}$
04	0.13	33	$7.98 \cdot 10^{+17}$
05	0.13	62	$1.37 \cdot 10^{+18}$
06	0.18	54	$2.38 \cdot 10^{+18}$
07	0.18	81	$3.38 \cdot 10^{+18}$
08	0.18	133	$4.28 \cdot 10^{+18}$

cases; this behaviour shows us that, at this level of ionization degree, the increase in power results almost entirely in an increase of plasma density.

TABLE 4.6: Estimated electron temperature (absolute irradiance), and calculated (CO_2 model) ground state neutral density.

Test	n_0 m^{-3}	Electron Temperature [eV]
01	$4.85 \cdot 10^{+020}$	2.1
02	$3.82 \cdot 10^{+020}$	2.0
03	$2.32 \cdot 10^{+020}$	2.0
04	$1.73 \cdot 10^{+020}$	2.4
05	$8.96 \cdot 10^{+019}$	2.5
06	$2.54 \cdot 10^{+020}$	2.0
07	$1.74 \cdot 10^{+020}$	2.0
08	$8.90 \cdot 10^{+019}$	2.1

Chapter 5

N2O Plasma Assisted Decomposition

Monopropellant thrusters are widely used in spacecraft attitude control and station keeping for satellites. Hydrazine and hydrogen peroxide are among the most used in such propulsion systems and are a proven technology. However, in recent years, research has committed into finding a *green* alternative to these propellants, because their toxicity and inherent flammability make them difficult and costly to handle[12, 13].

Nitrous oxide offers many inherent advantages as small satellite's propellant. It is non-toxic, non-corrosive and may be used with common structural materials. Nitrous oxide is stable and comparatively non-reactive at ordinary temperatures, is classified as a non-flammable and is shipped with the required "Green Label". From a space-propulsive point of view, N_2O offers the following advantages:

1. It can be stored as a liquid ($\sim$745 kg/m^3) with a vapour pressure of $\sim$52 bar (at 20 °C), and a storage temperature range from -34 to 60 °C.
2. Safe handling, non toxic and non flammable at ambient pressure and temperature.
3. Decomposes exothermically with standard enthalpy of formation of 82.05 kJ/mol.

Compare to hydrogen peroxide, N_2O presents a higher specific impulse; compared to hydrazine, N_2O does not presents safety concerns (and expensive handling); compared to both monopropellants, N_2O presents an extended storage temperature range and the "self pressurization" capability, which make possible to store it in liquid form and spill it in gaseous form. A good analysis of the advantages of the application of N_2O for space propulsion is provide by Zachirov in [13].

N_2O resistojets have been developed by SSTL (Surrey Satellite Technology LTD) [71]; these devices produce 125-270 mN thrust and 127-182 s specific impulse, they operate in the range of 0.1 g/s mass flow and 100-600 W electrical power, with efficiencies spanning from 27 - 30 %. Prior to operation the resistojet is heated, typically for 15 minutes, to achieve a minimum temperature throughout the chamber.

Catalytic decomposition of N_2O have been studied for monopropellant propulsive applications [13, 72]; Zakirov[72] reports chamber temperatures in the range 700-800 C°. Although this method does not need electrical power, catalyst is prompt to deteriorate when subject to high temperatures.

Plasma discharges have been proposed as method to initiate and sustain N_2O decomposition; a numerical investigation of N_2O plasma ignition is reported in [11], and a DBD N_2O discharge thruster experiment is presented in [14], which, however, does not shows promising results.

The catalytic effect of the plasma is well known [18, 25]; it is used for efficient CO_2 dissociation, fuel conversion and also in N_2O dissociation for nitric oxide production[73].

It has been, experimentally and numerically, observed[48, 49] that, for efficient molecular dissociation, *warm* plasmas, achieved with gliding arc or microwave heated discharges, provide good results, compared to *cold plasmas* (i.e. DBD, corona).

Possible advantages of plasma technology applied to monopropellant propulsion are, beside the catalytic effect, the capacity to exceed the ideal specific impulse limit of chemical thrusters, thanks to the additional electrical energy deposited into the gas; another advantage is related to the speed of plasma, the ability to reach operating conditions in very short times, and the possibility to exert an electrical control of the discharge and the propulsive parameters, to a certain degree to be addressed yet.

In this chapter we present preliminary results of a gliding arc experiment, for N_2O plasma assisted decomposition, carried out at Drexel University (Philadelphia); the experiment is designed to prove the feasibility of a N_2O gliding arc monopropellant thruster. The discharge is characterized by means of optical emission spectroscopy (OES), Fourier transform infrared spectroscopy (FTIR), thermocouple measurements and current-voltage measurements. The catalytic effect of the plasma is proved by the high vibrational temperature, T_v, of the plasma, and the degree of decomposition of the products of the discharge.

In the second part of the chapter, we present a numerical global model developed to investigate the advantages of plasma assisted decomposition; the purpose of the model is to demonstrate, from a numerical point of view, that the catalytic action of the plasma,

can be successfully applied to promote decomposition and combustion of nitrous oxide for monopropellant propulsion. The model make uses of modified non-equilibrium reaction rates, that depends on the neutral gas temperature and on the molecular vibrational temperature; a vibrational energy equation is implemented to track the change of the vibrational temperature during the discharge.

5.1 Gliding arc discharge

A gliding arc (GDA) discharge is obtained by a fast translating or rotating electrical arc; the arc is generated by a high voltage in a short gap, and then is pushed away by the flowing gas itself. As the arc travels downstream, it elongates because of the increasing size of the gap, until it reaches a critical length when the heat losses, from the plasma column, begin to exceed the energy supplied by the source; at that point the arc extinguishes , but it reignites itself at the minimum distance between the electrodes to start a new cycle[18].

The gliding arc plasma can be either thermal or non-thermal depending on the power and flow rate. It is possible to operate the arc also in a transitional regime when the arc starts thermal, but during its evolution, energy balance requirements shift the plasma in a non thermal, and less expensive, regime.

The non-equilibrium condition of the plasma is realized when $T < T_v < T_e$, with T_v the vibrational temperature of the molecules. In this condition, chemical reaction rates can be stimulated in regimes quite different from conventional combustion and environmental situations. GDA experiments have been carried to demonstrate efficient dissociation of green house gases as CO_2 and N_2O[73, 74].

In a N_2O gas GDA discharge, two mechanism are able to promote dissociation and combustion:

1. Hot spot localized dissociation, promoted by high energetic electrons within the arc, results in the following reactions:

$$\begin{aligned} N_2O + e &\rightarrow N_2 + O(_1D) + e \quad \Delta H = -0.3\,eV \\ N_2O + e &\rightarrow N_2 + O(_3P) + e \quad \Delta H = -2.3\,eV \\ N_2O + e &\rightarrow NO + N + e \qquad \Delta H = -1.0\,eV \end{aligned} \tag{5.1}$$

with the proper convention of $\Delta H < 0$ for exothermic processes; fast recombination of radicals results in additional heating of the gas:

$$\begin{aligned}
&N_2O + O(_1D) \rightarrow N_2 + O_2 && \Delta H = -5.4\,eV \\
&N_2O + O(_1D) \rightarrow NO + NO && \Delta H = -3.5\,eV \\
&N_2O + O(_3P) \rightarrow N_2 + O_2 && \Delta H = -3.4\,eV \\
&N_2O + O(_3P) \rightarrow NO + NO && \Delta H = -1.6\,eV \\
&NO + NO \rightarrow N_2 + O_2 && \Delta H = -1.0\,eV
\end{aligned} \tag{5.2}$$

2. High vibrational temperature, $T_v > T$,decrease the activation energy for unimolecular dissociation of the gas, resulting in a non equilibrium factor $\Phi(T, T_v)$ that boost the thermal dissociation reaction rate as follows:

$$N_2O + M \rightarrow N_2 + O + M \quad K(T, T_v) = \Phi(T, T_v) \cdot K(T) \tag{5.3}$$

An example of $\Phi(T, T_v)$ is reported in figure[5.1]. Vibrational energy is pumped into the molecule by plasma electron collisions, reducing the activation energy as explained in figure[5.2].

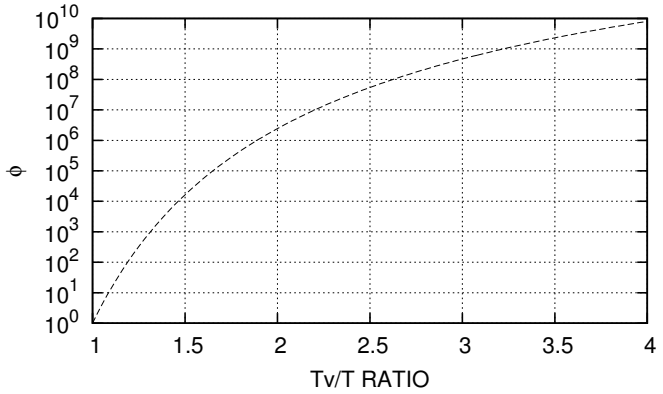

FIGURE 5.1: Non equilibrium factor $\Phi(T, T_v)$ calculated with Kuznetsov's formula[1], for N_2O at $T = 500$ K.

A rotating gliding arc reactor was designed to investigate the applicability, of this type of discharge, to monopropellant propulsion. The work has been carried out at Drexel University under the supervision of professor Danil Dobrynin and professor Gary Nirenberg. The design has been conducted with reference to the operative parameters of the N_2O resistojet previously mentioned. Electrical power range $P_W < 50$ W, mass flow rate 10-30 mg/s, compact dimensions 1.6 cm $\times$ 10 cm.

A schematic of the reactor is reported in figure[5.3]; the gas is injected through an inner steel tube that serves also as high voltage electrode; it is then expelled tangentially in a

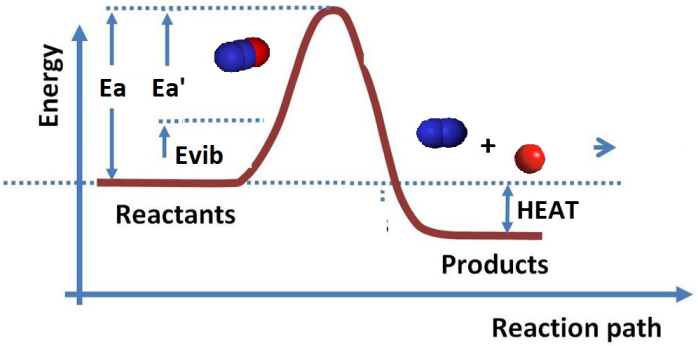

FIGURE 5.2: Qualitative explanation of the catalytic effect of higher vibrational temperatures $T_v > T$.

cylindrical chamber at a velocity of 38 - 95 m/s depending on the flow rate. The electrical arc is ignited between the inner high voltage electrode and the grounded external wall, and starts rotating pushed by the gas flow. A picture of the ignited N2O discharge is reported in figure[5.4].

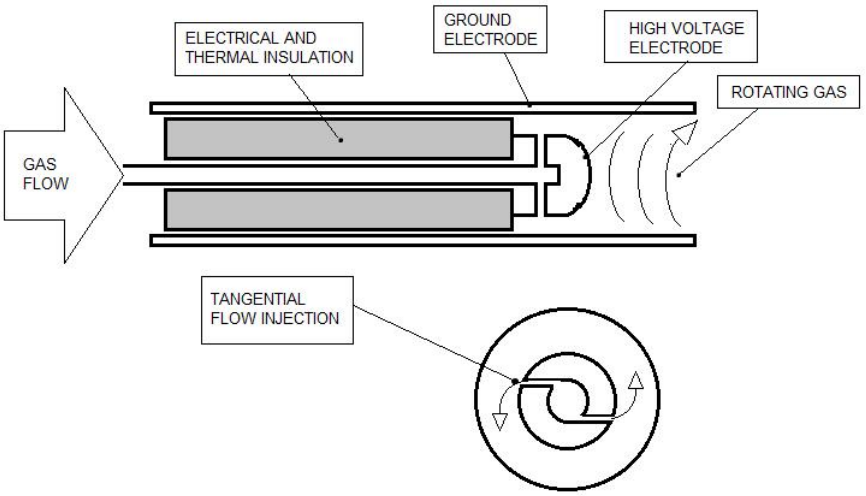

FIGURE 5.3: Schematic of the gliding arc reactor.

FIGURE 5.4: N_2O gliding arc reactor in operation.

The high voltage is provided by a simple custom made power unit, composed by a ballast resistor and a flyback transformer connected in series; the ballast resistor has the purpose to limit the amount of current flowing in the circuit, while the flyback transformer provides high rectified voltage.

5.1.1 Experimental tests

The experiments are conducted in atmospheric conditions; mass flow rates have been measured with a variable area flow meter, starting from the the minimum sustainable by the discharge; inlet gas pressure have been measured with a pressure gauge.

Table[5.1] reports the tested flow rates in units of millimetres (the unit scale of the flow meter), the corresponding volumetric and mass flow rates for N_2O in the experimental conditions, together with the inlet pressure condition; pressure and gas conversion factors have been determined as reported in [75].

TABLE 5.1: Gliding arc N_2O tests: volume flow rates at STP (standard 1 atm, 0°C) conditions, mass flow rates and inlet pressures.

Test	Flow scale [mm]	Volume Flow Rate(STP) [L/min]	Mass Flow Rate [mg/s]	Inlet Pressure [PSIG]
01	15	0.49	14.6	0.2
02	20	0.66	20.0	0.9
03	22.5	0.75	22.5	1.0
04	25	0.84	25.1	1.2
05	30	1.02	30.5	1.6
06	35	1.20	36.0	2.0

Power deposited into the discharge have been determined by current and voltage probe measurements. An example of current voltage acquisition is reported in figure[5.5]; the voltage and currents profile are periodic with a frequency of 29.5 kHz. Table[5.2] reports the average values of voltage, current and power for each test.

TABLE 5.2: Gliding arc N_2O tests: average voltages, currents and discharge power.

Test	Average Voltage [V]	Average Current [mA]	Average Power [W]
01	485	24.1	13.4
02	687	24.4	21.2
03	912	23.1	29.4
04	868	24.3	28.0
05	956	23.5	30.6
06	1047	23.6	33.2

The discharge shows three regimes described in figure[5.6]; at flow rates less than 22.5 mm, the arc is stable rotating between the downside wall of the high voltage inner electrode, and the wall of the outer ground electrode; as the flow rate increase, the point of attachment of the arc, in the inner electrodes, moves toward the tip of the electrode, laying in the center at 22.5 mm of flow rate; with higher flow rates, the arc shifts the attachment spot, on the electrodes, in an apparent random motion.

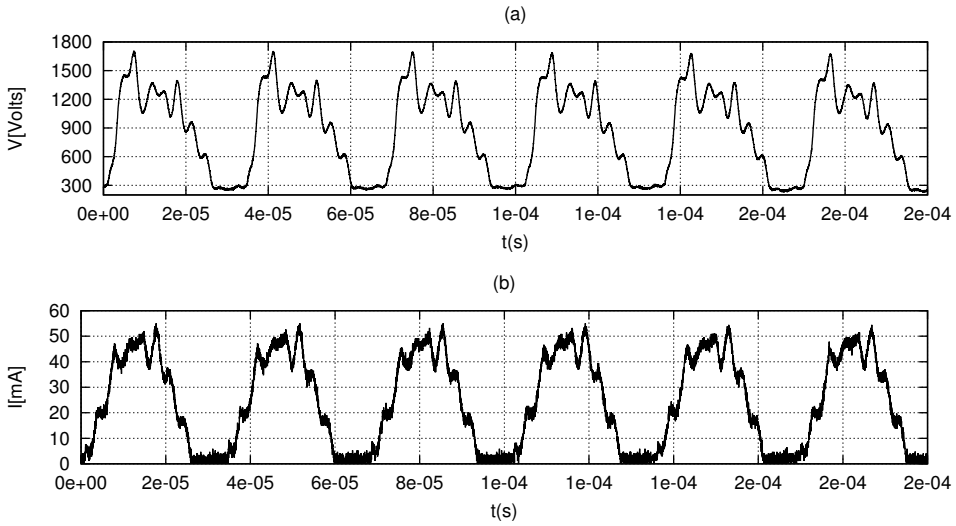

FIGURE 5.5: Measured voltage and current for test case 04 .

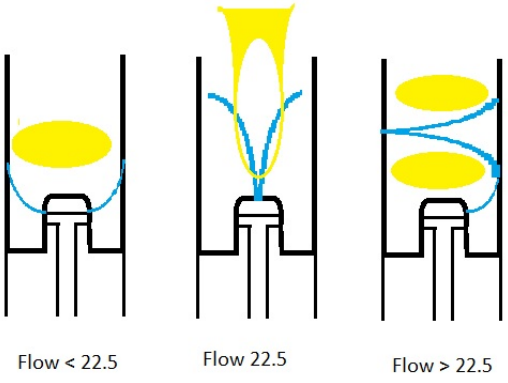

FIGURE 5.6: Gliding arc flow discharge regimes.

In the 22.5 mm flow regime, when the arc spot lies fixed on the tip of the electrode, the flame is pushed outside the the discharge volume, as depicted by the central image in figure[5.4]; in this condition, thermocouple measurements of the flame temperature, can be made submerging the tip of the probe into the flame, without interference from the electrodes; on the other regimes, temperature measurement are difficult, because of the tendency of the electrical arc to discharge on the probe tip. A flame temperature of 1200 ° C has been recorded for test case 03, corresponding to 22.5 mm flow regime.

Optical emission spectroscopy, in the UV-VIS range, is carried out for the 22.5 mm test case in order to estimate the vibrational temperature of the discharge; the spectrum was obtained using a fibreoptic bundle (Princeton Instruments-Acton, 10 fibres-200 μm core) connected to the spectrometer (Princeton Instruments-Acton Research, TriVista

TR555 spectrometer system with PIMAX digital ICCD camera); the spectrometer is operated at 0.013 nm resolution, wavelength shift calibration is performed using an Hg(Ar) spectral calibration lamp (Oriel 6035 - Newport).

Fourier transform infrared spectroscopy is performed on the gas products, for each test, in order to estimate the degree of decomposition of N2O after the discharge. The infrared spectrum was collected with a Nicolet 6700 IR spectrometer (from Thermo Electron Corporation), working with a ZnSe beam splitter able to collect the IR spectra from 650 to 6000 cm^{-1}.

5.1.2 N2O vibrational temperature estimation

The spectrum of the 22.5 mm test case discharge, in the range 300 - 385 nm, is shown in figure[5.7]. In this wavelength region the spectra is characterized by strong emission of the nitrogen second positive system, corresponding to the $N_2(C^3\Pi_u(v')-B^3\Pi_g(v''))$ transitions.

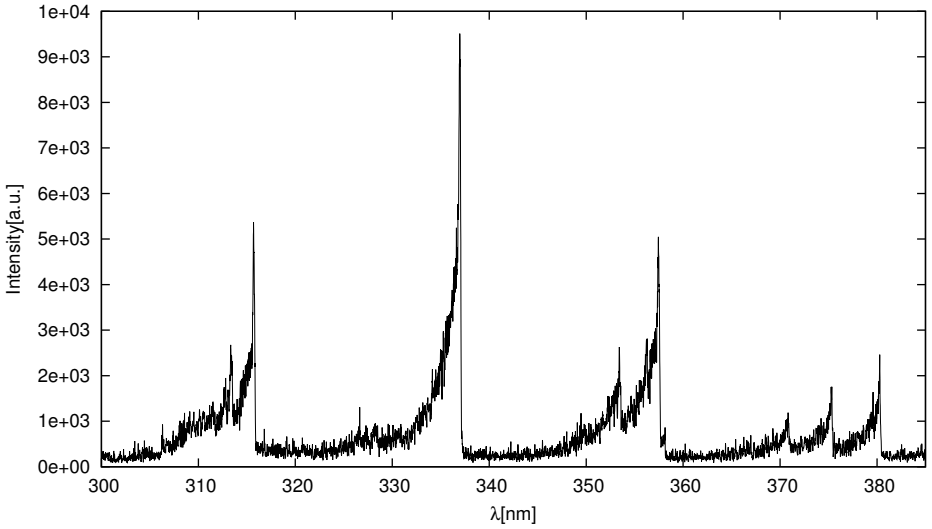

FIGURE 5.7: N_2 2nd positive emission system in the spectrum of test case 03.

The spectra has been analysed with SPECAIR, a commercial software for computing, manipulating and fitting spectra. this software allows the simulation of synthetic spectra from a database of Einstein emission, absorption and stimulated emission coefficients; additional features, as H_2O and CO_2 atmospheric absorption, can be also included.

In the general case, the spectrum is generated specifying emitting species concentration,s within the plasma, electron temperature T_e, translational T, rotational T_r and vibrational T_v temperatures of the plasma; the relative heights of the peaks, is constructed in the hypothesis of Boltzmann distribution of the electronic states, vibrational states, rotational and translational states.

In our case we have one very strong emitting system, we can neglect the other species and normalize the spectrum, so that the electron temperature is not a variable of the system any more. The relative heights of the emission peaks, of a single molecular electronic state, becomes only a function of T_v, T_r, T. However, T is known from the probe measurement, and is set to 1500 K; T_r can be assumed equal, or very close, to T by virtue of fast VT energy exchange that tends to thermalize both temperatures.

The spectrum in figure[5.7] was fitted with a synthetic spectra, generated by varying the value of T_v, until a low value of the root mean square error is obtained.

Instrumental broadening is taken into account by the software, by using a slit function that can be either triangular, trapezoidal or provided by the user. We use the isolated line profile, provided by the calibration lamp, at 546.07 nm, normalized so that the peak height is unitary.

Figure[5.8] shows the fitted spectrum; synthetic spectra is reported in red line. the regions between 300-320 and 360-380 nm appear to fit not so well, probably due to superposition of other weak emission systems or to excessive noise; however, it has to be point out that gliding arc discharge are highly non homogeneous and transient plasmas, therefore a clear spectrum is not expected. The spectrum fitting indicates that the vibrational temperature is around 5000 K, suggesting the plasma is in a non-equilibrium condition favourable to dissociation. An analysis of the uncertainty on the T_v estimation has not been performed in this case, however indication of how to proceed for such analysis, with SPECAIR, is reported in[76].

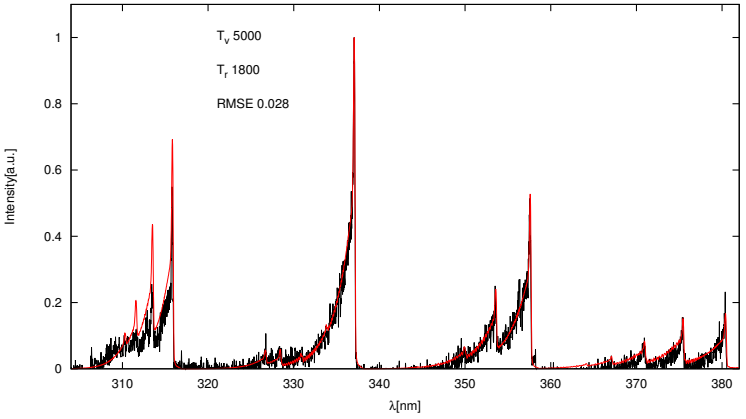

FIGURE 5.8: Fitting of the spectrum: synthetic spectra (red line) and experimental spectra (black line).

5.1.3 N2O decomposition estimation

Fourier transform infrared spectroscopy is a technique which is used to obtain an infrared spectrum of absorption of a gas, liquid or solid. IR radiation is passed through a sample, some of the infrared radiation is absorbed by the sample and some of it is passed through. The resulting spectrum provides informations on the composition of the sample, and in the case of gases, the integrated area of the absorption lines is proportional to the density of the molecular species.

Absorbance measurements have been performed with the NICOLET 6700 FTIR spectrometer, in the energy range from 2400 - 4000 cm^{-1}. Figure[5.9] shows the acquired spectrum of pure N_2O; the figure shows that some portions of the spectrum are affected by saturation, other portions are affected by baseline drift. The useful portion of the spectrum is located between 3300 and 3400 cm^{-1}: it has absorbance < 1, which is recommended for quantitative measurements, and it does not superimpose with the IR spectrum of other dissociated products as nitric oxide (NO), nitrogen dioxide (NO_2), N_2 and O_2.

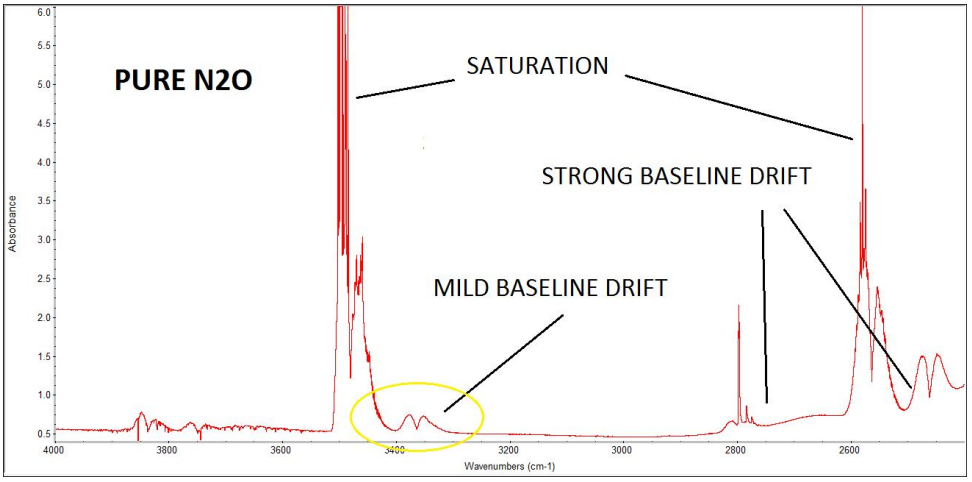

FIGURE 5.9: Absorbance of pure N_2O sample.

When performing FTIR measurements, figure[5.10], the gas is exhausted into a chamber with a metal pipe connected to the gas cell to be operated by the spectrometer. The amount of decomposition can be estimated as $1 - S/S_0$, with S_0 the integrated area, between 3300 and 3400 cm^{-1}, of the pure gas, and S the integrated area of the discharged gas. Discharge dissociation values are plotted in figure[5.11].

Absolute concentration of N_2O can be determined form the experimental IR spectra, by calculation of the absorption coefficient of N_2O, in the 3300 - 3400 cm^{-1} range, with the HITRAN[77] database and the procedure indicated in [77]; by comparison of the calculated quantity with the density of the pure N_2O loaded gas cell, at atmospheric

pressure and room temperature, we can estimate the accuracy of the decomposition measurements to be about 40%.

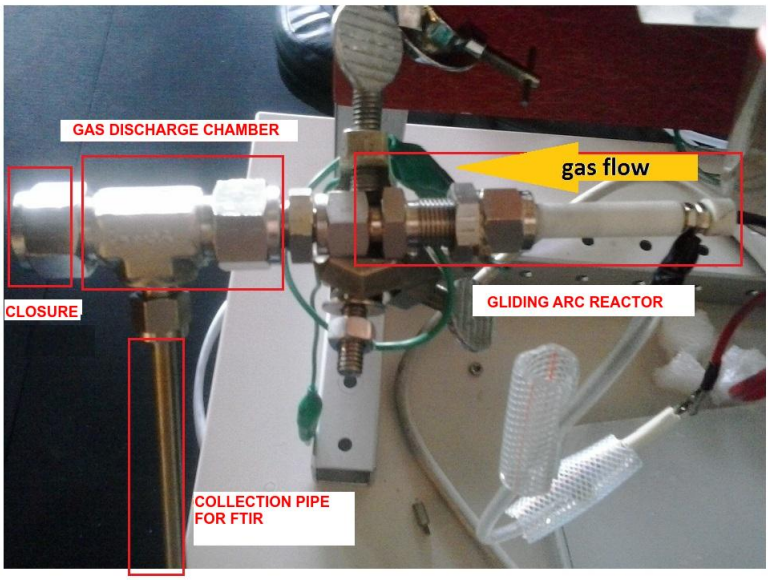

FIGURE 5.10: Experiment configuration for gas products samples collection.

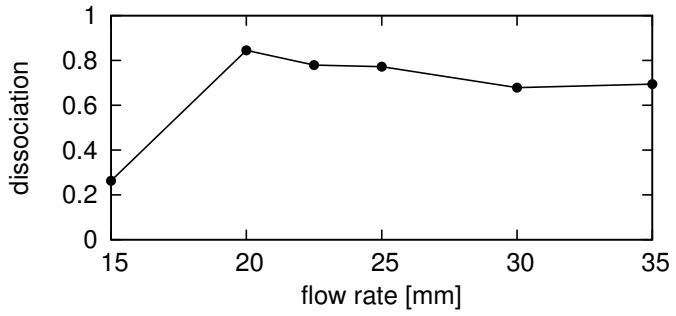

FIGURE 5.11: N_2O dissociation versus flow rate.

5.1.4 Discussion

We have presented results of an experiment on nitrous oxide gliding arc decomposition for monopropellant propulsion applications. The results can be summarized as follow:

1. 15-35 mg/s flow rate with 15-35 W discharge power.
2. 1500 K translational gas temperature.
3. ~5000 K vibrational temperature, favourable to promote dissociation.
4. 30-80 % decomposition of the gas in the discharge.

We want to compare the results of this experiment to an ideal thermal resistojet working in the same configuration (flow rate, injected power, chamber volume). In order to do so, we arrange a thermal batch reactor model that simulate the decomposition of a N_2O gas flow by injecting thermal power directly into the gas neutral energy equation. The model uses the subroutines provided by the package Cantera [78], including the kinetic scheme of thermal reaction rates; it solves a continuity equation for each specie (N_2O, N_2, O_2, NO, N, O), plus a neutral energy equation:

$$\frac{\mathrm{d}}{\mathrm{d}t}\left(\sum n_i u_i\right) = \dot{m}_{in} h_{in} - \sum \Gamma^i_{exh} h_i - \Delta H_0 + P_W - P_{loss} \tag{5.4}$$

where P_W is the thermal input power, and P_{loss} are wall conductive and convective heat losses (radiative losses are neglected for simplicity). The model has the same volumetric chamber, and lateral walls, of the GDA reactor, and it exhaust in atmospheric conditions. Table[5.3] reposts the numerical values of the simulations corresponding to the six experimental test cases; the table shows that the decomposition degree, that is achieved by thermally heating the gas, is very low, ans so it is the steady state chamber temperature $T \sim 580 - 720$ K.

We can see, therefore, that given the same amount of power, the plasma is much more effective at raising the temperature of the gas, by catalytic stimulation of the dissociation and making available the chemical energy of the gas.

TABLE 5.3: Thermal simulations of the six experimental gliding arc test cases.

Test	Mass Flow [ms/s]	Power [W]	Temperature [K]	Dissociation
01	14.6	13.4	645	9.5e-6
02	20.0	21.2	736	9.1e-6
03	22.5	29.4	829	9.0e-6
04	25.1	28.0	794	8.9e-6
05	30.5	30.6	791	8.6e-6
06	36.0	33.2	788	9.6e-6

The measured temperature of 1500 K, and the 0.78 dissociation degree, of the 22.5 mm test case reported in the previous section, allow us to project the thruster performances, that such a reactor could produce, if operated in vacuum conditions and equipped with a nozzle.

With reference to figure[5.12], imagine to close the the thruster chamber with a nozzle composed by ceramic materials (alumina or nitride ceramics), as the one used in plasma

welding technologies. The throat section is chosen with a diameter of 0.5 mm for two reasons:

1. A 0.5 mm diameter is close to the value of 0.4 mm adopted by the resistojet in[71].
2. The chamber pressure of the reactor operated in vacuum, with a 0.5 mm throat diameter, results the same pressure of the reactor, operated in the atmospheric experimental conditions previously reported.

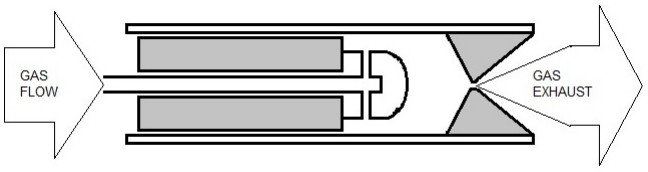

FIGURE 5.12: Schematic of the gliding arc reactor with ceramic nozzle.

Therefore we can assume the measured temperature and decomposition to be produced as well with the thruster exhausting in vacuum. The fraction of the gas that has undergo decomposition (i.e. 0.78) is assumed to be, for sake of simplicity, $N_2 + 1/2O_2$. Knowing chamber gas composition, pressure and temperature, thrust and specific impulse can be calculated with formulas(2.23,2.29,2.30), without the charged particles contribution; the efficiency, instead, is calculated as follow:

$$\eta_P = \frac{I_{SP} F g_0}{2(P_W + \dot{m}_{in} H_{N_2O})} \tag{5.5}$$

With H_{N_2O} the enthalpy of formation of the N_2O molecule. We obtain a thrust value of 37 mN, a specific impulse of 170 s and efficiency 43%; these values compare well with the 125 mN thrust, 127 s I_{SP}, 100 W electrical power and 27% efficiency of the SSTL N_2O resistojet.

5.2 N2O plasma assisted decomposition model

In this section we present a numerical global model developed to investigate the advantages of plasma assisted decomposition; the purpose of the model is to demonstrate, from a numerical point of view, that the catalytic action of the plasma, can be successfully applied to promote decomposition and combustion of nitrous oxide for monopropellant propulsion.

Given the highly non homogeneous feature of the gliding arc discharge, the model cannot be applied to describe such discharges; however, the model can be applied to the study of microwave discharges, that are able to produce diffusive homogeneous plasma; indeed, global models have been used extensively to study the chemistry and discharge features of microwave plasmas, at low, moderate and high pressures, few examples are [79–81].

Scott *et al.*[82] presented a three-temperature global model to study the thermo-chemistry of an hydrogen microwave plasma; in their work the authors assumed an electron temperature for electrons, vibrational states, roto-translational states, each characterized by its Boltzmann distributions at temperature $\mathrm{T_e}$, T_v, T.

Microwave discharge have also been applied to the decomposition of N_2O by several authors [83–85], the main purpose, in these papers, is destruction of the molecule for green house mitigation.

The model described in this section, is developed keeping in mind a possible application with microwave discharges; the model shares many aspects of the model described in chapter[2], and presents some additional features:

1. The geometry is a cylindrical reactor with an injection aperture (of negligible area) and an exhaust section at the diaphragm interface; the input parameters of the model are the chamber dimensions radius R and length L, the ϱ^* exhaust-to-chamber section ratio, the mass flow $\dot{m}$, and the deposited power P_W; no magnetic field is employed in these simulations.

2. Species are considered to exhaust in vacuum conditions, simulating thruster operations. Neutral particles exhaust is calculated with the isentropic nozzle formula(2.23); charged particles are assumed to exhaust at Bohm conditions (i.e. extraction coefficient and acceleration coefficient unitary: $\beta\,, \alpha = 1$).

3. Neutral particles wall diffusion and recombination, is described by the formulas presented in section[2.2.3]; charged particles wall diffusion is described by the non-magnetized formulas presented at the beginning of section[2.2.1].

4. Conductive and convective heat losses have been considered in the same manner as was done in equation(5.4).

The model make use of a 3-temperature description: T_e, T_v, T; a common vibrational temperature is assumed for the asymmetric N_2O(v=2224 cm^{-1}) mode and the N_2(v=2330 cm^{-1}), O_2(v=1556 cm^{-1}) and NO(v=1875 cm^{-1}) vibrational modes; the two symmetric modes N_2O(v=589, 1285 cm^{-1}), are assumed to be characterized by an equal temperature due to close Fermi resonance, this approach has been adopted for CO_2 and for N_2O in [18, 86]; however, because of the fast VT relaxation, in the pressure range of interest, of the bending mode (v=589 cm^{-1}), the vibrational distribution of the two symmetric modes is assumed to be thermalized at the gas temperature T.

Boltzmann distribution is assumed for electrons, vibrational molecular states and vibro-roto-translational states, characterized by relative temperatures. The species densities are determined solving the time dependent continuity equations(2.2); the temperatures are determined solving three energy equations that will be explained in section[5.2.2].

5.2.1 kinetic scheme and non equilibrium reaction rates

The considered species are listed in table[5.4]; the implemented reactions are listed in the kinetic scheme table[A.10] in appendix.

Electron-neutral vibrational excitation provides the channel for the generation of a non-equilibrium population of the vibrational states of the gas. This non equilibrium condition affects the chemistry of the discharge, enhancing, or inhibiting, certain reactions; the subject have been studied mostly by Russian researchers from 1970 to 1990; main results and references, on the subject, can be found in few books [1, 18, 25].

TABLE 5.4: Species considered for the N_2Oplasma assisted decomposition model

GAS	SPECIES						
N_2O	N_2O	N_2	O_2	NO	N	O	$O(_1D)$
	O_2^-	O^-	NO^-				
	N_2O^+	N_2^+	O_2^+	NO^+	N^+	O^+	

Neutral gas phase reactions are usually expressed by the modified Arrhenius equation: $K(T) = AT^n \exp(-E_a/T)$; however, when the gas is in a non-equilibrium condition, the neutral gas phase reaction rate, becomes a function of the vibrational temperature too, $K(T, T_v)$, and can be expressed as the product of the thermal reaction rate times a non equilibrium factor $\Phi(T, T_v)$:

$$K(T, T_v) = \Phi(T, T_v) \cdot K(T) \tag{5.6}$$

The processes that are affected by the non equilibrium, and relevant to this model, are:

1. Molecular dissociation $XY + M \rightarrow X + Y + M$.
2. Bimolecular reaction $XY + Z \rightarrow X + YZ$.

Recombination of particles, instead, is considered driven only by the translational temperature [18]. In order to estimate the non equilibrium factor for the two above mentioned processes, we refer to the *Kuznetsov model* for decomposition of polyatomic and diatomic molecules, , and the *Model of the efficiency of vibrational energy utilization (α model)*; both models are reported in [1], and in appendix[B].

The Kuznetsov model applies to the dissociation reactions, reported in table[A.10], of the type:

$$N_2O + M \rightarrow N_2 + O + M$$

$$N_2 + M \rightarrow N + N + M$$

$$O_2 + M \rightarrow O + O + M$$

$$NO + M \rightarrow N + O + M$$

where M can be any third body.

The α-model is applied to the reactions reported in table[5.5]; the values of the efficiency α are taken from literature, or estimated following the recommendations in [1, 18]; activation energies E_a, and α efficiencies are reported in table[5.5] as well.

5.2.2 Energy Equations

Three energy equations are implemented in this model, respectively for electrons, molecular vibrational energy and total neutral gas energy. The electron energy equation is the same equation(2.1) presented in the chapter[2]; the electron distribution function is assumed to be Maxwellian for sake of simplicity.

TABLE 5.5: Activation energies E_a, and α efficiencies.

Reaction	E_a [K]	α
$NO + N \rightarrow O + N_2$	610	0.20 [b]
$O + N_2 \rightarrow N + NO$	38370	0.51 [a]
$NO + O \rightarrow N + O_2$	19500	0.94 [a]
$N + O_2 \rightarrow O + NO$	3150	0.24 [a]
$N_2O + O \rightarrow N_2 + O_2$	8020	0.30 [b]
$N_2 + O_2 \rightarrow O + N_2O$	47876	0.90 [b]
$N_2O + O \rightarrow NO + NO$	13930	0.30 [b]
$NO + NO \rightarrow O + N_2O$	32056	0.90 [b]
$NO + NO \rightarrow N_2 + O_2$	33660	0.20 [b]
$N_2 + O_2 \rightarrow NO + NO$	55389	0.70 [b]

1. (a) Values from [1, 18], (b) estimated

The vibrational energy equation describes the rate of change of the the vibrational energy stored in the molecules within the discharge; the equation is derived in the frame of the harmonic approximation[25, 87], the vibrational states are assumed to be in Boltzmann equilibrium at temperature T_v; the equation is

$$\frac{\mathrm{d}}{\mathrm{dt}}\left(\sum n_i e_{vi}\right) = \dot{m}_{in} e_{v,in} - \sum \Gamma^i_{exh} e_{vi} - E^{rel}_{VT} + S_{ev} \tag{5.7}$$

The first two terms on the RHS, are the flow of vibrational energy at the boundaries; the third term, E^{rel}_{VT}, is the V-T relaxation of vibrational energy, the last term is the electron-vibrational excitation of vibrational energy.

$$E^{rel}_{VT} = \sum -\frac{n_i(e_{vi} - e^0_{vi})}{\tau_{i_{VT}}} \tag{5.8}$$

e_{vi} and e^0_{vi} are respectively, the vibrational energy stored in the i-th species within the i-th mode, and the equilibrium vibrational energy of the same; they are:

$$e_{vi} = \frac{\mathrm{h}\nu_i}{\exp\left(\frac{\mathrm{h}\nu_i}{k_b T_v}\right) - 1}, \quad e^0_{vi} = \frac{\mathrm{h}\nu_i}{\exp\left(\frac{\mathrm{h}\nu_i}{k_b T}\right) - 1} \tag{5.9}$$

In our case each molecule has one mode (two of the three modes of N_2O are thermalized); in the more general case, the expression for polyatomic vibrational energy should be used. The relaxation time $\tau_{i_{VT}}$ is expressed by the Landau-Teller formula:

$$[\tau_{i_{VT}}]^{-1} = k_i^{10}\, n_0 \left[1 - \exp\left(-\frac{\mathrm{h}\nu_i}{k_b T}\right)\right] \tag{5.10}$$

With n_0 the total gas density and k_i^{10} the relaxation rate constant of the i-th mode; expressions for k_i^{10} can be found in [18, 25].

The S_{ev} term is given by the summation of all the vibrational excitation processes that input energy into the considered modes (i.e. the diatomic and the asymmetric N_2O modes).

$$S_{ev} = n_e \sum_i n_i \sum_j K_{ev}^{ij}(\mathrm{T_e})\varepsilon_{th}^{ij} \tag{5.11}$$

Finally the rate of change of the total energy, of neutrals and ions, is described by the following equation:

$$\frac{\mathrm{d}}{\mathrm{d}t}\left(\sum n_i u_i\right) = \dot{m}_{in} h_{in} - \sum \Gamma_{exh}^i h_i - \Delta H_0 + \sum(\varepsilon_j - \delta h_{0j}) + S_{ev}^{tot} \tag{5.12}$$

The total energy includes the translational, rotational and vibrational energy, and is a function of T and T_v; the RHS of equation(5.12) is identical to the RHS of equation(2.3) in chapter[2], but with an additional term S_{ev}^{tot} that includes *all* electron vibrational excitation (including excitation of the symmetric N_2O modes).

If we subtract equation(5.7) from equation(5.12) we get the rate of change of the *thermalized* energy, $u_{RT,vs}$, where RT stands for roto-translational and vs stands for symmetric-vibrational:

$$\begin{aligned}\frac{\mathrm{d}}{\mathrm{d}t}\left(\sum n_i u_{i,RT,vs}\right) = \dot{m}_{in}(h_{in} - e_{v,in}) - \sum \Gamma_{exh}^i (h_i - e_{vi}) + \ldots \\ -\Delta H_0 + \sum(\varepsilon_j - \delta h_{0j}) + S_{ev}^{sym} + E_{VT}^{rel}\end{aligned} \tag{5.13}$$

The relaxation term, E_{VT}^{rel}, has appeared as positive heating term; also the term relative to the electron vibrational excitation, of the symmetric modes, has appeared as positive heating term; this two terms represent the flow of energy from the vibrational energy reservoir, to the equilibrium gas thermal reservoir.

5.2.3 Preliminary Results

In this section we present results of preliminary simulations with the model; a thorough investigation will be soon performed with a more extensive simulations campaign. Simulations are performed on a cylindrical chamber with radius $R = 1$ cm and $L = 10$ cm; mass flow rate ranges from 30 to 120 mg/s, input power ranges from 60 to 240 W;

In order to illustrate the benefits of the plasma action, the following figures show the time evolution of several discharge parameters of a sample test case with: input power 60 W, mass flow rate 30 mg/s, exhaust-to-chamber ratio $\varrho^* = 10^{-3}$; figure(5.13) reports the electron temperature and density of the discharge, together with the chamber pressure and the vibrational-to-gas temperature ratio, T_v/T, in the discharge. In this case the discharge is ignited in sub-atmospheric conditions and reach 1 bar at steady state conditions. At the beginning of the simulation there are few electrons and the injected power raises the value of T_e; as the discharge evolves the build up of electron population follows a decrease of T_e.

The fast electron vibrational excitation starts pumping energy into the vibrational degrees of freedom, while the gas temperature increases slowly, see figure(5.14); at certain point, the degree of dissociation and the gas temperature are sufficiently high to trigger the remaining decomposition of the gas; after that, the gas temperature increases to a value that makes the VT relaxation fast enough to thermalize the discharge.

Thermalization does not happens always, because VT relaxation depends not only on the temperature, but also on the pressure of the discharge. Figure(5.14) reports, as comparison, the value of the gas temperature, that would be obtained if the power where transferred to the gas thermally, thus without plasma; the equilibrium thermal simulation is performed with the Cantera model explained in section[5.1.4].

In order to explore the behaviour of the system, and assess the propulsive performances with different discharge parameters, two series of sweeps are performed; for simplicity the radius and length of the chamber are kept fixed to $R = 1$ cm and $L = 10$ cm; the power input P_W, is swept between 60 and 240 W, the mass flow rate is changed also in order to keep fixed the specific power input, $P_w/\dot{m}$ to a value of 2 W/(mg s^{-1}).

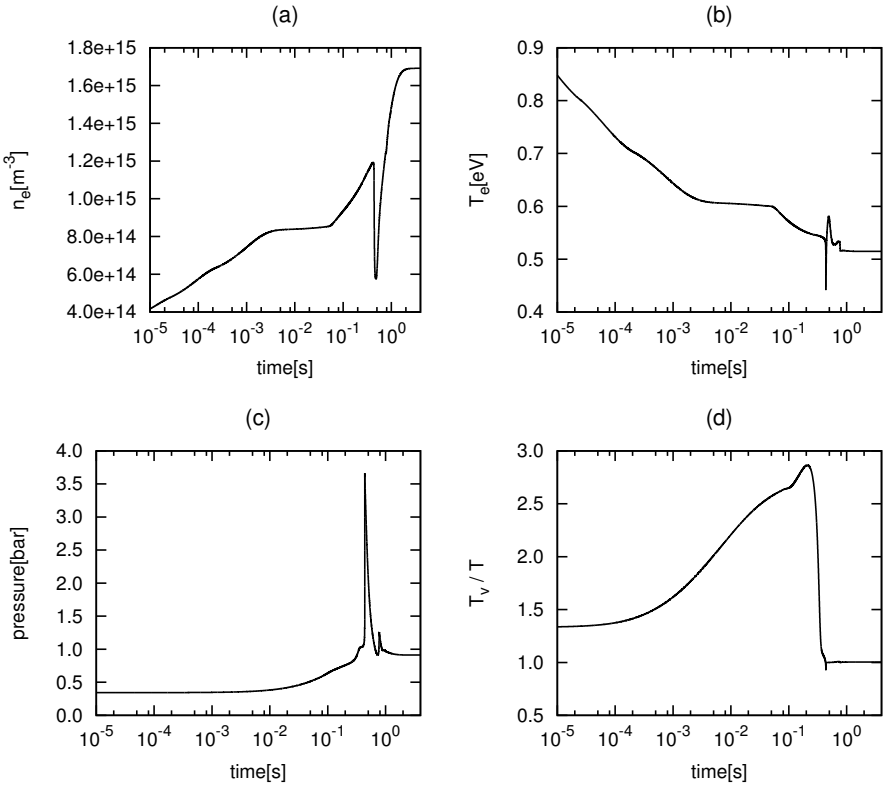

FIGURE 5.13: Simulation time profiles: (a) electron density, (b) electron temperature, (c) pressure, (d) T_v/T. $R = 1$ cm, $L = 10$ cm, $P_W = 60$ W, $\dot{m} = 30$ mg/s, $\varrho^* = 10^{-3}$.

Two series of simulations of N_2O plasma assisted decomposition are presented: the first has an exhaust-to-chamber ratio $\varrho^* = 10^{-3}$, the second has $\varrho^* = 10^{-2}$. Conductive and convective heat losses are accounted for as explained in section[5.2]; propulsive efficiency is calculated with formula(5.5), thrust and specific impulse are calculated with formulas(2.23,2.29,2.30), without considering the (negligible) charged particles contribution; the nozzle expansion ratio $A_{\text{exit}}/A_{\text{throat}}$, the ratio between the exit section area and the throat section area, is set to 225.

Figures[5.15,5.16] report the non equilibrium vibrational temperatures T_v and T, the pressure and the dissociation degree within the discharge, for the two $\varrho^* = 10^{-3}$ and 10^{-2} cases. It is observed that changing the ϱ^* parameter, seems to affect mostly the chamber pressure; moreover, at higher pressures the thermalization is more efficient, while at lower pressures there is a more marked difference between T_v and T.

The values of n_e and T_e, not reported in the figures, result almost constant in these sweeps: $n_e \sim 1.5 \cdot 10^{15}$ m^{-3} and $T_e \sim 0.5$ eV for $\varrho^* = 10^{-3}$, $n_e \sim 1.1 \cdot 10^{16}$ m^{-3} and $T_e \sim 0.6$ eV for $\varrho^* = 10^{-2}$.

Figures[5.17,5.18] report the thrust, specific impulse and propulsive efficiency for the two cases; the thrust exhibits an almost linear trend in both cases; the values achieved by I_{SP}

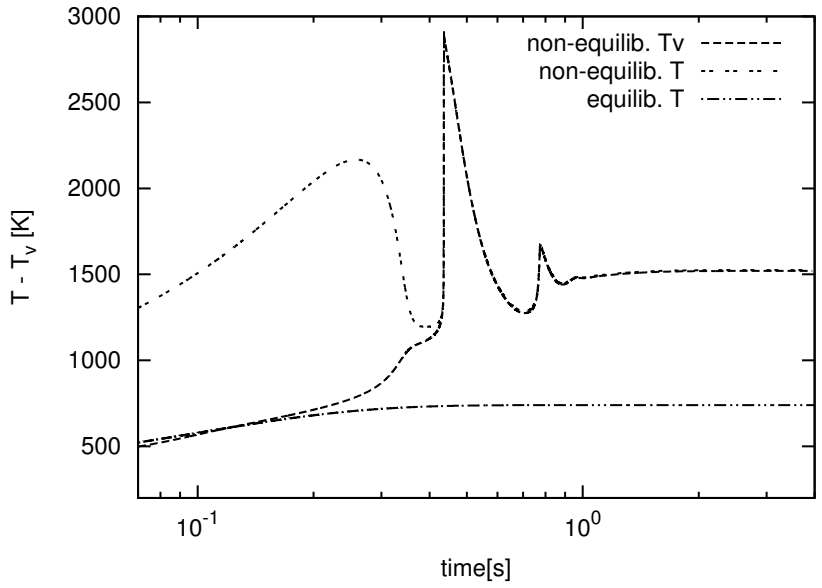

FIGURE 5.14: Simulation time profiles: non equilibrium T_v, T, and equilibrium T. $R = 1$ cm, $L = 10$ cm, $P_W = 60$ W, $\dot{m} = 30$ mg/s, $\varrho^* = 10^{-3}$.

and η_p are satisfactory, with the highest values of 200 s and 50% efficiency. Simulations with intermediate values $10^{-3} < \varrho^* < 10^{-2}$, not reported here, with the same specific power 2 W/(mg s^{-1}), and the same range of power, have displayed a smooth variation of performances, between the two limiting cases reported in figures[5.17,5.18].

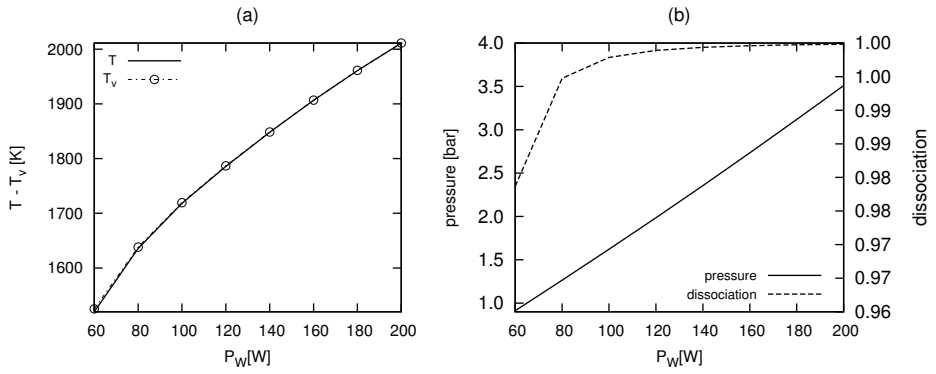

FIGURE 5.15: Simulations with $\varrho^* = 10^{-3}$, P_W = 60-200 W, $\dot{m}$ = 30-100 mg/s (fixed $P_w/\dot{m} = 2$ W/(mg s^{-1})); (a) non equilibrium T_v, T; (b) discharge pressure and dissociation degree.

The VT relaxation heats the gas and helps the decomposition process; however, as was said before, the VT relaxation depends not only on the temperature, but also on the pressure of the discharge; the simulations show that there is a critical value of ϱ^*, given source dimensions and specific input power, beyond which, the VT relaxation is too slow, resulting in an excessive accumulation of energy in the vibrational reservoir, and low values of gas temperatures. An example is reported relative to the first case

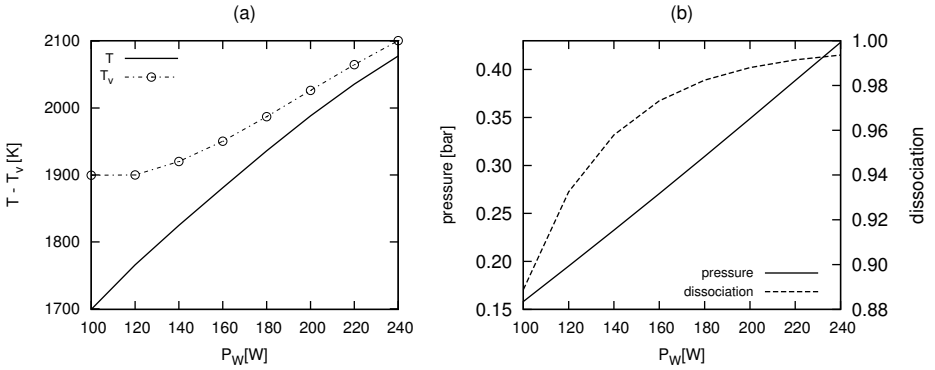

FIGURE 5.16: Simulations with $\varrho^* = 10^{-2}$, P_W = 60-200 W, $\dot{m}$ = 30-100 mg/s (fixed $P_w/\dot{m} = 2$ W/(mg s^{-1})); (a) non equilibrium T_v, T; (b) discharge pressure and dissociation degree.

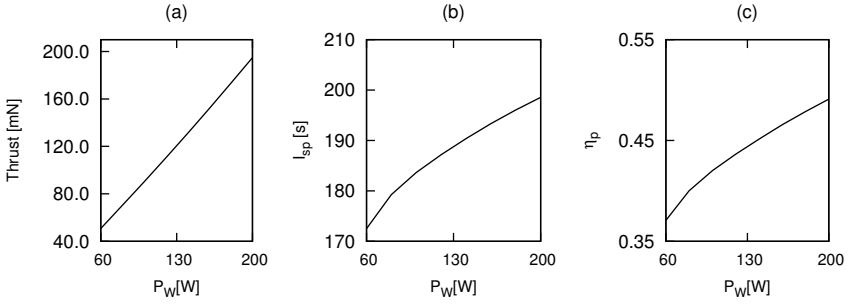

FIGURE 5.17: Simulations with $\varrho^* = 10^{-3}$, P_W = 60-200 W, $\dot{m}$ = 30-100 mg/s (fixed $P_w/\dot{m} = 2$ W/(mg s^{-1})); (a) thrust, (b) specific impulse and (c) propulsive efficiency.

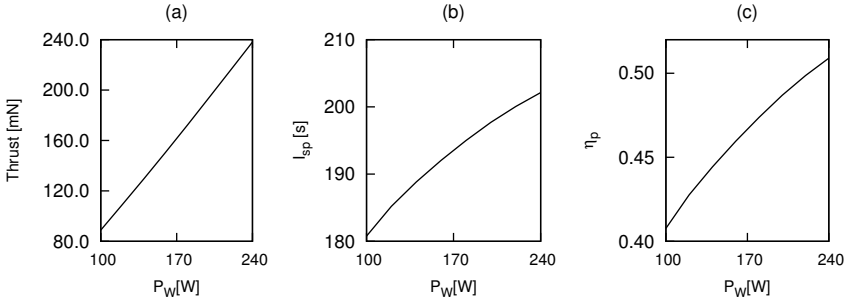

FIGURE 5.18: Simulations with $\varrho^* = 10^{-2}$, P_W = 60-200 W, $\dot{m}$ = 30-100 mg/s (fixed $P_w/\dot{m} = 2$ W/(mg s^{-1})); (a) thrust, (b) specific impulse and (c) propulsive efficiency.

presented: input power 60 W, mass flow rate 30 mg/s, and exhaust-to-chamber ratio $\varrho^* = 10^{-2}$ instead of 10^{-3}. Figure[5.19a] shows that the vibrational temperature goes higher to a value of 5500 K, while the gas temperature sets to about 750 K; Figure[5.19b] reports the chamber pressure and the dissociation degree; we can see that, though the gas temperature is low, 750 K, the dissociation, promoted by the very high T_v, is as high as 20%; this value would not be achievable by a N_2O gas in thermal equilibrium at 750 K (for the same conditions, the Cantera model provides 740 K temperature and 10^{-5} dissociation degree).

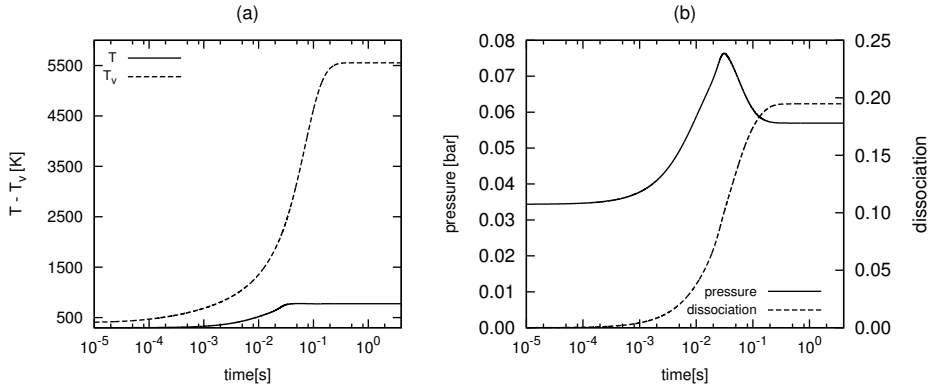

FIGURE 5.19: Simulation time profiles:(a) non equilibrium T_v, T and (b) discharge pressure and dissociation degree. $R = 1$ cm, $L = 10$ cm, $P_W = 60$ W, $\dot{m} = 30$ mg/s, $\varrho^* = 10^{-2}$.

To end this section, we present some additional remarks regarding electrical power and mass flow rate variation trends. In figure[5.20] a sweep is performed varying only the input power, while keeping fixed the other parameters; the figure refers to a case with $R = 1$ cm, $L = 10$ cm, $\dot{m} = 30$ mg/s, $\varrho^* = 10^{-2}$, and P_W from 60 to 200 W. The figure shows that it is possible to increase the specific impulse at the expenses of the efficiency. In figure[5.21] a sweep is performed varying only the mass flow rate, while keeping fixed the other parameters; the figure refers to a case with $R = 1$ cm, $L = 10$ cm, $P_W = 100$ W, $\varrho^* = 10^{-2}$, and $\dot{m}$ from 40 to 60 mg/s. The figure shows that is possible to increase the efficiency at the expenses of the specific impulse.

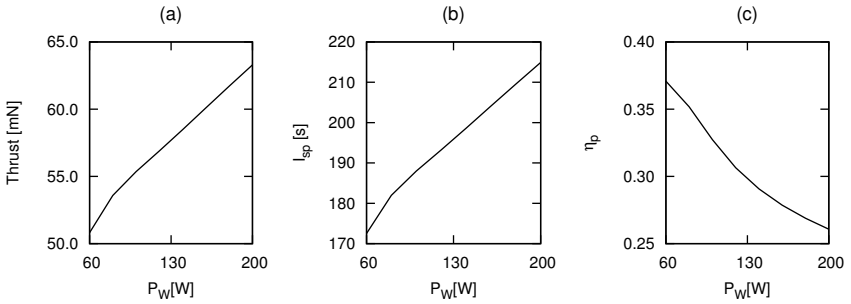

FIGURE 5.20: Simulations with $\varrho^* = 10^{-3}$, P_W = 60-200 W, $\dot{m}$ = 30 mg/s; (a) thrust, (b) specific impulse and (c) propulsive efficiency.

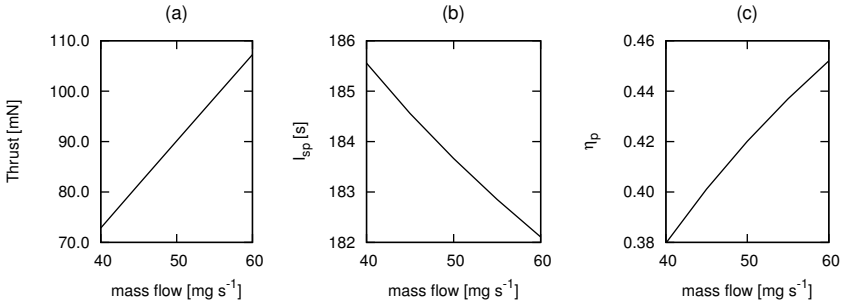

FIGURE 5.21: Simulations with $\varrho^* = 10^{-3}$, P_W = 100 W, $\dot{m}$ = 40-60 mg/s; (a) thrust, (b) specific impulse and (c) propulsive efficiency.

Chapter 6

Conclusions

In this work several plasma global models have been developed, with the purpose to be used in Helicon plasma propulsion and plasma assisted combustion investigations.

The mathematical frame of the plasma models is presented, in the first chapter, in the more general view of global modelling of magnetized discharges for electronegative gases; the models are particularized for space propulsion applications by means of thruster exhaust coefficients, which were derived by means of particle in cell simulations. However, the presented relationships for diffusion of charges and computation of plasma processes can be applied to any type of cold plasma discharge, from high vacuum glow, to atmospheric DBD, provided that the model is complemented with a Boltzmann solver for the electron distribution function, for those cases where the ionization fraction is small. Furthermore, the reviewed and compiled kinetic database, presented in the tables at the end of the chapter, is applicable to atmospheric air discharges and carbon dioxide plasma discharges, that have interested the European research community lately.

In order to gain confidence with the predictions of the model, electron density measurements have been performed; the electron temperature have been qualitatively estimated by means of optical emission spectroscopy. The small dimensions of the source chamber, wrapped with the magnetic field generation system and the RF excitation antenna, together with interference produced by high RF fields, makes difficult th use of Langmuir probes for direct measurement of the electron temperature. Non intrusive methods are preferred in this case, nonetheless, the measured electron densities and the estimated electron temperatures are in good agreement with the predictions of the model.

The helicon experiments literature review and comparison, presented in the second chapter, emphasize the good efficiency of the source developed at CISAS; the global model

simulations indicates also that, in order to get good propulsive performances, high electron temperatures and ionization fractions, it is necessary to operate with high values of the exhaust-to-chamber ratio $\varrho^* \sim 0.9$, therefore operating the source at lower pressure values. Simulation shows that the thruster can reach specific impulse as high as 3500 s with Ar and 3000 s with CO_2, with efficiencies of 55 % and 45 % respectively.

Nowadays, investigative efforts on HPT technology, at CISAS, are focused on the high power regime operation of the thruster, with either Argon gas than carbon dioxide gas.

In this thesis, a work on plasma assisted decomposition of nitrous oxide was also presented in the last chapter.

Experiments on a gliding arc reactor appositely designed, at Drexel Plasma Institute (Philadelphia), show that the catalytic action of the plasma is effective in decomposing the molecule and promoting monopropellant combustion. Efficiency of an equivalent device exhausting in vacuum, with the same chamber pressure and temperature, is about 43%, and it compares positively with the 27% efficiency of the existing nitrous oxide resistojets. Higher values of efficiency could be achieved, following electrodes, discharge dimensions and parameters optimization.

A global model for plasma assisted combustion, applied to monopropellant propulsion, is developed and presented in the last chapter. The model is able to reveal the mechanism of plasma catalysis, and predicts good performances for an hypothetical N_2O microwave discharge thruster, specific impulses up to 200 s and efficiencies up to 50 %. Also in this case, the mathematical formulas adopted in the model are independent on the specific application; the model could be extended, for instance, with the CO_2 reactions dataset, in order to investigate microwave discharges for carbon dioxide conversion.

Appendix A

Reactions dataset

Ar model kinetic scheme

TABLE A.1: Ar model reactions dataset.

Reaction	Rate Constant 2nd order (cm^3/s)	Reference
$e + Ar \rightarrow e + Ar$	$2.336 \cdot 10^{-14} T_e^{1.609} \exp(0.0618 \ln^2(T_e) - 0.117 \ln^3(T_e))$	[7]
$e + Ar \rightarrow e + Ar(4s)$	$5.0 \cdot 10^{-15} T_e^{0.74} \exp(-11.56/T_e)$	[7]
$e + Ar \rightarrow e + Ar(4p)$	$1.4 \cdot 10^{-14} T_e^{0.71} \exp(-13.2/T_e)$	[7]
$e + Ar \rightarrow e + Ar^+$	$2.34 \cdot 10^{-14} T_e^{0.59} \exp(-17.44/T_e)$	[7]
$e + Ar(4s) \rightarrow e + Ar$	$4.3 \cdot 10^{-16} T_e^{0.74}$	[7]
$e + Ar(4p) \rightarrow e + Ar$	$3.9 \cdot 10^{-16} T_e^{0.71}$	[7]
$e + Ar(4s) \rightarrow e + Ar(4p)$	$8.9 \cdot 10^{-13} T_e^{0.51} \exp(-17.59/T_e)$	[7]
$e + Ar(4s) \rightarrow e + Ar^+$	$6.8 \cdot 10^{-15} T_e^{0.67} \exp(-4.20/T_e)$	[7]
$e + Ar(4p) \rightarrow e + Ar(4s)$	$3.0 \cdot 10^{-13} T_e^{0.51}$	[7]
$e + Ar(4p) \rightarrow e + Ar^+$	$1.8 \cdot 10^{-13} T_e^{0.61} \exp(-2.61/T_e)$	[7]
Surface reactions	**Recombination factor (s^{-1})**	
$Ar^+ \rightarrow Ar$	$\gamma = 1$	
$Ar(4s) \rightarrow Ar$	$\gamma = 1$	
$Ar(4p) \rightarrow Ar$	$\gamma = 1$	
Exhaust Coefficients		
α	7.75	
β	0.49	

1. T_e is in eV

Multi species model kinetic scheme

TABLE A.2: H_2 model reactions dataset.

Reaction	Rate Constant 2nd order (cm^3/s) 3rd order (cm^6/s)	Reference
$e + H \rightarrow e + H(_2p)$	Bolsig	[43]
$e + H \rightarrow e + H(_2s)$	Bolsig	[43]
$e + H(_2s) \rightarrow e + H(_2p)$	$3.5 \cdot 10^{-6}$	[88]
$e + H \rightarrow e + e + H^+$	$1.75 \cdot 10^{-8} \exp(-15.4/T_e)$	[88]
$e + H(_2s) \rightarrow e + e + H^+$	Bolsig	[43]
$e + H_2 \rightarrow e + H_2^*(J, v)$	Bolsig	[43, 89]
$e + H_2 \rightarrow e + H_2(B^1)$	Bolsig	[43, 89]
$e + H_2 \rightarrow e + H_2(C^3 - A^3)$	Bolsig	[43, 89]
$e + H_2 \rightarrow e + H_2^*$	Bolsig	[43, 89]
$e + H_2 \rightarrow e + e + H_2^+$	Bolsig	[43, 89]
$e + H_2(B^1) \rightarrow e + e + H_2^+$	Bolsig	[43, 89]
$e + H_2(C^3 - A^3) \rightarrow e + e + H_2^+$	Bolsig	[43, 89]
$e + H_2 \rightarrow e + e + H + H^+$	$3.07 \cdot 10^{-10} \exp(-17.5/T_e)$	[88]
$e + H_2 \rightarrow e + H + H$	$1.2 \cdot 10^{-8} \exp(-10.0/T_e)$	[88]
$e + H_2 \rightarrow e + H + H(_2s)$	$4.71 \cdot 10^{-9} \exp(-15.9/T_e)$	[88]
$e + H_2 \rightarrow e + H(_2p) + H(_2s)$	$1.78 \cdot 10^{-9} \exp(-28.34/T_e)$	[88]
$e + H_2 \rightarrow e + H + H^*$	$3.74 \cdot 10^{-10} \exp(-18.0/T_e)$	[88]
$e + H^+ \rightarrow H$	$4.0 \cdot 10^{-13}/{T_e}^{0.5}$	[90]
$e + H_2^+ \rightarrow H + H$	$8.0 \cdot 10^{-8} \exp(-0.2/T_e)$	[88]
$e + H_2^+ \rightarrow e + H + H^+$	$1.45 \cdot 10^{-7} \exp(-1.97/T_e)$	[88]
$e + H_3^+ \rightarrow H_2 + H$	$1.55 \cdot 10^{-6}(300.0/T)$	[88]
$e + H_3^+ \rightarrow e + H_2^+ + H$	$4.85 \cdot 10^{-10}(1/{T_e}^{0.05}) \exp(-19.16/T_e)$	[91]
$e + H_3^+ \rightarrow H + H + H$	$0.5[8.39 \cdot 10^{-9} + 3.01 \cdot 10^{-9}T_e +$ $-3.8 \cdot 10^{-10}{T_e}^2 + 1.31 \cdot 10^{-11}{T_e}^3 + 2.4 \cdot 10^{-13}{T_e}^4 +$ $-2.3 \cdot 10^{-14}{T_e}^5 + 3.5 \cdot 10^{-16}{T_e}^6]$	[91]
$H_2 + H_2^+ \rightarrow H_3^+ + H$	$2.1 \cdot 10^{-9}$	[88]
$H_2^+ + H \rightarrow H_2 + H^+$	$9.0 \cdot 10^{-10}$	[91]
$H^+ + H_2 \rightarrow H + H_2^+$	$1.19 \cdot 10^{-22}$	[91]
$H(_2p) \rightarrow H$	$4.74 \cdot 10^{7}$	[88]
$H + H + H_2 \rightarrow H_2 + H_2$	$8.85 \cdot 10^{-33}(298/T)^{0.6}$	[55]
$H_2 + H_2 \rightarrow H_2 + H + H$	$2.61 \cdot 10^{-8}(270/T)^{0.7} \exp(-52562/T)$	[55]
$H_2 + H \rightarrow H + H + H$	$2.54 \cdot 10^{-8}(298/T)^{0.1} \exp(-52562/T)$	[55]
$H + H + H \rightarrow H + H_2$	$8.82 \cdot 10^{-33}$	[55]

Surface reactions	Recombination factor (s^{-1})
$H_3^+ \rightarrow H_2 + H$	$\gamma = 1$

$H_2^+ \rightarrow H_2$	$\gamma = 1$
$H^+ \rightarrow H$	$\gamma = 1$
$H(_2s) \rightarrow H$	$\gamma = 1$
$H(_2p) \rightarrow H$	$\gamma = 1$
Exhaust Coefficients	
$\alpha(H_3^+) = 6.14$	$\beta(H_3^+) = 1.53$
$\alpha(H_2^+) = 6.35$	$\beta(H_2^+) = 2.73$
$\alpha(H^+) = 9.16$	$\beta(H^+) = 3.26$

1. T and T_e are expressed in K and eV, respectively
2. Excited states not tracked as distinct species: (*) electronic, $^*(J, v)$ rotational and vibrational.

TABLE A.3: N_2 model reactions dataset.

Reaction	Rate Constant 2nd order (cm^3/s) 3rd order (cm^6/s)	Reference
$e + N_2 \rightarrow e + N_2(v^*)$	Bolsig	[43, 89]
$e + N_2 \rightarrow e + N_2(A^3)(v^*)$	Bolsig	[43, 89]
$e + N_2 \rightarrow e + N_2(B^3)$	Bolsig	[43, 89]
$e + N_2 \rightarrow e + N_2(B^3)^*$	Bolsig	[43, 89]
$e + N_2 \rightarrow e + N_2(a'^1)$	Bolsig	[43, 89]
$e + N_2 \rightarrow e + N_2(a'^1)^*$	Bolsig	[43, 89]
$e + N_2 \rightarrow e + N_2(C^3)$	Bolsig	[43, 89]
$e + N_2 \rightarrow e + N_2(C^3)^*$	Bolsig	[43, 89]
$e + N_2 \rightarrow e + N + N(_2D)$	Bolsig	[43, 89]
$e + N_2 \rightarrow e + e + N_2^+$	Bolsig	[43, 89]
$e + N_2(A^3) \rightarrow e + e + N_2^+$	Bolsig	[43, 89]
$e + N \rightarrow e + e + N^+$	Bolsig	[43, 89]
$e + N_2^+ \rightarrow N + N$	$0.50[1.8 \cdot 10^{-7}(300/T_e(K))^{0.39}$	[25]
$e + N_2^+ \rightarrow N + N(_2D)$	$0.45[1.8 \cdot 10^{-7}(300/T_e(K))^{0.39}$	[25]
$e + N_2^+ \rightarrow N + N(_2P)$	$0.05[1.8 \cdot 10^{-7}(300/T_e(K))^{0.39}$	[25]
$e + N^+ + e \rightarrow N + e$	$7.0 \cdot 10^{-20}(300/T_e(K))^{4.5}$	[25]
$e + N^+ + N_2 \rightarrow N + N_2$	$6.0 \cdot 10^{-27}(300/T_e(K))^{1.5}$	[25]
$N_2(A^3) + N \rightarrow N_2 + N$	$2.0 \cdot 10^{-12}$	[25]
$N_2(A^3) + N \rightarrow N_2 + N(_2P)$	$4.0 \cdot 10^{-11}(300/T)^{0.667}$	[25]
$N_2(A^3) + N_2 \rightarrow N_2 + N_2$	$3.0 \cdot 10^{-16}$	[25]
$N_2(A^3) + N_2(A^3) \rightarrow N_2 + N_2(B^3)$	$3.0 \cdot 10^{-10}$	[25]
$N_2(A^3) + N_2(A^3) \rightarrow N_2 + N_2(C^3)$	$1.5 \cdot 10^{-10}$	[25]
$N_2(B^3) + N_2 \rightarrow N_2(A^3) + N_2$	$3.0 \cdot 10^{-11}$	[25]
$N_2(B^3) + N_2 \rightarrow N_2 + N_2$	$2.0 \cdot 10^{-12}$	[25]
$N_2(C^3) + N_2 \rightarrow N_2(a'^1) + N_2$	$1.0 \cdot 10^{-11}$	[25]
$N_2(a'^1) + N_2 \rightarrow N_2(B^3) + N_2$	$1.9 \cdot 10^{-13}$	[25]
$N + N + M \rightarrow N_2(A^3) + M$	$1.7 \cdot 10^{-33}$	[25]
$N + N + N \rightarrow N_2(A^3) + N$	10^{-32}	[25]
$N + N + M \rightarrow N_2(B^3) + M$	$2.4 \cdot 10^{-33}$	[25]
$N + N + N \rightarrow N_2(B^3) + N$	$1.4 \cdot 10^{-32}$	[25]
$N(_2D) + N_2 \rightarrow N + N_2$	$1.0 \cdot 10^{-13}\exp(-510/T)$	[25]
$N(_2P) + N \rightarrow N + N$	$1.8 \cdot 10^{-12}$	[25]
$N(_2P) + N \rightarrow N(_2D) + N$	$6.0 \cdot 10^{-13}$	[92]
$N(_2P) + N_2 \rightarrow N + N_2$	$6.0 \cdot 10^{-14}$	[92]
$N(_2P) + N(_2D) \rightarrow N_2^+ + e$	$1.0 \cdot 10^{-13}$	[92]
$N + N \rightarrow N_2^+ + e$	$2.7 \cdot 10^{-11}\exp(-6.74 \cdot 10^4/T)$	[25]
$N_2 + M \rightarrow N + N + M$	$5.4 \cdot 10^{-8}(1 - \exp(-3354/T))\exp(-113200/T)$	[25]
$N_2 + N \rightarrow N + N + N$	$6.6[5.4 \cdot 10^{-8}(1 - \exp(-3354/T))\exp(-113200/T)]$	[25]
$N + N + N_2 \rightarrow N_2 + N_2$	$MAX(8.3 \cdot 10^{-34}\exp(500/T), 1.91 \cdot 10^{-33})$	[25]
$N + N + N \rightarrow N_2 + N$	$3.0[1.8 \cdot 10^{-33}\exp(435/T)]$	[25]

$N_2^+ + N \rightarrow N^+ + N_2$	$7.2 \cdot 10^{-13}(T/300)$	[25]
$N^+ + N + M \rightarrow N_2^+ + M$	$1.0 \cdot 10^{-29}$	[25]

Spontaneous emission	(s^{-1})	
$N_2(A^3) \rightarrow N_2$	0.50	[25]
$N_2(B^3) \rightarrow N_2(A^3)$	$1.34 \cdot 10^5$	[25]
$N_2(a'^1) \rightarrow N_2$	$1.0 \cdot 10^2$	[25]
$N_2(C^3) \rightarrow N_2(B^3)$	$2.45 \cdot 10^7$	[25]

Surface reactions	Recombination factor (s^{-1})	
$N_2^+ \rightarrow N_2$	$\gamma = 1$	
$N^+ \rightarrow N$	$\gamma = 1$	
$N_2(A^3) \rightarrow N_2$	$\gamma = 1$	[25]
$N_2(a'^1) \rightarrow N_2$	$\gamma = 10^{-2}$	[25]
$N(_2D) \rightarrow N$	$\gamma = 1$	
$N(_2P) \rightarrow N$	$\gamma = 1$	
$2\,N \rightarrow N_2$	$\gamma = 8.0 \cdot 10^{-4}$	[93]
Exhaust Coefficients		
$\alpha(N_2^+) = 7.23$	$\beta(N_2^+) = 0.55$	
$\alpha(N^+) = 6.59$	$\beta(N^+) = 0.58$	

1. T and $T_e(K)$ are expressed both in K.
2. Excited states not tracked as distinct species: (*) electronic and $^*(v)$ vibrational.
3. $N_2(A^3)(v^*)$ vibrational excited A^3 state.
2. $N_2(B^3\Pi)^*$ stands for $N_2(B'^3\Sigma)$ and $N_2(W^3\Delta)$, which relax istantly to $N_2(B^3\Pi)$ state [44].
5. $N_2(a^1\Sigma)^*$ stands for $N_2(a^1\Pi)$ and $N_2(w^1\Delta)$, which relax istantly to $N_2(a'^1\Sigma)$ state [44].
6. $N_2(C^3\Pi)^*$ stands for $N_2(a''^1\Sigma)$ and $N_2(E^3\Sigma)$, which relax istantly to $N_2(C^3\Pi)$ state [44].
7. M is third body reaction partner M = N_2.

TABLE A.4: O_2 model reactions dataset.

Reaction	Rate Constant 2nd order (cm^3/s) 3rd order (cm^6/s)	Reference
$e + O_2 \rightarrow e + O_2(^*v)$	Bolsig	[43, 94]
$e + O_2 \rightarrow e + O_2(a^1)$	Bolsig	[43, 94]
$e + O_2 \rightarrow e + O_2(b^1)$	Bolsig	[43, 94]
$e + O_2 \rightarrow e + O_2(4.5eV)$	Bolsig	[43, 94]
$e + O_2 \rightarrow e + O + O$	Bolsig	[43, 94]
$e + O_2 \rightarrow e + O + O(_1D)$	Bolsig	[43, 94]
$e + O_2 \rightarrow e + O + O(_1S)$	Bolsig	[43, 94]
$e + O_2 \rightarrow e + e + O_2^+$	Bolsig	[43, 94]
$e + O_2(a^1) \rightarrow e + O + O$	Bolsig	[43, 94]
$e + O_2(a^1) \rightarrow e + e + O_2^+$	Bolsig	[43, 94]
$e + O_2(b^1) \rightarrow e + e + O_2^+$	Bolsig	[43, 94]
$e + O_2(4.5eV) \rightarrow e + e + O_2^+$	Bolsig	[43, 94]
$e + O \rightarrow e + O(_1D)$	Bolsig	[43, 94]
$e + O \rightarrow e + O(_1S)$	Bolsig	[43, 94]
$e + O \rightarrow e + e + O^+$	Bolsig	[43, 94]
$e + O_2^+ \rightarrow O + O$	$0.55[2.7 \cdot 10^{-7}(300/T_e(K))^{0.7}]$	[25]
$e + O_2^+ \rightarrow O + O(_1D)$	$0.4[2.7 \cdot 10^{-7}(300/T_e(K))^{0.7}]$	[25]
$e + O_2^+ \rightarrow O + O(_1S)$	$0.05[2.7 \cdot 10^{-7}(300/T_e(K))^{0.7}]$	[25]
$e + O_4^+ \rightarrow O_2 + O_2$	$1.4 \cdot 10^{-6}(300/T_e(K))^{0.5}$	[25]
$e + O^+ + e \rightarrow O + e$	$7.0 \cdot 10^{-20}(300/T_e(K))^{4.5}$	[25]
$e + O^+ + M \rightarrow O + M$	$6.0 \cdot 10^{-27}(300/T_e(K))^{1.5}$	[25]
$e + O_2 \rightarrow O^- + O$	Bolsig	[43, 94]
$e + O_3 \rightarrow O_2^- + O$	$1.0 \cdot 10^{-9}$	[25]
$e + O_3 \rightarrow O^- + O_2$	$1.0 \cdot 10^{-11}$	[25]
$e + O + O_2 \rightarrow O^- + O_2$	$1.0 \cdot 10^{-31}$	[25]
$e + O + O_2 \rightarrow O_2^- + O$	$1.0 \cdot 10^{-31}$	[25]
$e + O_3 + O_2 \rightarrow O_3^- + O_2$	$1.0 \cdot 10^{-31}$	[25]
$e + O_2 + O_2 \rightarrow O_2^- + O_2$	$1.4 \cdot 10^{-29}(300/T_e(K)) \exp(-600/T)$	[95]
$O^- + O \rightarrow O_2 + e$	$1.4 \cdot 10^{-10}$	[25]
$O^- + O_2 \rightarrow O_3 + e$	$5.0 \cdot 10^{-15}$	[25]
$O^- + O_2(a^1) \rightarrow O_3 + e$	$3.0 \cdot 10^{-10}$	[25]
$O^- + O_2(b^1) \rightarrow O + O_2 + e$	$6.9 \cdot 10^{-10}$	[25]
$O^- + O_3 \rightarrow O_2 + O_2 + e$	$3.0 \cdot 10^{-10}$	[25]
$O_2^- + O \rightarrow O_3 + e$	$1.5 \cdot 10^{-10}$	[25]
$O_2^- + O_2 \rightarrow O_2 + O_2 + e$	$2.7 \cdot 10^{-10}(T/300)^{0.5} \exp(-5590/T)$	[25]
$O_2^- + O_2(a^1) \rightarrow O_2 + O_2 + e$	$2.0 \cdot 10^{-10}$	[25]
$O_2^- + O_2(b^1) \rightarrow O_2 + O_2 + e$	$3.6 \cdot 10^{-10}$	[25]
$O_3^- + O \rightarrow O_2 + O_2 + e$	$3.0 \cdot 10^{-10}$	[25]
$O_2(a^1) + O \rightarrow O_2 + O$	$7.0 \cdot 10^{-16}$	[25]
$O_2(a^1) + O_2 \rightarrow O_2 + O_2$	$3.8 \cdot 10^{-18} \exp(-205/T)$	[25]

$O_2(a^1) + O_3 \rightarrow O_2 + O_2 + O(_1D)$	$5.2 \cdot 10^{-11} \exp(-2840/T)$	[25]
$O_2(a^1) + O_2(a^1) \rightarrow O_2 + O_2(b^1)$	$7.0 \cdot 10^{-28} T^{3.8} \exp(700/T)$	[25]
$O + O_3 \rightarrow O_2 + O_2(a^1)$	$1.0 \cdot 10^{-11} \exp(-2300/T)$	[25]
$O_2(b^1) + O \rightarrow O_2(a^1) + O$	$8.1 \cdot 10^{-14}$	[25]
$O_2(b^1) + O \rightarrow O_2 + O(_1D)$	$3.4 \cdot 10^{-11} (300/T)^{0.1} \exp(-4200/T)$	[25]
$O_2(b^1) + O_2 \rightarrow O_2(a^1) + O_2$	$4.3 \cdot 10^{-22} T^{2.4} \exp(-281/T)$	[25]
$O_2(b^1) + O_3 \rightarrow O_2 + O_2 + O$	$2.2 \cdot 10^{-11}$	[25]
$O_2(4.5eV) + O \rightarrow O_2 + O(_1S)$	$9.0 \cdot 10^{-12}$	[25]
$O + O + M \rightarrow O_2(a^1) + M$	$0.07[6.1 \cdot 10^{-9}(1 - \exp(-2240/T)) \exp(-59380/T)]$	[25]
$O + O + O_2 \rightarrow O_2(a^1) + O_2$	$0.343[6.1 \cdot 10^{-9}(1 - \exp(-2240/T)) \exp(-59380/T)]$	[25]
$O + O + O \rightarrow O_2(a^1) + O$	$1.4[6.1 \cdot 10^{-9}(1 - \exp(-2240/T)) \exp(-59380/T)]$	[25]
$O + O + M \rightarrow O_2(b^1) + M$	$0.01[6.1 \cdot 10^{-9}(1 - \exp(-2240/T)) \exp(-59380/T)]$	[25]
$O_2(a^1) + O_2(a^1) + O_2 \rightarrow O_3 + O_3$	$1.0 \cdot 10^{-31}$	[25]
$O(_1D) + O \rightarrow O + O$	$8.0 \cdot 10^{-12}$	[25]
$O(_1D) + O_2 \rightarrow O + O_2$	$6.4 \cdot 10^{-12} \exp(67/T)$	[25]
$O(_1D) + O_2 \rightarrow O + O_2(a^1)$	$1.0 \cdot 10^{-12}$	[25]
$O(_1D) + O_2 \rightarrow O + O_2(b^1)$	$2.6 \cdot 10^{-11} \exp(67/T)$	[25]
$O(_1D) + O_3 \rightarrow O_2 + O + O$	$1.2 \cdot 10^{-10}$	[25]
$O(_1D) + O_3 \rightarrow O_2 + O_2$	$1.2 \cdot 10^{-10}$	[25]
$O(_1S) + O \rightarrow O(_1D) + O$	$5.0 \cdot 10^{-11} \exp(-300/T)$	[95]
$O(_1S) + O_2 \rightarrow O(_1D) + O_2$	$1.3 \cdot 10^{-12} \exp(-850/T)$	[95]
$O(_1S) + O_2 \rightarrow O + O + O$	$3.0 \cdot 10^{-12} \exp(-850/T)$	[95]
$O(_1S) + O_2(a^1) \rightarrow O + O + O$	$1.1 \cdot 10^{-10}$	[95]
$O(_1S) + O_2(a^1) \rightarrow O(_1D) + O_2(b^1)$	$2.9 \cdot 10^{-11}$	[95]
$O(_1S) + O_2(a^1) \rightarrow O + O + O$	$3.2 \cdot 10^{-11}$	[95]
$O(_1S) + O_3 \rightarrow O_2 + O_2$	$2.9 \cdot 10^{-10}$	[95]
$O(_1S) + O_3 \rightarrow O_2 + O + O(_1D)$	$2.9 \cdot 10^{-10}$	[95]
$O + O_3 \rightarrow O_2 + O_2(a^1)$	$2.0 \cdot 10^{-11} \exp(-2280/T)$	[25]
$O_2 + O_2 \rightarrow O + O_3$	$2.0 \cdot 10^{-11} \exp(-49800/T)$	[25]
$O_2 + M \rightarrow O + O + M$	$6.1 \cdot 10^{-9}(1 - \exp(-2240/T)) \exp(-59380/T)$	[25]
$O_2 + O_2 \rightarrow O + O + O_2$	$4.9[6.1 \cdot 10^{-9}(1 - \exp(-2240/T)) \exp(-59380/T)$	[25]
$O_2 + O \rightarrow O + O + O$	$20.0[6.1 \cdot 10^{-9}(1 - \exp(-2240/T)) \exp(-59380/T)$	[25]
$O_3 + O_2 \rightarrow O_2 + O + O_2$	$0.38[6.6 \cdot 10^{-10} \exp(-11600/T)]$	[25]
$O_3 + O \rightarrow O_2 + O + O$	$6.3[6.6 \cdot 10^{-10} \exp(-11600/T) \exp(170/T)]$	[25]
$O + O + O_2 \rightarrow O_2 + O_2$	$4.0 \cdot 10^{-33} (300/T)^{0.41}$	[25]
$O + O + O \rightarrow O_2 + O$	$3.6[4.0 \cdot 10^{-33} (300/T)^{0.41}]$	[25]
$O + O_2 + O_2 \rightarrow O_3 + O_2$	$7.6 \cdot 10^{-34} (300/T)^{1.9}$	[25]
$O + O_2 + O \rightarrow O_3 + O$	$min[3.9 \cdot 10^{-33} (300/T)^{1.9}, 1.1 \cdot 10^{-34} \exp(1060/T)]$	[25]
$O^+ + O_2 \rightarrow O_2^+ + O$	$2.0 \cdot 10^{-11} (300/T)^{0.5}$	[25]
$O^+ + O_3 \rightarrow O_2^+ + O_2$	$1.0 \cdot 10^{-10}$	[25]
$O_4^+ + O_2 \rightarrow O_2^+ + O_2 + O_2$	$3.3 \cdot 10^{-6} (300/T)^{4.0} \exp(-5030/T)$	[25]
$O_4^+ + O_2(a^1) \rightarrow O_2^+ + O_2 + O_2$	$1.0 \cdot 10^{-10}$	[25]
$O_4^+ + O_2(b^1) \rightarrow O_2^+ + O_2 + O_2$	$1.0 \cdot 10^{-10}$	[25]
$O_4^+ + O \rightarrow O_2^+ + O_3$	$3.0 \cdot 10^{-10}$	[25]
$O^+ + O + M \rightarrow O_2^+ + M$	$1.0 \cdot 10^{-29}$	[25]
$O_2^+ + O_2 + O_2 \rightarrow O_4^+ + O_2$	$2.4 \cdot 10^{-30} (300/T)^{3.2}$	[25]
$O^- + O_2(a^1) \rightarrow O_2^- + O$	$1.0 \cdot 10^{-10}$	[25]

$O^- + O_3 \rightarrow O_3^- + O$	$8.0 \cdot 10^{-10}$	[25]
$O_2^- + O \rightarrow O^- + O_2$	$3.3 \cdot 10^{-10}$	[25]
$O_2^- + O_3 \rightarrow O_3^- + O_2$	$3.5 \cdot 10^{-10}$	[25]
$O_3^- + O \rightarrow O_2^- + O_2$	$3.2 \cdot 10^{-10}$	[95]
$O_4^- + M \rightarrow O_2^- + O_2 + M$	$1.0 \cdot 10^{-10} \exp(-1044/T)$	[95]
$O_4^- + O \rightarrow O_3^- + O_2$	$4.0 \cdot 10^{-10}$	[95]
$O_4^- + O \rightarrow O^- + O_2 + O_2$	$3.0 \cdot 10^{-10}$	[95]
$O_4^- + O_2(a^1) \rightarrow O_2^- + O_2 + O_2$	$1.0 \cdot 10^{-10}$	[95]
$O_4^- + O_2(b^1) \rightarrow O_2^- + O_2 + O_2$	$1.0 \cdot 10^{-10}$	[95]
$O^- + O_2 + M \rightarrow O_3^- + M$	$1.1 \cdot 10^{-30}(300/T)$	[95]
$O_2^- + O_2 + M \rightarrow O_4^- + M$	$3.5 \cdot 10^{-31}(300/T)$	[95]
$O^- + O^+ \rightarrow O + O$	$2.0 \cdot 10^{-7}(300/T)^{0.5}$	[95]
$O^- + O_2^+ \rightarrow O + O_2$	$2.0 \cdot 10^{-7}(300/T)^{0.5}$	[95]
$O^- + O_2^+ \rightarrow O + O + O$	$1.0 \cdot 10^{-7}$	[95]
$O^- + O_4^+ \rightarrow O + O_2 + O_2$	$1.0 \cdot 10^{-7}$	[95]
$O_2^- + O^+ \rightarrow O_2 + O$	$2.0 \cdot 10^{-7}(300/T)^{0.5}$	[95]
$O_2^- + O_2^+ \rightarrow O_2 + O_2$	$2.0 \cdot 10^{-7}(300/T)^{0.5}$	[95]
$O_2^- + O_2^+ \rightarrow O_2 + O + O$	$1.0 \cdot 10^{-7}$	[95]
$O_2^- + O_4^+ \rightarrow O_2 + O_2 + O_2$	$1.0 \cdot 10^{-7}$	[95]
$O_3^- + O^+ \rightarrow O_3 + O$	$2.0 \cdot 10^{-7}(300/T)^{0.5}$	[95]
$O_3^- + O_2^+ \rightarrow O_3 + O_2$	$2.0 \cdot 10^{-7}(300/T)^{0.5}$	[95]
$O_3^- + O_2^+ \rightarrow O_3 + O + O$	$1.0 \cdot 10^{-7}$	[95]
$O_3^- + O_4^+ \rightarrow O_3 + O_2 + O_2$	$1.0 \cdot 10^{-7}$	[95]
$O_4^- + O^+ \rightarrow O_2 + O_2 + O$	$1.0 \cdot 10^{-7}$	[95]
$O_4^- + O_2^+ \rightarrow O_2 + O_2 + O_2$	$1.0 \cdot 10^{-7}$	[95]
$O_4^- + O_4^+ \rightarrow O_2 + O_2 + O_2 + O_2$	$1.0 \cdot 10^{-7}$	[95]
$O^- + O^+ + M \rightarrow O + O + M$	$2.0 \cdot 10^{-25}(300/T)^{2.5}$	[95]
$O^- + O_2^+ + M \rightarrow O + O_2 + M$	$2.0 \cdot 10^{-25}(300/T)^{2.5}$	[95]
$O_2^- + O^+ + M \rightarrow O_2 + O + M$	$2.0 \cdot 10^{-25}(300/T)^{2.5}$	[95]
$O_2^- + O_2^+ + M \rightarrow O_2 + O_2 + M$	$2.0 \cdot 10^{-25}(300/T)^{2.5}$	[95]
$O^- + O^+ + M \rightarrow O_2 + M$	$2.0 \cdot 10^{-25}(300/T)^{2.5}$	[95]
$O^- + O_2^+ + M \rightarrow O_3 + M$	$2.0 \cdot 10^{-25}(300/T)^{2.5}$	[95]
$O_2^- + O^+ + M \rightarrow O_3 + M$	$2.0 \cdot 10^{-25}(300/T)^{2.5}$	[95]

Spontaneous emission	(s^{-1})	
$O_2(a^1) \rightarrow O_2$	$2.6 \cdot 10^{-4}$	[25]
$O_2(b^1) \rightarrow O_2(a^1)$	$1.5 \cdot 10^{-3}$	[25]
$O_2(b^1) \rightarrow O_2$	$8.5 \cdot 10^{-2}$	[25]
$O_2(4.5eV) \rightarrow O_2$	11.0	[25]

Surface reactions	Recombination factor (s^{-1})	
$O_4^+ \rightarrow 2\,O_2$	$\gamma = 1$	
$O_2^+ \rightarrow O_2$	$\gamma = 1$	
$O^+ \rightarrow O$	$\gamma = 1$	
$O_2(a^1) \rightarrow O_2$	$\gamma = 10^{-5}$	[25]
$O_2(b^1) \rightarrow O_2$	$\gamma = 10^{-2}$	[25]

$O(_1D) \rightarrow O$	$\gamma = 1$	
$O(_1S) \rightarrow O$	$\gamma = 1$	
$2\,O \rightarrow O_2$	$\gamma = 2.0 \cdot 10^{-4}$	[93]
Exhaust Coefficients		
$\alpha(O_4^+) = 7.45$	$\beta(O_4^+) = 0.54$	
$\alpha(O_2^+) = 7.45$	$\beta(O_2^+) = 0.54$	
$\alpha(O^+) = 6.72$	$\beta(O^+) = 0.60$	

1. T and $T_e(K)$ are expressed both in K.
2. Excited states not tracked as distinct species: (*v) vibrational.
3. $O_2(4.5eV)$ Generic excited state representative of $A^3\Sigma$, $C^3\Delta$, $c^1\Sigma$ states.
4. M is third body reaction partner M = O_2.

TABLE A.5: N_2O model reactions dataset.

Reaction	Rate Constant 2nd order (cm^3/s) 3rd order (cm^6/s)	Reference
$e + N_2O \rightarrow e + N_2O(^*v)$	Bolsig	[96]
$e + N_2O \rightarrow e + N_2O^*$	Bolsig	[96]
$e + N_2O \rightarrow e + e + N_2O^+$	Bolsig	[96]
$e + N_2O \rightarrow e + N_2 + O(_1D)$	Bolsig	[97]
$e + N_2O \rightarrow e + N_2 + O$	Bolsig	[97]
$e + N_2O \rightarrow e + N + NO$	Bolsig	[97]
$e + N_2 \rightarrow e + N_2(v^*)$	Bolsig	[43, 89]
$e + N_2 \rightarrow e + N_2^*$	Bolsig	[43, 89]
$e + N_2 \rightarrow e + N + N(_2D)$	Bolsig	[43, 89]
$e + N_2 \rightarrow e + e + N_2^+$	Bolsig	[43, 89]
$e + O_2 \rightarrow e + O_2(^*v)$	Bolsig	[43, 94]
$e + O_2 \rightarrow e + O_2^*$	Bolsig	[43, 94]
$e + O_2 \rightarrow e + O + O$	Bolsig	[43, 94]
$e + O_2 \rightarrow e + O + O(_1D)$	Bolsig	[43, 94]
$e + O_2 \rightarrow e + O + O^*$	Bolsig	[43, 94]
$e + O_2 \rightarrow e + e + O_2^+$	Bolsig	[43, 94]
$e + O \rightarrow e + O(_1D)$	Bolsig	[43, 94]
$e + O \rightarrow e + O^*$	Bolsig	[43, 94]
$e + O \rightarrow e + e + O^+$	Bolsig	[43, 94]
$e + NO \rightarrow e + NO(^*v)$	Bolsig	[43]
$e + NO \rightarrow e + NO^*$	Bolsig	[43]
$e + NO \rightarrow e + e + NO^+$	Bolsig	[43]
$e + N_2O^+ \rightarrow N_2 + O$	$2.0 \cdot 10^{-7}(300/T_e(K))^{0.5}$	[95]
$e + N_2^+ \rightarrow N + N$	$0.50[1.8 \cdot 10^{-7}(300/T_e(K))^{0.39}$	[25]
$e + N_2^+ \rightarrow N + N(_2D)$	$0.45[1.8 \cdot 10^{-7}(300/T_e(K))^{0.39}$	[25]
$e + O_2^+ \rightarrow O + O$	$0.55[2.7 \cdot 10^{-7}(300/T_e(K))^{0.7}]$	[25]
$e + O_2^+ \rightarrow O + O(_1D)$	$0.4[2.7 \cdot 10^{-7}(300/T_e(K))^{0.7}]$	[25]
$e + O_2^+ \rightarrow O + O^*$	$0.05[2.7 \cdot 10^{-7}(300/T_e(K))^{0.7}]$	[25]
$e + O^+ + e \rightarrow O + e$	$7.0 \cdot 10^{-20}(300/T_e(K))^{4.5}$	[25]
$e + O^+ + M \rightarrow O + M$	$6.0 \cdot 10^{-27}(300/T_e(K))^{1.5}$	[25]
$e + NO^+ \rightarrow O + N$	$0.2[4.2 \cdot 10^{-7}(300/T_e(K))^{0.85}]$	[25]
$e + NO^+ \rightarrow O + N(_2D)$	$0.8[4.2 \cdot 10^{-7}(300/T_e(K))^{0.85}]$	[25]
$N(_2D) + N_2 \rightarrow N + N_2$	$1.0 \cdot 10^{-13}\exp(-510/T)$	[25]
$O(_1D) + O \rightarrow O + O$	$8.0 \cdot 10^{-12}$	[25]
$O(_1D) + O_2 \rightarrow O + O_2$	$6.4 \cdot 10^{-12}\exp(67/T)$	[25]
$N(_2D) + O \rightarrow N + O(_1D)$	4.0^{-13}	[25]
$N(_2D) + O_2 \rightarrow NO + O$	5.2^{-12}	[25]
$N(_2D) + NO \rightarrow N_2 + O$	1.8^{-10}	[25]
$O(_1D) + N_2 \rightarrow O + N_2$	2.3^{-11}	[25]
$O(_1D) + NO \rightarrow O_2 + N$	1.7^{-10}	[25]

$N(_2D) + N_2O \rightarrow NO + N_2$	3.5^{-12}	[25]
$O(_1D) + N_2O \rightarrow NO + NO$	7.2^{-11}	[25]
$O(_1D) + N_2O \rightarrow O_2 + N_2$	4.4^{-11}	[25]
$N_2O + O \rightarrow N_2 + O_2$	$8.3 \cdot 10^{-12} \exp(-14000/T)$	[25]
$N_2O + O \rightarrow NO + NO$	$1.5 \cdot 10^{-10} \exp(-14090/T)$	[25]
$N_2O + N_2 \rightarrow N_2 + O + N_2$	$1.0[1.2 \cdot 10^{-8}(300/T) \exp(-29000/T)]$	[25]
$N_2O + O_2 \rightarrow N_2 + O + O_2$	$1.0[1.2 \cdot 10^{-8}(300/T) \exp(-29000/T)]$	[25]
$N_2O + NO \rightarrow N_2 + O + NO$	$2.0[1.2 \cdot 10^{-8}(300/T) \exp(-29000/T)]$	[25]
$N_2O + N_2O \rightarrow N_2 + O + N_2O$	$4.0[1.2 \cdot 10^{-8}(300/T) \exp(-29000/T)]$	[25]
$N_2 + M \rightarrow N + N + M$	$5.4 \cdot 10^{-8}(1 - \exp(-3354/T)) \exp(-113200/T)$	[25]
$N_2 + NO \rightarrow N + N + NO$	$5.4 \cdot 10^{-8}(1 - \exp(-3354/T)) \exp(-113200/T)$	[25]
$N_2 + N \rightarrow N + N + N$	$6.6[5.4 \cdot 10^{-8}(1 - \exp(-3354/T)) \exp(-113200/T)]$	[25]
$N_2 + O \rightarrow N + N + O$	$6.6[5.4 \cdot 10^{-8}(1 - \exp(-3354/T)) \exp(-113200/T)]$	[25]
$N + N + N_2 \rightarrow N_2 + N_2$	$MAX(8.3 \cdot 10^{-34} \exp(500/T), 1.91 \cdot 10^{-33})$	[25]
$N + N + N \rightarrow N_2 + N$	$3.0[1.8 \cdot 10^{-33} \exp(435/T)]$	[25]
$O_2 + N_2 \rightarrow O + O + N_2$	$6.1 \cdot 10^{-9}(1 - \exp(-2240/T)) \exp(-59380/T)$	[25]
$O_2 + O_2 \rightarrow O + O + O_2$	$5.9[6.1 \cdot 10^{-9}(1 - \exp(-2240/T)) \exp(-59380/T)$	[25]
$O_2 + O \rightarrow O + O + O$	$21.0[6.1 \cdot 10^{-9}(1 - \exp(-2240/T)) \exp(-59380/T)$	[25]
$O_2 + NO \rightarrow O + O + NO$	$[6.1 \cdot 10^{-9}(1 - \exp(-2240/T)) \exp(-59380/T)$	[25]
$O_2 + N \rightarrow O + O + N$	$[6.1 \cdot 10^{-9}(1 - \exp(-2240/T)) \exp(-59380/T)$	[25]
$O + O + O_2 \rightarrow O_2 + O_2$	$4.0 \cdot 10^{-33}(300/T)^{0.41}$	[25]
$O + O + O \rightarrow O_2 + O$	$3.6[4.0 \cdot 10^{-33}(300/T)^{0.41}]$	[25]
$N + O_2 \rightarrow O + NO$	$3.2 \cdot 10^{-12}(T/300) \exp(-3150/T)$	[25]
$O + N_2 \rightarrow N + NO$	$3.0 \cdot 10^{-10} \exp(-38370/T)$	[25]
$N_2 + O \rightarrow N + N + O$	$5.6[5.4 \cdot 10^{-8}(1 - \exp(-3354/T)) \exp(-113200/T)$	[25]
$N + N + O_2 \rightarrow N_2 + O_2$	$1.8 \cdot 10^{-33} \exp(435/T)$	[25]
$N + N + NO \rightarrow N_2 + NO$	$1.8 \cdot 10^{-33} \exp(435/T)$	[25]
$N + N + O \rightarrow N_2 + O$	$3.0[1.8 \cdot 10^{-33} \exp(435/T)$	[25]
$O + O + N_2 \rightarrow O_2 + N_2$	$MAX(2.8 \cdot 10^{-34} \exp(720/T), 1.0 \cdot 10^{-33}(300/T)^{0.41})$	[25]
$O + O + NO \rightarrow O_2 + NO$	$0.17[4.0 \cdot 10^{-33}(300/T)^{0.41}$	[25]
$O + O + N \rightarrow O_2 + N$	$0.8[4.0 \cdot 10^{-33}(300/T)^{0.41}$	[25]
$N + O + N_2 \rightarrow NO + N_2$	$1.0 \cdot 10^{-32}(300/T)^{0.5}$	[25]
$N + O + O_2 \rightarrow NO + O_2$	$1.0 \cdot 10^{-32}(300/T)^{0.5}$	[25]
$N + O + NO \rightarrow NO + NO$	$1.8 \cdot 10^{-31}(300/T)$	[25]
$N + O + N \rightarrow NO + N$	$1.8 \cdot 10^{-31}(300/T)$	[25]
$N + O + O \rightarrow NO + O$	$1.8 \cdot 10^{-31}(300/T)$	[25]
$N_2 + O_2 \rightarrow O + N_2O$	$2.5 \cdot 10^{-10} \exp(-50390/T)$	[25]
$O + N_2 + M_1 \rightarrow N_2O + M_1$	$3.9 \cdot 10^{-35} \exp(-10400/T)$	[25]
$NO + N \rightarrow O + N_2$	$1.8 \cdot 10^{-11}(T/300.0)^{0.5}$	[25]
$NO + O \rightarrow N + O_2$	$7.5 \cdot 10^{-12}(T/300.0) \exp(-19500/T)$	[25]
$NO + NO \rightarrow N_2 + O_2$	$5.1 \cdot 10^{-13} \exp(-33660/T)$	[25]
$NO + M_1 \rightarrow N + O + M_1$	$8.7 \cdot 10^{-9} \exp(-75994/T)$	[25]
$NO + N \rightarrow N + O + N$	$19[8.7 \cdot 10^{-9} \exp(-75994/T)]$	[25]
$NO + O \rightarrow N + O + O$	$19[8.7 \cdot 10^{-9} \exp(-75994/T)]$	[25]
$NO + NO \rightarrow O + N_2O$	$2.2 \cdot 10^{-12} \exp(-32100/T)$	[25]
$N_2O^+ + NO \rightarrow NO^+ + N_2O$	$2.9 \cdot 10^{-10}$	[25]

$N_2^+ + O_2 \rightarrow O_2^+ + N_2$	$6.0 \cdot 10^{-11}(300/T)^{0.5}$	[25]
$N_2^+ + O \rightarrow NO^+ + N$	$1.3 \cdot 10^{-10}(300/T)^{0.5}$	[25]
$N_2^+ + O \rightarrow O^+ + N_2$	$1.0 \cdot 10^{-11}(300/T)^{0.2}$	[95]
$N_2^+ + NO \rightarrow NO^+ + N_2$	$3.3 \cdot 10^{-10}$	[95]
$N_2^+ + N_2O \rightarrow N_2O^+ + N_2$	$5.0 \cdot 10^{-10}$	[95]
$N_2^+ + N_2O \rightarrow NO^+ + N + N_2$	$4.0 \cdot 10^{-10}$	[95]
$O_2^+ + N_2 \rightarrow NO^+ + NO$	$1.0 \cdot 10^{-17}$	[95]
$O_2^+ + N \rightarrow NO^+ + O$	$1.2 \cdot 10^{-10}$	[95]
$O_2^+ + NO \rightarrow NO^+ + O_2$	$6.3 \cdot 10^{-10}$	[95]
$O^+ + O_2 \rightarrow O_2^+ + O$	$2.0 \cdot 10^{-11}(300/T)^{0.5}$	[25]
$O^+ + O + M \rightarrow O_2^+ + M$	$1.0 \cdot 10^{-29}$	[25]
$O^+ + N_2 \rightarrow NO^+ + N$	$1.0 \cdot 10^{-12}[1.5 - 2.0 \cdot 10^{-3}T + 9.6 \cdot 10^{-7}T^2]$	[25]
$O^+ + NO \rightarrow NO^+ + O$	$2.4 \cdot 10^{-11}$	[25]
$O^+ + NO \rightarrow O_2^+ + N$	$3.0 \cdot 10^{-12}$	[25]
$O^+ + N_2 + M \rightarrow NO^+ + N + M$	$6.0 \cdot 10^{-29}(300/T)^2$	[95]
$O^+ + N + M \rightarrow NO^+ + M$	$1.0 \cdot 10^{-29}$	[95]
$O^+ + N_2O \rightarrow NO^+ + NO$	$2.3 \cdot 10^{-10}$	[95]
$O^+ + N_2O \rightarrow N_2O^+ + O$	$2.2 \cdot 10^{-10}$	[95]
$O^+ + N_2O \rightarrow O_2^+ + N_2$	$2.0 \cdot 10^{-11}$	[95]
$N + N \rightarrow N_2^+ + e$	$2.7 \cdot 10^{-11} \exp(-6.74 \cdot 10^4/T)$	[25]

Surface reactions	Recombination factor (s^{-1})	
$N_2^+ \rightarrow N_2$	$\gamma = 1$	
$O_2^+ \rightarrow O_2$	$\gamma = 1$	
$O^+ \rightarrow O$	$\gamma = 1$	
$NO^+ \rightarrow NO$	$\gamma = 1$	
$N_2O^+ \rightarrow N_2O$	$\gamma = 1$	
$O(_1D) \rightarrow O$	$\gamma = 1$	
$N(_2D) \rightarrow N$	$\gamma = 1$	
$2\,O \rightarrow O_2$	$\gamma = 2.0 \cdot 10^{-4}$	[93]
$2\,N \rightarrow N_2$	$\gamma = 8.0 \cdot 10^{-4}$	[93]

Exhaust Coefficients	
$\alpha(N_2O^+) = 7.75$	$\beta(N_2O^+) = 0.56$
$\alpha(N_2^+) = 7.23$	$\beta(N_2^+) = 0.55$
$\alpha(O_2^+) = 7.45$	$\beta(O_2^+) = 0.54$
$\alpha(NO^+) = 7.39$	$\beta(NO^+) = 0.56$
$\alpha(O^+) = 6.72$	$\beta(O^+) = 0.60$

1. T and $T_e(K)$ are expressed both in K.
2. Excited states not tracked as distinct species: electronic (*), (*v) vibrational.
3. M is third body reaction partner M = N_2, O_2.
4. M_1 is third body reaction partner M_1 = *any neutral particle*.

TABLE A.6: CO_2 model reactions dataset.

Reaction	Rate Constant 2nd order (cm^3/s) 3rd order (cm^6/s)	Reference
$e + CO_2 \rightarrow e + CO_2(^*v)$	Bolsig	[43, 51]
$e + CO_2 \rightarrow e + CO_2^*$	Bolsig	[43, 51]
$e + CO_2 \rightarrow e + e + CO_2^+$	Bolsig	[43, 51]
$e + CO_2 \rightarrow e + e + O + CO^+$	Bolsig	[54]
$e + CO_2 \rightarrow e + e + O_2 + C^+$	Bolsig	[54]
$e + CO_2 \rightarrow e + e + CO + O^+$	Bolsig	[54]
$e + CO \rightarrow e + CO(^*v)$	Bolsig	[43, 98]
$e + CO \rightarrow e + CO^*$	Bolsig	[43, 52]
$e + CO \rightarrow e + C + O$	Bolsig	[43, 98]
$e + CO \rightarrow e + e + CO^+$	Bolsig	[43, 98]
$e + CO \rightarrow e + C + O^+$	Bolsig	[43, 52]
$e + CO \rightarrow e + O + C^+$	Bolsig	[43, 52]
$e + O_2 \rightarrow e + O_2(^*v)$	Bolsig	[43, 94]
$e + O_2 \rightarrow e + O_2(a^1)$	Bolsig	[43, 94]
$e + O_2 \rightarrow e + O_2(b^1)$	Bolsig	[43, 94]
$e + O_2 \rightarrow e + O_2(4.5eV)$	Bolsig	[43, 94]
$e + O_2 \rightarrow e + O + O$	Bolsig	[43, 94]
$e + O_2 \rightarrow e + O + O(_1D)$	Bolsig	[43, 94]
$e + O_2 \rightarrow e + O + O(_1S)$	Bolsig	[43, 94]
$e + O_2 \rightarrow e + e + O_2^+$	Bolsig	[43, 94]
$e + O_2(a^1) \rightarrow e + O + O$	Bolsig	[43, 94]
$e + O_2(a^1) \rightarrow e + e + O_2^+$	Bolsig	[43, 94]
$e + O_2(b^1) \rightarrow e + e + O_2^+$	Bolsig	[43, 94]
$e + O_2(4.5eV) \rightarrow e + e + O_2^+$	Bolsig	[43, 94]
$e + O \rightarrow e + O(_1D)$	Bolsig	[43, 94]
$e + O \rightarrow e + O(_1S)$	Bolsig	[43, 94]
$e + O \rightarrow e + e + O^+$	Bolsig	[43, 94]
$e + O_2^+ \rightarrow O + O$	$0.55[2.7 \cdot 10^{-7}(300/T_e(K))^{0.7}]$	[25]
$e + O_2^+ \rightarrow O + O(_1D)$	$0.4[2.7 \cdot 10^{-7}(300/T_e(K))^{0.7}]$	[25]
$e + O_2^+ \rightarrow O + O(_1S)$	$0.05[2.7 \cdot 10^{-7}(300/T_e(K))^{0.7}]$	[25]
$e + O_4^+ \rightarrow O_2 + O_2$	$1.4 \cdot 10^{-6}(300/T_e(K))^{0.5}$	[25]
$e + O^+ + e \rightarrow O + e$	$7.0 \cdot 10^{-20}(300/T_e(K))^{4.5}$	[25]
$e + O^+ + M \rightarrow O + M$	$6.0 \cdot 10^{-27}(300/T_e(K))^{1.5}$	[25]
$e + CO_2 \rightarrow CO + O^-$	Bolsig	[54]
$e + O_2 \rightarrow O^- + O$	Bolsig	[43, 94]
$e + O_3 \rightarrow O_2^- + O$	$1.0 \cdot 10^{-9}$	[25]
$e + O_3 \rightarrow O^- + O_2$	$1.0 \cdot 10^{-11}$	[25]
$e + O + O_2 \rightarrow O^- + O_2$	$1.0 \cdot 10^{-31}$	[25]
$e + O + O_2 \rightarrow O_2^- + O$	$1.0 \cdot 10^{-31}$	[25]
$e + O_3 + O_2 \rightarrow O_3^- + O_2$	$1.0 \cdot 10^{-31}$	[25]
$e + O_2 + O_2 \rightarrow O_2^- + O_2$	$1.4 \cdot 10^{-29}(300/T_e(K))\exp(-600/T)$	[95]

$O^- + O \rightarrow O_2 + e$	$1.4 \cdot 10^{-10}$	[25]
$O^- + O_2 \rightarrow O_3 + e$	$5.0 \cdot 10^{-15}$	[25]
$O^- + O_2(a^1) \rightarrow O_3 + e$	$3.0 \cdot 10^{-10}$	[25]
$O^- + O_2(b^1) \rightarrow O + O_2 + e$	$6.9 \cdot 10^{-10}$	[25]
$O^- + O_3 \rightarrow O_2 + O_2 + e$	$3.0 \cdot 10^{-10}$	[25]
$O_2^- + O \rightarrow O_3 + e$	$1.5 \cdot 10^{-10}$	[25]
$O_2^- + O_2 \rightarrow O_2 + O_2 + e$	$2.7 \cdot 10^{-10}(T/300)^{0.5} \exp(-5590/T)$	[25]
$O_2^- + O_2(a^1) \rightarrow O_2 + O_2 + e$	$2.0 \cdot 10^{-10}$	[25]
$O_2^- + O_2(b^1) \rightarrow O_2 + O_2 + e$	$3.6 \cdot 10^{-10}$	[25]
$O_3^- + O \rightarrow O_2 + O_2 + e$	$3.0 \cdot 10^{-10}$	[25]
$O_2(a^1) + O \rightarrow O_2 + O$	$7.0 \cdot 10^{-16}$	[25]
$O_2(a^1) + O_2 \rightarrow O_2 + O_2$	$3.8 \cdot 10^{-18} \exp(-205/T)$	[25]
$O_2(a^1) + O_3 \rightarrow O_2 + O_2 + O(_1D)$	$5.2 \cdot 10^{-11} \exp(-2840/T)$	[25]
$O_2(a^1) + O_2(a^1) \rightarrow O_2 + O_2(b^1)$	$7.0 \cdot 10^{-28} T^{3.8} \exp(700/T)$	[25]
$O + O_3 \rightarrow O_2 + O_2(a^1)$	$1.0 \cdot 10^{-11} \exp(-2300/T)$	[25]
$O_2(b^1) + O \rightarrow O_2(a^1) + O$	$8.1 \cdot 10^{-14}$	[25]
$O_2(b^1) + O \rightarrow O_2 + O(_1D)$	$3.4 \cdot 10^{-11}(300/T)^{0.1} \exp(-4200/T)$	[25]
$O_2(b^1) + O_2 \rightarrow O_2(a^1) + O_2$	$4.3 \cdot 10^{-22} T^{2.4} \exp(-281/T)$	[25]
$O_2(b^1) + O_3 \rightarrow O_2 + O_2 + O$	$2.2 \cdot 10^{-11}$	[25]
$O_2(4.5eV) + O \rightarrow O_2 + O(_1S)$	$9.0 \cdot 10^{-12}$	[25]
$O + O + M \rightarrow O_2(a^1) + M$	$0.07[6.1 \cdot 10^{-9}(1 - \exp(-2240/T)) \exp(-59380/T)]$	[25]
$O + O + O_2 \rightarrow O_2(a^1) + O_2$	$0.343[6.1 \cdot 10^{-9}(1 - \exp(-2240/T)) \exp(-59380/T)]$	[25]
$O + O + O \rightarrow O_2(a^1) + O$	$1.4[6.1 \cdot 10^{-9}(1 - \exp(-2240/T)) \exp(-59380/T)]$	[25]
$O + O + M \rightarrow O_2(b^1) + M$	$0.01[6.1 \cdot 10^{-9}(1 - \exp(-2240/T)) \exp(-59380/T)]$	[25]
$O_2(a^1) + O_2(a^1) + O_2 \rightarrow O_3 + O_3$	$1.0 \cdot 10^{-31}$	[25]
$O(_1D) + O \rightarrow O + O$	$8.0 \cdot 10^{-12}$	[25]
$O(_1D) + O_2 \rightarrow O + O_2$	$6.4 \cdot 10^{-12} \exp(67/T)$	[25]
$O(_1D) + O_2 \rightarrow O + O_2(a^1)$	$1.0 \cdot 10^{-12}$	[25]
$O(_1D) + O_2 \rightarrow O + O_2(b^1)$	$2.6 \cdot 10^{-11} \exp(67/T)$	[25]
$O(_1D) + O_3 \rightarrow O_2 + O + O$	$1.2 \cdot 10^{-10}$	[25]
$O(_1D) + O_3 \rightarrow O_2 + O_2$	$1.2 \cdot 10^{-10}$	[25]
$O(_1S) + O \rightarrow O(_1D) + O$	$5.0 \cdot 10^{-11} \exp(-300/T)$	[95]
$O(_1S) + O_2 \rightarrow O(_1D) + O_2$	$1.3 \cdot 10^{-12} \exp(-850/T)$	[95]
$O(_1S) + O_2 \rightarrow O + O + O$	$3.0 \cdot 10^{-12} \exp(-850/T)$	[95]
$O(_1S) + O_2(a^1) \rightarrow O + O + O$	$1.1 \cdot 10^{-10}$	[95]
$O(_1S) + O_2(a^1) \rightarrow O(_1D) + O_2(b^1)$	$2.9 \cdot 10^{-11}$	[95]
$O(_1S) + O_2(a^1) \rightarrow O + O + O$	$3.2 \cdot 10^{-11}$	[95]
$O(_1S) + O_3 \rightarrow O_2 + O_2$	$2.9 \cdot 10^{-10}$	[95]
$O(_1S) + O_3 \rightarrow O_2 + O + O(_1D)$	$2.9 \cdot 10^{-10}$	[95]
$CO_2 + CO_2 \rightarrow CO + O + CO_2$	$2.14 \cdot 10^{-10}(T/298)^{0}.5 \exp(-52321/T)$	[55]
$CO_2 + CO \rightarrow CO + O + CO$	$1.53 \cdot 10^{-8}(T/298)^{0}.5 \exp(-40053/T)$	[55]
$CO_2 + O_2 \rightarrow CO + O + O_2$	$1.53 \cdot 10^{-8}(T/298)^{0}.5 \exp(-40053/T)$	[55]
$CO + O + CO_2 \rightarrow CO_2 + CO_2$	$6.51 \cdot 10^{-36} \exp(1859/Tgas)$	[55]
$CO + O + CO \rightarrow CO_2 + CO$	$1.46 \cdot 10^{-34} \exp(2280/Tgas)$	[55]
$CO + O + O_2 \rightarrow CO_2 + O_2$	$1.17 \cdot 10^{-33} \exp(-1509/Tgas)$	[55]
$CO_2 + O \rightarrow CO + O_2$	$2.81 \cdot 10^{-11} \exp(-26461/Tgas)$	[55]
$CO + O_2 \rightarrow CO_2 + O$	$4.20 \cdot 10^{-12} \exp(-24056/Tgas)$	[55]

$O + O_3 \rightarrow O_2 + O_2(a^1)$	$2.0 \cdot 10^{-11} \exp(-2280/T)$	[25]
$O_2 + O_2 \rightarrow O + O_3$	$2.0 \cdot 10^{-11} \exp(-49800/T)$	[25]
$O_2 + M \rightarrow O + O + M$	$6.1 \cdot 10^{-9}(1 - \exp(-2240/T)) \exp(-59380/T)$	[25]
$O_2 + O_2 \rightarrow O + O + O_2$	$4.9[6.1 \cdot 10^{-9}(1 - \exp(-2240/T)) \exp(-59380/T)$	[25]
$O_2 + O \rightarrow O + O + O$	$20.0[6.1 \cdot 10^{-9}(1 - \exp(-2240/T)) \exp(-59380/T)$	[25]
$O_3 + O_2 \rightarrow O_2 + O + O_2$	$0.38[6.6 \cdot 10^{-10} \exp(-11600/T)]$	[25]
$O_3 + O \rightarrow O_2 + O + O$	$6.3[6.6 \cdot 10^{-10} \exp(-11600/T) \exp(170/T)]$	[25]
$O + O + O_2 \rightarrow O_2 + O_2$	$4.0 \cdot 10^{-33}(300/T)^{0.41}$	[25]
$O + O + O \rightarrow O_2 + O$	$3.6[4.0 \cdot 10^{-33}(300/T)^{0.41}]$	[25]
$O + O_2 + O_2 \rightarrow O_3 + O_2$	$7.6 \cdot 10^{-34}(300/T)^{1.9}$	[25]
$O + O_2 + O \rightarrow O_3 + O$	$min[3.9 \cdot 10^{-33}(300/T)^{1.9}, 1.1 \cdot 10^{-34} \exp(1060/T)]$	[25]
$O^+ + O_2 \rightarrow O_2^+ + O$	$2.0 \cdot 10^{-11}(300/T)^{0.5}$	[25]
$O^+ + O_3 \rightarrow O_2^+ + O_2$	$1.0 \cdot 10^{-10}$	[25]
$O_4^+ + O_2 \rightarrow O_2^+ + O_2 + O_2$	$3.3 \cdot 10^{-6}(300/T)^{4.0} \exp(-5030/T)$	[25]
$O_4^+ + O_2(a^1) \rightarrow O_2^+ + O_2 + O_2$	$1.0 \cdot 10^{-10}$	[25]
$O_4^+ + O_2(b^1) \rightarrow O_2^+ + O_2 + O_2$	$1.0 \cdot 10^{-10}$	[25]
$O_4^+ + O \rightarrow O_2^+ + O_3$	$3.0 \cdot 10^{-10}$	[25]
$O^+ + O + M \rightarrow O_2^+ + M$	$1.0 \cdot 10^{-29}$	[25]
$O_2^+ + O_2 + O_2 \rightarrow O_4^+ + O_2$	$2.4 \cdot 10^{-30}(300/T)^{3.2}$	[25]
$O^- + O_2(a^1) \rightarrow O_2^- + O$	$1.0 \cdot 10^{-10}$	[25]
$O^- + O_3 \rightarrow O_3^- + O$	$8.0 \cdot 10^{-10}$	[25]
$O_2^- + O \rightarrow O^- + O_2$	$3.3 \cdot 10^{-10}$	[25]
$O_2^- + O_3 \rightarrow O_3^- + O_2$	$3.5 \cdot 10^{-10}$	[25]
$O_3^- + O \rightarrow O_2^- + O_2$	$3.2 \cdot 10^{-10}$	[95]
$O_4^- + M \rightarrow O_2^- + O_2 + M$	$1.0 \cdot 10^{-10} \exp(-1044/T)$	[95]
$O_4^- + O \rightarrow O_3^- + O_2$	$4.0 \cdot 10^{-10}$	[95]
$O_4^- + O \rightarrow O^- + O_2 + O_2$	$3.0 \cdot 10^{-10}$	[95]
$O_4^- + O_2(a^1) \rightarrow O_2^- + O_2 + O_2$	$1.0 \cdot 10^{-10}$	[95]
$O_4^- + O_2(b^1) \rightarrow O_2^- + O_2 + O_2$	$1.0 \cdot 10^{-10}$	[95]
$O^- + O_2 + M \rightarrow O_3^- + M$	$1.1 \cdot 10^{-30}(300/T)$	[95]
$O_2^- + O_2 + M \rightarrow O_4^- + M$	$3.5 \cdot 10^{-31}(300/T)$	[95]
$O^- + O^+ \rightarrow O + O$	$2.0 \cdot 10^{-7}(300/T)^{0.5}$	[95]
$O^- + O_2^+ \rightarrow O + O_2$	$2.0 \cdot 10^{-7}(300/T)^{0.5}$	[95]
$O^- + O_2^+ \rightarrow O + O + O$	$1.0 \cdot 10^{-7}$	[95]
$O^- + O_4^+ \rightarrow O + O_2 + O_2$	$1.0 \cdot 10^{-7}$	[95]
$O_2^- + O^+ \rightarrow O_2 + O$	$2.0 \cdot 10^{-7}(300/T)^{0.5}$	[95]
$O_2^- + O_2^+ \rightarrow O_2 + O_2$	$2.0 \cdot 10^{-7}(300/T)^{0.5}$	[95]
$O_2^- + O_2^+ \rightarrow O_2 + O + O$	$1.0 \cdot 10^{-7}$	[95]
$O_2^- + O_4^+ \rightarrow O_2 + O_2 + O_2$	$1.0 \cdot 10^{-7}$	[95]
$O_3^- + O^+ \rightarrow O_3 + O$	$2.0 \cdot 10^{-7}(300/T)^{0.5}$	[95]
$O_3^- + O_2^+ \rightarrow O_3 + O_2$	$2.0 \cdot 10^{-7}(300/T)^{0.5}$	[95]
$O_3^- + O_2^+ \rightarrow O_3 + O + O$	$1.0 \cdot 10^{-7}$	[95]
$O_3^- + O_4^+ \rightarrow O_3 + O_2 + O_2$	$1.0 \cdot 10^{-7}$	[95]
$O_4^- + O^+ \rightarrow O_2 + O_2 + O$	$1.0 \cdot 10^{-7}$	[95]
$O_4^- + O_2^+ \rightarrow O_2 + O_2 + O_2$	$1.0 \cdot 10^{-7}$	[95]
$O_4^- + O_4^+ \rightarrow O_2 + O_2 + O_2 + O_2$	$1.0 \cdot 10^{-7}$	[95]

$O^- + O^+ + M \rightarrow O + O + M$	$2.0 \cdot 10^{-25}(300/T)^{2.5}$	[95]
$O^- + O_2^+ + M \rightarrow O + O_2 + M$	$2.0 \cdot 10^{-25}(300/T)^{2.5}$	[95]
$O_2^- + O^+ + M \rightarrow O_2 + O + M$	$2.0 \cdot 10^{-25}(300/T)^{2.5}$	[95]
$O_2^- + O_2^+ + M \rightarrow O_2 + O_2 + M$	$2.0 \cdot 10^{-25}(300/T)^{2.5}$	[95]
$O^- + O^+ + M \rightarrow O_2 + M$	$2.0 \cdot 10^{-25}(300/T)^{2.5}$	[95]
$O^- + O_2^+ + M \rightarrow O_3 + M$	$2.0 \cdot 10^{-25}(300/T)^{2.5}$	[95]
$O_2^- + O^+ + M \rightarrow O_3 + M$	$2.0 \cdot 10^{-25}(300/T)^{2.5}$	[95]

Spontaneous emission	(s^{-1})	
$O_2(a^1) \rightarrow O_2$	$2.6 \cdot 10^{-4}$	[25]
$O_2(b^1) \rightarrow O_2(a^1)$	$1.5 \cdot 10^{-3}$	[25]
$O_2(b^1) \rightarrow O_2$	$8.5 \cdot 10^{-2}$	[25]
$O_2(4.5eV) \rightarrow O_2$	11.0	[25]

Surface reactions	Recombination factor (s^{-1})	
$CO_2^+ \rightarrow CO_2$	$\gamma = 1$	
$CO^+ \rightarrow CO$	$\gamma = 1$	
$C^+ \rightarrow C$	$\gamma = 1$	
$O_4^+ \rightarrow 2\,O_2$	$\gamma = 1$	
$O_2^+ \rightarrow O_2$	$\gamma = 1$	
$O^+ \rightarrow O$	$\gamma = 1$	
$O_2(a^1) \rightarrow O_2$	$\gamma = 10^{-5}$	[25]
$O_2(b^1) \rightarrow O_2$	$\gamma = 10^{-2}$	[25]
$O(_1D) \rightarrow O$	$\gamma = 1$	
$O(_1S) \rightarrow O$	$\gamma = 1$	
$2\,O \rightarrow O_2$	$\gamma = 2.0 \cdot 10^{-4}$	[93]

Exhaust Coefficients	
$\alpha(CO_2^+) = 7.45$	$\beta(O_4^+) = 0.49$
$\alpha(CO^+) = 7.50$	$\beta(O_4^+) = 0.53$
$\alpha(C^+) = 7.53$	$\beta(O_4^+) = 0.60$
$\alpha(O_4^+) = 7.45$	$\beta(O_4^+) = 0.54$
$\alpha(O_2^+) = 7.45$	$\beta(O_2^+) = 0.54$
$\alpha(O^+) = 6.72$	$\beta(O^+) = 0.60$

1. T and $T_e(K)$ are expressed both in K.
2. Excited states not tracked as distinct species: electronic (*), (*v) vibrational.
3. $O_2(4.5eV)$ Generic excited state representative of $A^3\Sigma$, $C^3\Delta$, $c^1\Sigma$ states.
4. M is third body reaction partner M = O_2.

CO_2 model kinetic scheme

TABLE A.7: Electron impact cross sections and rate constants for the CO_2 model.

Reaction	Rate Constant 2nd order (cm^3/s) 3rd order (cm^6/s)	Reference
$e + CO_2 \rightarrow e + CO_2(^*v)$	Integrated	[43, 51]
$e + CO_2 \rightarrow e + CO_2(e_1)$	Integrated	[43, 51]
$e + CO_2 \rightarrow e + CO_2(e_2)$	Integrated	[43, 51]
$e + CO_2 \rightarrow e + e + CO_2^+$	Integrated	[43, 51]
$e + CO_2(e_1) \rightarrow e + e + CO_2^+$	Integrated	[43, 51]
$e + CO_2(e_2) \rightarrow e + e + CO_2^+$	Integrated	[43, 51]
$e + CO_2 \rightarrow e + CO + O(_1S)$	Integrated	[54]
$e + CO_2 \rightarrow e + e + O + CO^+$	Integrated	[54]
$e + CO_2(e_1) \rightarrow e + e + O + CO^+$	Integrated	[54]
$e + CO_2(e_2) \rightarrow e + e + O + CO^+$	Integrated	[54]
$e + CO_2 \rightarrow e + e + O_2 + C^+$	Integrated	[54]
$e + CO_2(e_1) \rightarrow e + e + O_2 + C^+$	Integrated	[54]
$e + CO_2(e_2) \rightarrow e + e + O_2 + C^+$	Integrated	[54]
$e + CO_2 \rightarrow e + e + CO + O^+$	Integrated	[54]
$e + CO_2(e_1) \rightarrow e + e + CO + O^+$	Integrated	[54]
$e + CO_2(e_2) \rightarrow e + e + CO + O^+$	Integrated	[54]
$e + CO \rightarrow e + CO(^*v)$	Integrated	[43, 98]
$e + CO \rightarrow e + CO(A^1)$	Integrated	[43, 52]
$e + CO \rightarrow e + CO(a^3)$	Integrated	[43, 52]
$e + CO \rightarrow e + CO(e_1)$	Integrated	[43, 52]
$e + CO \rightarrow e + CO(e_2)$	Integrated	[43, 52]
$e + CO \rightarrow e + C + O$	Integrated	[43, 98]
$e + CO \rightarrow e + e + CO^+$	Integrated	[43, 98]
$e + CO(A^1) \rightarrow e + e + CO^+$	Integrated	[43, 98]
$e + CO(a^3) \rightarrow e + e + CO^+$	Integrated	[43, 98]
$e + CO(e_1) \rightarrow e + e + CO^+$	Integrated	[43, 98]
$e + CO(e_2) \rightarrow e + e + CO^+$	Integrated	[43, 98]
$e + CO \rightarrow e + C + O^+$	Integrated	[43, 52]
$e + CO(A^1) \rightarrow e + C + O^+$	Integrated	[43, 52]
$e + CO(a^3) \rightarrow e + C + O^+$	Integrated	[43, 52]
$e + CO(e_1) \rightarrow e + C + O^+$	Integrated	[43, 52]
$e + CO(e_2) \rightarrow e + C + O^+$	Integrated	[43, 52]
$e + CO \rightarrow e + O + C^+$	Integrated	[43, 52]
$e + CO(A^1) \rightarrow e + O + C^+$	Integrated	[43, 52]
$e + CO(a^3) \rightarrow e + O + C^+$	Integrated	[43, 52]
$e + CO(e_1) \rightarrow e + O + C^+$	Integrated	[43, 52]
$e + CO(e_2) \rightarrow e + O + C^+$	Integrated	[43, 52]
$e + C \rightarrow e + C^*$	Integrated	[43, 99]

$e + C \rightarrow e + e + C^+$	Integrated	[43, 99]
$e + O_2 \rightarrow e + O_2(^*v)$	Integrated	[43, 94]
$e + O_2 \rightarrow e + O_2(a^1)$	Integrated	[43, 94]
$e + O_2 \rightarrow e + O_2(b^1)$	Integrated	[43, 94]
$e + O_2 \rightarrow e + O_2(4.5eV)$	Integrated	[43, 94]
$e + O_2 \rightarrow e + O + O$	Integrated	[43, 94]
$e + O_2(a^1) \rightarrow e + O + O$	Integrated	[43, 94]
$e + O_2 \rightarrow e + O + O(_1D)$	Integrated	[43, 94]
$e + O_2 \rightarrow e + O + O(_1S)$	Integrated	[43, 94]
$e + O_2 \rightarrow e + e + O_2^+$	Integrated	[43, 94]
$e + O_2(a^1) \rightarrow e + e + O_2^+$	Integrated	[43, 94]
$e + O_2(b^1) \rightarrow e + e + O_2^+$	Integrated	[43, 94]
$e + O_2(4.5eV) \rightarrow e + e + O_2^+$	Integrated	[43, 94]
$e + O \rightarrow e + O(_1D)$	Integrated	[43, 94]
$e + O \rightarrow e + O(_1S)$	Integrated	[43, 94]
$e + O \rightarrow e + e + O^+$	Integrated	[43, 94]
$e + CO_2 \rightarrow CO + O^-$	Integrated	[54]
$e + O_2 \rightarrow O^- + O$	Integrated	[43, 94]
$e + O_3 \rightarrow O_2^- + O$	$1.0 \cdot 10^{-9}$	[25]
$e + O_3 \rightarrow O^- + O_2$	$1.0 \cdot 10^{-11}$	[25]
$e + O + O_2 \rightarrow O^- + O_2$	$1.0 \cdot 10^{-31}$	[25]
$e + O_2 + O \rightarrow O_2^- + O$	$1.0 \cdot 10^{-31}$	[25]
$e + O_3 + O_2 \rightarrow O_3^- + O_2$	$1.0 \cdot 10^{-31}$	[25]
$e + O_2 + O_2 \rightarrow O_2^- + O_2$	$1.4 \cdot 10^{-29}(300/T_e(K)) \exp(-600/T)$	[95]
$e + CO_2^+ \rightarrow CO + O$	$2.0 \cdot 10{-}5(1/T){T_e}^{-0.5)}$	[46]
$e + CO_2^+ \rightarrow C + O_2$	$5.0 \cdot 10{-}7(T_e(K)/300)^{-0.4}$	[47]
$e + CO^+ \rightarrow C + O$	$3.683 \cdot 10^{-9}{T_e}^{-0.55}$	[50]
$e + O_2^+ \rightarrow O + O$	$0.55[2.7 \cdot 10^{-7}(300/T_e(K))^{0.7}]$	[25]
$e + O_2^+ \rightarrow O + O(_1D)$	$0.4[2.7 \cdot 10^{-7}(300/T_e(K))^{0.7}]$	[25]
$e + O_2^+ \rightarrow O + O(_1S)$	$0.05[2.7 \cdot 10^{-7}(300/T_e(K))^{0.7}]$	[25]
$e + O_4^+ \rightarrow O_2 + O_2$	$1.4 \cdot 10^{-6}(300/T_e(K))^{0.5}$	[25]
$e + O^+ + e \rightarrow O + e$	$7.0 \cdot 10^{-20}(300/T_e(K))^{4.5}$	[25]
$e + O^+ + M \rightarrow O + M$	$6.0 \cdot 10^{-27}(300/T_e(K))^{1.5}$	[25]

1. T and $T_e(K)$ are in K, T_e is in eV.
2. Excited states not tracked as distinct species: (*v) vibrational.
3. $O_2(4.5eV)$ Generic excited state representative of $A^3\Sigma$, $C^3\Delta$, $c^1\Sigma$ states.
4. $CO_2(e_1)$ and $CO_2(e_2)$ corresponds to $CO_2(^1\Pi)$ and $CO_2(^1\Delta)$.
5. $CO(e_1)$ is a generic excited state representative of $CO(I^1\Sigma)$, $CO(B^1\Sigma)$, $CO(C^1\Sigma)$, $CO(E^1\Pi)$.
6. $CO(e_2)$ is a generic excited state representative of $CO(a'^3\Sigma)$, $CO(d^3\Delta)$, $CO(e^3\Sigma)$, $CO(b^3\Sigma)$.

7. M is third body reaction partner M = O_2.

TABLE A.8: Detachment, charge exchange and ion-ion reactions for the CO_2 model.

Reaction	Rate Constant 2nd order (cm^3/s) 3rd order (cm^6/s)	Reference
$O^- + CO \rightarrow CO_2 + e$	$5.5 \cdot 10^{-10}$	[47]
$O^- + C \rightarrow CO + e$	$5.0 \cdot 10^{-10}$	[100]
$O^- + O \rightarrow O_2 + e$	$1.4 \cdot 10^{-10}$	[25]
$O^- + O_2 \rightarrow O_3 + e$	$5.0 \cdot 10^{-15}$	[25]
$O^- + O_2(a^1) \rightarrow O_3 + e$	$3.0 \cdot 10^{-10}$	[25]
$O^- + O_2(b^1) \rightarrow O + O_2 + e$	$6.9 \cdot 10^{-10}$	[25]
$O^- + O_3 \rightarrow O_2 + O_2 + e$	$3.0 \cdot 10^{-10}$	[25]
$O_2^- + O \rightarrow O_3 + e$	$1.5 \cdot 10^{-10}$	[25]
$O_2^- + O_2 \rightarrow O_2 + O_2 + e$	$2.7 \cdot 10^{-10}(T/300)^{0.5} \exp(-5590/T)$	[25]
$O_2^- + O_2(a^1) \rightarrow O_2 + O_2 + e$	$2.0 \cdot 10^{-10}$	[25]
$O_2^- + O_2(b^1) \rightarrow O_2 + O_2 + e$	$3.6 \cdot 10^{-10}$	[25]
$O_3^- + O \rightarrow O_2 + O_2 + e$	$3.0 \cdot 10^{-10}$	[25]
$CO_2^+ + O \rightarrow O_2^+ + CO$	$1.64 \cdot 10^{-10}$	[100]
$CO_2^+ + O \rightarrow O^+ + CO_2$	$9.62 \cdot 10^{-11}$	[100]
$CO_2^+ + O_2 \rightarrow O_2^+ + CO_2$	$5.30 \cdot 10^{-11}$	[100]
$CO^+ + CO_2 \rightarrow CO_2^+ + CO$	$1.0 \cdot 10^{-10}$	[100]
$CO^+ + C \rightarrow CO + C^+$	$1.1 \cdot 10^{-10}$	[100]
$CO^+ + O \rightarrow O^+ + CO$	$1.4 \cdot 10^{-10}$	[100]
$CO^+ + O_2 \rightarrow O_2^+ + CO$	$1.2 \cdot 10^{-10}$	[100]
$O_2^+ + C \rightarrow CO^+ + O$	$5.2 \cdot 10^{-11}$	[100]
$O_2^+ + C \rightarrow C^+ + O_2$	$5.2 \cdot 10^{-11}$	[100]
$O_2^+ + O_2 + O_2 \rightarrow O_4^+ + O_2$	$2.4 \cdot 10^{-30}(300/T)^{3.2}$	[25]
$O^+ + CO_2 \rightarrow O_2^+ + CO$	$9.4 \cdot 10^{-11}$	[100]
$O^+ + CO_2 \rightarrow CO_2^+ + O$	$4.5 \cdot 10^{-10}$	[47]
$O^+ + CO \rightarrow O + CO^+$	$4.9 \cdot 10^{-12}(300/T)^{0.5} \exp(-4580/T)$	[100]
$O^+ + O_2 \rightarrow O_2^+ + O$	$2.0 \cdot 10^{-11}(300/T)^{0.5}$	[25]
$O^+ + O_3 \rightarrow O_2^+ + O_2$	$1.0 \cdot 10^{-10}$	[25]
$O^+ + O + M \rightarrow O_2^+ + M$	$1.0 \cdot 10^{-29}$	[25]
$O_4^+ + O_2 \rightarrow O_2^+ + O_2 + O_2$	$3.3 \cdot 10^{-6}(300/T)^{4.0} \exp(-5030/T)$	[25]
$O_4^+ + O_2(a^1) \rightarrow O_2^+ + O_2 + O_2$	$1.0 \cdot 10^{-10}$	[25]
$O_4^+ + O_2(b^1) \rightarrow O_2^+ + O_2 + O_2$	$1.0 \cdot 10^{-10}$	[25]
$O_4^+ + O \rightarrow O_2^+ + O_3$	$3.0 \cdot 10^{-10}$	[25]
$C^+ + CO_2 \rightarrow CO^+ + CO$	$1.1 \cdot 10^{-9}$	[47]
$C^+ + CO \rightarrow CO^+ + C$	$5.0 \cdot 10^{-13}$	[47]
$C^+ + O_2 \rightarrow CO + O^+$	$6.2 \cdot 10^{-10}$	[47]
$C^+ + O_2 \rightarrow CO^+ + O$	$3.8 \cdot 10^{-10}$	[47]
$O^- + O_2(a^1) \rightarrow O_2^- + O$	$1.0 \cdot 10^{-10}$	[25]
$O^- + O_3 \rightarrow O_3^- + O$	$8.0 \cdot 10^{-10}$	[25]
$O^- + O_2 + M \rightarrow O_3^- + M$	$1.1 \cdot 10^{-30}(300/T)$	[95]
$O_2^- + O \rightarrow O^- + O_2$	$3.3 \cdot 10^{-10}$	[25]

$O_2^- + O_3 \rightarrow O_3^- + O_2$	$3.5 \cdot 10^{-10}$	[25]
$O_2^- + O_2 + M \rightarrow O_4^- + M$	$3.5 \cdot 10^{-31}(300/T)$	[95]
$O_3^- + O \rightarrow O_2^- + O_2$	$3.2 \cdot 10^{-10}$	[95]
$O_4^- + M \rightarrow O_2^- + O_2 + M$	$1.0 \cdot 10^{-10} \exp(-1044/T)$	[95]
$O_4^- + O \rightarrow O_3^- + O_2$	$4.0 \cdot 10^{-10}$	[95]
$O_4^- + O \rightarrow O^- + O_2 + O_2$	$3.0 \cdot 10^{-10}$	[95]
$O_4^- + O_2(a^1) \rightarrow O_2^- + O_2 + O_2$	$1.0 \cdot 10^{-10}$	[95]
$O_4^- + O_2(b^1) \rightarrow O_2^- + O_2 + O_2$	$1.0 \cdot 10^{-10}$	[95]
$O^- + C^+ \rightarrow O + C$	$3.0 \cdot 10^{-7}$	[101]
$O^- + CO^+ \rightarrow O + CO$	$2.0 \cdot 10^{-7}$	[101]
$O^- + O^+ \rightarrow O + O$	$2.0 \cdot 10^{-7}(300/T)^{0.5}$	[95]
$O^- + O_2^+ \rightarrow O + O_2$	$2.0 \cdot 10^{-7}(300/T)^{0.5}$	[95]
$O^- + O_2^+ \rightarrow O + O + O$	$1.0 \cdot 10^{-7}$	[95]
$O^- + O_4^+ \rightarrow O + O_2 + O_2$	$1.0 \cdot 10^{-7}$	[95]
$O^- + O^+ + M \rightarrow O + O + M$	$2.0 \cdot 10^{-25}(300/T)^{2.5}$	[95]
$O^- + O_2^+ + M \rightarrow O + O_2 + M$	$2.0 \cdot 10^{-25}(300/T)^{2.5}$	[95]
$O^- + O^+ + M \rightarrow O_2 + M$	$2.0 \cdot 10^{-25}(300/T)^{2.5}$	[95]
$O^- + O_2^+ + M \rightarrow O_3 + M$	$2.0 \cdot 10^{-25}(300/T)^{2.5}$	[95]
$O_2^- + O^+ \rightarrow O_2 + O$	$2.0 \cdot 10^{-7}(300/T)^{0.5}$	[95]
$O_2^- + O_2^+ \rightarrow O_2 + O_2$	$2.0 \cdot 10^{-7}(300/T)^{0.5}$	[95]
$O_2^- + O_2^+ \rightarrow O_2 + O + O$	$1.0 \cdot 10^{-7}$	[95]
$O_2^- + O_4^+ \rightarrow O_2 + O_2 + O_2$	$1.0 \cdot 10^{-7}$	[95]
$O_2^- + O^+ + M \rightarrow O_2 + O + M$	$2.0 \cdot 10^{-25}(300/T)^{2.5}$	[95]
$O_2^- + O_2^+ + M \rightarrow O_2 + O_2 + M$	$2.0 \cdot 10^{-25}(300/T)^{2.5}$	[95]
$O_2^- + O^+ + M \rightarrow O_3 + M$	$2.0 \cdot 10^{-25}(300/T)^{2.5}$	[95]
$O_3^- + O^+ \rightarrow O_3 + O$	$2.0 \cdot 10^{-7}(300/T)^{0.5}$	[95]
$O_3^- + O_2^+ \rightarrow O_3 + O_2$	$2.0 \cdot 10^{-7}(300/T)^{0.5}$	[95]
$O_3^- + O_2^+ \rightarrow O_3 + O + O$	$1.0 \cdot 10^{-7}$	[95]
$O_3^- + O_4^+ \rightarrow O_3 + O_2 + O_2$	$1.0 \cdot 10^{-7}$	[95]
$O_4^- + O^+ \rightarrow O_2 + O_2 + O$	$1.0 \cdot 10^{-7}$	[95]
$O_4^- + O_2^+ \rightarrow O_2 + O_2 + O_2$	$1.0 \cdot 10^{-7}$	[95]
$O_4^- + O_4^+ \rightarrow O_2 + O_2 + O_2 + O_2$	$1.0 \cdot 10^{-7}$	[95]

TABLE A.9: Activation-deactivation of metastables, neutral gas phase reactions and surface reactions for the CO_2 model.

Reaction	Rate Constant 2nd order (cm^3/s) 3rd order (cm^6/s)	Reference
$O_2(a^1) + O \rightarrow O_2 + O$	$7.0 \cdot 10^{-16}$	[25]
$O_2(a^1) + O_2 \rightarrow O_2 + O_2$	$3.8 \cdot 10^{-18} \exp(-205/T)$	[25]
$O_2(a^1) + O_3 \rightarrow O_2 + O_2 + O(_1D)$	$5.2 \cdot 10^{-11} \exp(-2840/T)$	[25]
$O_2(a^1) + O_2(a^1) \rightarrow O_2 + O_2(b^1)$	$7.0 \cdot 10^{-28} T^{3.8} \exp(700/T)$	[25]
$O_2(a^1) + O_2(a^1) + O_2 \rightarrow O_3 + O_3$	$1.0 \cdot 10^{-31}$	[92]
$O_2(b^1) + O \rightarrow O_2(a^1) + O$	$8.1 \cdot 10^{-14}$	[25]
$O_2(b^1) + O \rightarrow O_2 + O(_1D)$	$3.4 \cdot 10^{-11} (300/T)^{0.1} \exp(-4200/T)$	[25]
$O_2(b^1) + O_2 \rightarrow O_2(a^1) + O_2$	$4.3 \cdot 10^{-22} T^{2.4} \exp(-281/T)$	[25]
$O_2(b^1) + O_3 \rightarrow O_2 + O_2 + O$	$2.2 \cdot 10^{-11}$	[25]
$O_2^{4.5eV} + O \rightarrow O_2 + O(_1S)$	$9.0 \cdot 10^{-12}$	[25]
$O + O_3 \rightarrow O_2 + O_2(a^1)$	$1.0 \cdot 10^{-11} \exp(-2300/T)$	[25]
$O + O + CO_2 \rightarrow O_2(a^1) + CO_2$	$0.07[3.6 \cdot 10^{-34} \exp(900/T)]$	[25]
$O + O + O_2 \rightarrow O_2(a^1) + O_2$	$0.07[4.0 \cdot 10^{-33} (300/T)^{0.41}]$	[25]
$O + O + O \rightarrow O_2(a^1) + O$	$0.07[3.6 \cdot 4.0 \cdot 10^{-33} (300/T)^{0.41}]$	[25]
$O + O + CO_2 \rightarrow O_2(b^1) + CO_2$	$0.01[3.6 \cdot 10^{-34} \exp(900/T)]$	[25]
$O + O + O_2 \rightarrow O_2(b^1) + O_2$	$0.01[4.0 \cdot 10^{-33} (300/T)^{0.41}]$	[25]
$O + O + O \rightarrow O_2(b^1) + O$	$0.01[3.6 \cdot 4.0 \cdot 10^{-33} (300/T)^{0.41}]$	[25]
$O(_1D) + CO_2 \rightarrow O + CO_2$	$2.52 \cdot 10^{-10}$	[102]
$O(_1D) + CO \rightarrow CO_2$	$8.0 \cdot 10^{-11}$	[102]
$O(_1D) + O \rightarrow O + O$	$8.0 \cdot 10^{-12}$	[25]
$O(_1D) + O_2 \rightarrow O + O_2$	$6.4 \cdot 10^{-12} \exp(67/T)$	[25]
$O(_1D) + O_2 \rightarrow O + O_2(a^1)$	$1.0 \cdot 10^{-12}$	[25]
$O(_1D) + O_2 \rightarrow O + O_2(b^1)$	$2.6 \cdot 10^{-11} \exp(67/T)$	[25]
$O(_1D) + O_3 \rightarrow O_2 + O + O$	$1.2 \cdot 10^{-10}$	[25]
$O(_1D) + O_3 \rightarrow O_2 + O_2$	$1.2 \cdot 10^{-10}$	[25]
$O(_1S) + O \rightarrow O(_1D) + O$	$5.0 \cdot 10^{-11} \exp(-300/T)$	[95]
$O(_1S) + O_2 \rightarrow O(_1D) + O_2$	$1.3 \cdot 10^{-12} \exp(-850/T)$	[95]
$O(_1S) + O_2 \rightarrow O + O + O$	$3.0 \cdot 10^{-12} \exp(-850/T)$	[95]
$O(_1S) + O_2(a^1) \rightarrow O + O + O$	$3.4 \cdot 10^{-11}$	[95]
$O(_1S) + O_2(a^1) \rightarrow O(_1D) + O_2(b^1)$	$2.9 \cdot 10^{-11}$	[95]
$O(_1S) + O_3 \rightarrow O_2 + O_2$	$2.9 \cdot 10^{-10}$	[95]
$O(_1S) + O_3 \rightarrow O_2 + O + O(_1D)$	$2.9 \cdot 10^{-10}$	[95]
$CO_2 + CO_2 \rightarrow CO + O + CO_2$	$2.14 \cdot 10^{-10} (T/298)^{0.5} \exp(-52321/T)$	[55]
$CO + O + CO_2 \rightarrow CO_2 + CO_2$	Reversed	
$CO + O + CO \rightarrow CO_2 + CO$	$1.46 \cdot 10^{-34} \exp(2280/T)$	[55]
$CO_2 + CO \rightarrow CO + O + CO$	Reversed	
$CO_2 + O_2 \rightarrow CO + O + O_2$	$5.9 \cdot 7.02 \cdot 10^{-12} (T/298)^{0.5} \exp(-37527/T)$	[55]
$CO + O + O_2 \rightarrow CO_2 + O_2$	Reversed	
$CO_2 + O \rightarrow CO + O + O$	$21.0 \cdot 7.02 \cdot 10^{-12} (T/298)^{0.5} \exp(-37527/T)$	[55]

$CO + O + O \rightarrow CO_2 + O$	Reversed	
$CO_2 + O \rightarrow CO + O_2$	$2.81 \cdot 10^{-11} \exp(-26461/T)$	[55]
$CO + O_2 \rightarrow CO_2 + O$	$4.20 \cdot 10^{-12} \exp(24056/T)$	[55]
$O + O_3 \rightarrow O_2 + O_2$	$2.23 \cdot 10^{-12} (T/298)^{0.75} \exp(-1580/T)$	[55]
$O_2 + O_2 \rightarrow O + O_3$	Reversed	
$O_2 + CO_2 \rightarrow O + O + CO_2$	$2.0 \cdot 6.1 \cdot 10^{-9} (1 - \exp(-2240/T)) \exp(-59380/T)$	[25]
$O + O + CO_2 \rightarrow O_2 + CO_2$	Reversed	
$O_2 + O_2 \rightarrow O + O + O_2$	$5.9 \cdot 6.1 \cdot 10^{-9} (1 - \exp(-2240/T)) \exp(-59380/T)$	[25]
$O + O + O_2 \rightarrow O_2 + O_2$	$4.0 \cdot 10^{-33} (300/T)^{0.41}$	[25]
$O_2 + O \rightarrow O + O + O$	$21.0 \cdot 6.1 \cdot 10^{-9} (1 - \exp(-2240/T)) \exp(-59380/T)$	[25]
$O + O + O \rightarrow O_2 + O$	$3.6 \cdot 4.0 \cdot 10^{-33} (300/T)^{0.41}]$	[25]
$O_3 + O_2 \rightarrow O_2 + O + O_2$	$0.38[6.6 \cdot 10^{-10} \exp(-11600/T)]$	[25]
$O + O_2 + O_2 \rightarrow O_3 + O_2$	$7.6 \cdot 10^{-34} (300/T)^{1.9}$	[25]
$O_3 + O \rightarrow O_2 + O + O$	$6.3[6.6 \cdot 10^{-10} \exp(-11600/T) \exp(170/T)]$	[25]
$O + O_2 + O \rightarrow O_3 + O$	$min\{3.9 \cdot 10^{-33} (300/T)^{1.9}, 1.1 \cdot 10^{-34} \exp(1060/T)\}$	[25]
$O_3 + O_3 \rightarrow O_2 + O + O_3$	$7.16 \cdot 10^{-10} \exp(-11200/T)$	[55]
$O_2 + O + O_3 \rightarrow O_3 + O_3$	Reversed	

Spontaneous emission	(s^{-1})	
$O_2(a^1) \rightarrow O_2$	$2.6 \cdot 10^{-4}$	[25]
$O_2(b^1) \rightarrow O_2(a^1)$	$1.5 \cdot 10^{-3}$	[25]
$O_2(b^1) \rightarrow O_2$	$8.5 \cdot 10^{-2}$	[25]
$O_2(4.5eV) \rightarrow O_2$	11.0	[25]

Surface reactions	Recombination factor (s^{-1})	
$CO_2^+ \rightarrow CO_2$	$\gamma = 1$	
$CO^+ \rightarrow CO$	$\gamma = 1$	
$C^+ \rightarrow C$	$\gamma = 1$	
$O_4^+ \rightarrow 2\,O_2$	$\gamma = 1$	
$O_2^+ \rightarrow O_2$	$\gamma = 1$	
$O^+ \rightarrow O$	$\gamma = 1$	
$O_2(a^1) \rightarrow O_2$	$\gamma = 10^{-5}$	[25]
$O_2(b^1) \rightarrow O_2$	$\gamma = 10^{-2}$	[25]
$O(_1D) \rightarrow O$	$\gamma = 1$	
$O(_1S) \rightarrow O$	$\gamma = 1$	
$2\,O \rightarrow O_2$	$\gamma = 2.0 \cdot 10^{-4}$	[93]

Exhaust Coefficients	
$\alpha(CO_2^+) = 7.45$	$\beta(O_4^+) = 0.49$
$\alpha(CO^+) = 7.50$	$\beta(O_4^+) = 0.53$
$\alpha(C^+) = 7.53$	$\beta(O_4^+) = 0.60$
$\alpha(O_4^+) = 7.45$	$\beta(O_4^+) = 0.54$
$\alpha(O_2^+) = 7.45$	$\beta(O_2^+) = 0.54$
$\alpha(O^+) = 6.72$	$\beta(O^+) = 0.60$

1. $O_2(4.5eV)$ Generic excited state representative of $A^3\Sigma$, $C^3\Delta$, $c^1\Sigma$ states.

2. M is third body reaction partner M = O_2.

N2O plasma assisted decomposition model kinetic scheme

TABLE A.10: N_2O kinetic scheme used for plasma assisted decomposition model.

Reaction	Rate Constant 2nd order (cm^3/s) 3rd order (cm^6/s)	Reference
Electron impact		
$e + N_2O \rightarrow e + N_2O(^*v)$	Integrated	[96]
$e + N_2O \rightarrow e + N_2O^*$	Integrated	[96]
$e + N_2O \rightarrow e + e + N_2O^+$	Integrated	[96]
$e + N_2O \rightarrow e + N_2 + O(_1D)$	Integrated	[97]
$e + N_2O \rightarrow e + N_2 + O$	Integrated	[97]
$e + N_2O \rightarrow e + N + NO$	Integrated	[97]
$e + N_2 \rightarrow e + N_2(v^*)$	Integrated	[43, 89]
$e + N_2 \rightarrow e + N_2^*$	Integrated	[43, 89]
$e + N_2 \rightarrow e + N + N$	Integrated	[103]
$e + N_2 \rightarrow e + e + N_2^+$	Integrated	[43, 89]
$e + O_2 \rightarrow e + O_2(^*v)$	Integrated	[43, 94]
$e + O_2 \rightarrow e + O_2^*$	Integrated	[43, 94]
$e + O_2 \rightarrow e + O + O$	Integrated	[43, 94]
$e + O_2 \rightarrow e + O + O(_1D)$	Integrated	[43, 94]
$e + O_2 \rightarrow e + e + O_2^+$	Integrated	[43, 94]
$e + O \rightarrow e + O(_1D)$	Integrated	[43, 94]
$e + O \rightarrow e + O^*$	Integrated	[43, 94]
$e + O \rightarrow e + e + O^+$	Integrated	[43, 94]
$e + N \rightarrow e + N^*$	Integrated	[104]
$e + N \rightarrow e + e + N^+$	Integrated	[99]
$e + NO \rightarrow e + NO(^*v)$	Integrated	[105]
$e + NO \rightarrow e + NO^*$	Integrated	[105]
$e + NO \rightarrow e + e + NO^+$	Integrated	[105]
Electron-ion recombination		
$e + N_2O^+ \rightarrow N_2 + O$	$2.0 \cdot 10^{-7}(300/T_e(K))^{0.5}$	[95]
$e + N_2^+ \rightarrow N + N$	$0.50[1.8 \cdot 10^{-7}(300/T_e(K))^{0.39}$	[25]
$e + N_2^+ e \rightarrow N + N + e$	$1.0 \cdot 10^{-19}(300/T_e(K))^{4.5}$	[95]
$e + N_2^+ M \rightarrow N + N + M$	$6.0 \cdot 10^{-27}(300/T_e(K))^{1.5}$	[95]
$e + O_2^+ \rightarrow O + O$	$0.55[2.7 \cdot 10^{-7}(300/T_e(K))^{0.7}]$	[25]
$e + O_2^+ \rightarrow O + O(_1D)$	$0.4[2.7 \cdot 10^{-7}(300/T_e(K))^{0.7}]$	[25]
$e + O_2^+ + e \rightarrow O_2 + e$	$1.0 \cdot 10^{-19}(300/T_e(K))^{4.5}$	[95]
$e + O_2^+ + M \rightarrow O_2 + M$	$6.0 \cdot 10^{-27}(300/T_e(K))^{1.5}$	[95]
$e + O^+ + e \rightarrow O + e$	$1.0 \cdot 10^{-19}(300/T_e(K))^{4.5}$	[95]
$e + O^+ + M \rightarrow O + M$	$6.0 \cdot 10^{-27}(300/T_e(K))^{1.5}$	[95]
$e + N^+ + e \rightarrow N + e$	$1.0 \cdot 10^{-19}(300/T_e(K))^{4.5}$	[95]
$e + N^+ + M \rightarrow N + M$	$6.0 \cdot 10^{-27}(300/T_e(K))^{1.5}$	[95]
$e + NO^+ + e \rightarrow NO + e$	$1.0 \cdot 10^{-19}(300/T_e(K))^{4.5}$	[95]
$e + NO^+ + M \rightarrow NO + M$	$6.0 \cdot 10^{-27}(300/T_e(K))^{1.5}$	[95]

$e + NO^+ \rightarrow O + N$	$4.2 \cdot 10^{-7}(300/T_e(K))^{0.85}$	[25]
Electron attachment		
$e + N_2O \rightarrow N_2 + O^-$	Integrated	[106]
$e + NO \rightarrow NO^-$	Integrated	[105]
$e + O_2 \rightarrow O^- + O$	$1.07 \cdot 10^{-9} \exp(-6.29/T_e)$	[7]
$e + O_2 + O_2 \rightarrow O_2^- + O_2$	$1.40 \cdot 10^{-29} \left(\frac{300}{T_e(K)}\right) \exp\left(-\frac{600}{T}\right) \exp\left(\frac{700(T_e(K)-T)}{T \cdot T_e(K)}\right)$	[25]
$e + O + O_2 \rightarrow O_2^- + O$	$1.0e-31$	[25]
$e + O + O_2 \rightarrow O^- + O_2$	$1.0e-31$	[25]
Electron detachment		
$O^- + O \rightarrow O_2 + e$	$1.4 \cdot 10^{-10}$	[25]
$O^- + N \rightarrow NO + e$	$2.6 \cdot 10^{-10}$	[25]
$O^- + N_2 \rightarrow N_2O + e$	$5.0 \cdot 10^{-12}$	[25]
$O^- + N_2O \rightarrow N_2O + O + e$	$3.0 \cdot 10^{-10}$	[25]
$O_2^- + N_2 \rightarrow O_2 + N_2 + e$	$1.9 \cdot 10^{-12}(T/300)^{0.5} \exp(-4990/T)$	[25]
$O_2^- + O_2 \rightarrow O_2 + O_2 + e$	$2.7 \cdot 10^{-10}(T/300)^{0.5} \exp(-5590/T)$	[25]
$NO^- + N_2O \rightarrow N_2O + NO + e$	$4.26 \cdot 10^{-10} \exp(-1270/T)$	[25]
Metastable deactivation		
$O(_1D) + O = O + O$	$8.0 \cdot 10^{-12}$	[25]
$O(_1D) + O_2 = O + O_2$	$6.4 \cdot 10^{-12} \exp(67/T)$	[25]
$O(_1D) + N_2 = O + N_2$	$1.8 \cdot 10^{-11} \exp(107/T)$	[95]
$O(_1D) + NO = O + NO$	$4.0 \cdot 10^{-11}$	[55]
$O(_1D) + NO = O_2 + N$	$1.7 \cdot 10^{-10}$	[95]
$O(_1D) + N_2O = NO + NO$	$5.02 \cdot 10^{11}(T/298)^{1.12} \exp(105/T)$	[107]
$O(_1D) + N_2O = O_2 + N_2$	$3.81 \cdot 10^{11}(T/298)^{1.11} \exp(28.85/T)$	[108]
Associative ionization		
$N + N = N_2p + e$	$2.7 \cdot 10^{-11} \exp(-67400/T) \cdot (T \geq 4000)$	[25]
$N + O = NOp + e$	$1.6 \cdot 10^{-12} \left(\frac{T}{300}\right)^{0.5} \cdot (0.19 + 8.6T) \exp\left(-\frac{32000}{T}\right) \cdot (T \geq 4000)$	[25]
Positive ion reactions		
$N_2O^+ + NO \rightarrow NO^+ + N_2O$	$2.9 \cdot 10^{-10}$	[25]
$N_2^+ + N_2O \rightarrow N_2O^+ + N_2$	$5.0 \cdot 10^{-10}$	[95]
$N_2^+ + N_2O \rightarrow NO^+ + N + N_2$	$4.0 \cdot 10^{-10}$	[95]
$N_2^+ + O_2 \rightarrow O_2^+ + N_2$	$6.0 \cdot 10^{-11}(300/T)^{0.5}$	[25]
$N_2^+ + NO \rightarrow NO^+ + N_2$	$3.3 \cdot 10^{-10}$	[95]
$N_2^+ + O \rightarrow NO^+ + N$	$1.3 \cdot 10^{-10}(300/T)^{0.5}$	[25]
$N_2^+ + O \rightarrow O^+ + N_2$	$1.0 \cdot 10^{-11}(300/T)^{0.2}$	[95]
$N_2^+ + N \rightarrow N^+ + N_2$	$7.2 \cdot 10^{-13}(300/T)$	[95]
$O_2^+ + N_2 \rightarrow NO^+ + NO$	$1.0 \cdot 10^{-17}$	[95]
$O_2^+ + N \rightarrow NO^+ + O$	$1.2 \cdot 10^{-10}$	[95]
$O_2^+ + NO \rightarrow NO^+ + O_2$	$6.3 \cdot 10^{-10}$	[95]
$O^+ + N_2O \rightarrow NO^+ + NO$	$2.3 \cdot 10^{-10}$	[95]
$O^+ + N_2O \rightarrow N_2O^+ + O$	$2.2 \cdot 10^{-10}$	[95]
$O^+ + N_2O \rightarrow O_2^+ + N_2$	$2.0 \cdot 10^{-11}$	[95]
$O^+ + N_2 \rightarrow NO^+ + N$	$1.0 \cdot 10^{-12}[1.5 - 2.0 \cdot 10^{-3}T + 9.6 \cdot 10^{-7}T^2]$	[25]

$O^+ + O_2 \rightarrow O_2^+ + O$	$2.0 \cdot 10^{-11}(300/T)^{0.5}$	[25]
$O^+ + NO \rightarrow NO^+ + O$	$2.4 \cdot 10^{-11}$	[25]
$O^+ + NO \rightarrow O_2^+ + N$	$3.0 \cdot 10^{-12}$	[25]
$O^+ + O + M \rightarrow O_2^+ + M$	$1.0 \cdot 10^{-29}$	[25]
$O^+ + N_2 + M \rightarrow NO^+ + N + M$	$6.0 \cdot 10^{-29}(300/T)^2$	[95]
$O^+ + N + M \rightarrow NO^+ + M$	$1.0 \cdot 10^{-29}$	[95]
$N^+ + O \rightarrow O^+ + N$	$1.0 \cdot 10^{-12}$	[25]
$N^+ + O_2 \rightarrow O_2^+ + N$	$2.8 \cdot 10^{-10}$	[25]
$N^+ + O_2 \rightarrow NO^+ + O$	$2.5 \cdot 10^{-10}$	[25]
$N^+ + NO \rightarrow NO^+ + N$	$8.0 \cdot 10^{-12}$	[25]
$N^+ + NO \rightarrow N_2^+ + O$	$3.0 \cdot 10^{-12}$	[25]
$N^+ + NO \rightarrow O^+ + N_2$	$1.0 \cdot 10^{-12}$	[25]
$N^+ + O + M \rightarrow NO^+ + M$	$1.0 \cdot 10^{-29}$	[25]
$N^+ + N + M \rightarrow N_2^+ + M$	$1.0 \cdot 10^{-29}$	[95]

Negative ion reactions

$O_2^- + O \rightarrow O^- + O_2$	$3.3 \cdot 10^{-10}$	[25]
$O^- + N_2O \rightarrow NO^- + NO$	$2.0 \cdot 10^{-10}$	[25]
$NO^- + O_2 \rightarrow O_2^- + NO$	$5.0 \cdot 10^{-10}$	[25]

Ion-ion recombination

$O^- + N_2O^+ \rightarrow O + N_2O$	$2.0 \cdot 10^{-7}(300/T)^{0.5}$	[95]
$O^- + N_2^+ \rightarrow O + N_2$	$2.0 \cdot 10^{-7}(300/T)^{0.5}$	[95]
$O^- + O_2^+ \rightarrow O + O_2$	$2.0 \cdot 10^{-7}(300/T)^{0.5}$	[95]
$O^- + NO^+ \rightarrow O + NO$	$2.0 \cdot 10^{-7}(300/T)^{0.5}$	[95]
$O^- + N^+ \rightarrow O + N$	$2.0 \cdot 10^{-7}(300/T)^{0.5}$	[95]
$O^- + O^+ \rightarrow O + O$	$2.0 \cdot 10^{-7}(300/T)^{0.5}$	[95]
$O_2^- + N_2O^+ \rightarrow O_2 + N_2O$	$2.0 \cdot 10^{-7}(300/T)^{0.5}$	[95]
$O_2^- + N_2^+ \rightarrow O_2 + N_2$	$2.0 \cdot 10^{-7}(300/T)^{0.5}$	[95]
$O_2^- + O_2^+ \rightarrow O_2 + O_2$	$2.0 \cdot 10^{-7}(300/T)^{0.5}$	[95]
$O_2^- + NO^+ \rightarrow O_2 + NO$	$2.0 \cdot 10^{-7}(300/T)^{0.5}$	[95]
$O_2^- + N^+ \rightarrow O_2 + N$	$2.0 \cdot 10^{-7}(300/T)^{0.5}$	[95]
$O_2^- + O^+ \rightarrow O_2 + O$	$2.0 \cdot 10^{-7}(300/T)^{0.5}$	[95]
$NO^- + N_2O^+ \rightarrow NO + N_2O$	$2.0 \cdot 10^{-7}(300/T)^{0.5}$	[95]
$NO^- + N_2^+ \rightarrow NO + N_2$	$2.0 \cdot 10^{-7}(300/T)^{0.5}$	[95]
$NO^- + O_2^+ \rightarrow NO + O_2$	$2.0 \cdot 10^{-7}(300/T)^{0.5}$	[95]
$NO^- + NO^+ \rightarrow NO + NO$	$2.0 \cdot 10^{-7}(300/T)^{0.5}$	[95]
$NO^- + N^+ \rightarrow NO + N$	$2.0 \cdot 10^{-7}(300/T)^{0.5}$	[95]
$NO^- + O^+ \rightarrow NO + O$	$2.0 \cdot 10^{-7}(300/T)^{0.5}$	[95]
$O^- + N_2O^+ \rightarrow O + N_2 + O$	$1.0 \cdot 10^{-7}$	[95]
$O^- + N_2^+ \rightarrow O + N + N$	$1.0 \cdot 10^{-7}$	[95]
$O^- + O_2^+ \rightarrow O + O + O$	$1.0 \cdot 10^{-7}$	[95]
$O^- + NO^+ \rightarrow O + N + O$	$1.0 \cdot 10^{-7}$	[95]
$O_2^- + N_2O^+ \rightarrow O_2 + N_2 + O$	$1.0 \cdot 10^{-7}$	[95]
$O_2^- + N_2^+ \rightarrow O_2 + N + N$	$1.0 \cdot 10^{-7}$	[95]
$O_2^- + O_2^+ \rightarrow O_2 + O + O$	$1.0 \cdot 10^{-7}$	[95]
$O_2^- + NO^+ \rightarrow O_2 + N + O$	$1.0 \cdot 10^{-7}$	[95]
$NO^- + N_2O^+ \rightarrow NO + N_2 + O$	$1.0 \cdot 10^{-7}$	[95]

$NO^- + N_2^+ \rightarrow NO + N + N$	$1.0 \cdot 10^{-7}$	[95]
$NO^- + O_2^+ \rightarrow NO + O + O$	$1.0 \cdot 10^{-7}$	[95]
$NO^- + NO^+ \rightarrow NO + N + O$	$1.0 \cdot 10^{-7}$	[95]
$O^- + N_2^+ + M \rightarrow O + N_2 + M$	$2.0 \cdot 10^{-25}(300/T)^{2.5}$	[95]
$O^- + O_2^+ + M \rightarrow O + O_2 + M$	$2.0 \cdot 10^{-25}(300/T)^{2.5}$	[95]
$O^- + NO^+ + M \rightarrow O + NO + M$	$2.0 \cdot 10^{-25}(300/T)^{2.5}$	[95]
$O^- + N^+ + M \rightarrow O + N + M$	$2.0 \cdot 10^{-25}(300/T)^{2.5}$	[95]
$O^- + O^+ + M \rightarrow O + O + M$	$2.0 \cdot 10^{-25}(300/T)^{2.5}$	[95]
$O_2^- + N_2^+ + M \rightarrow O_2 + N_2 + M$	$2.0 \cdot 10^{-25}(300/T)^{2.5}$	[95]
$O_2^- + O_2^+ + M \rightarrow O_2 + O_2 + M$	$2.0 \cdot 10^{-25}(300/T)^{2.5}$	[95]
$O_2^- + NO^+ + M \rightarrow O_2 + NO + M$	$2.0 \cdot 10^{-25}(300/T)^{2.5}$	[95]
$O_2^- + N^+ + M \rightarrow O_2 + N + M$	$2.0 \cdot 10^{-25}(300/T)^{2.5}$	[95]
$O_2^- + O^+ + M \rightarrow O_2 + O + M$	$2.0 \cdot 10^{-25}(300/T)^{2.5}$	[95]
$NO^- + N_2^+ + M \rightarrow NO + N_2 + M$	$2.0 \cdot 10^{-25}(300/T)^{2.5}$	[95]
$NO^- + O_2^+ + M \rightarrow NO + O_2 + M$	$2.0 \cdot 10^{-25}(300/T)^{2.5}$	[95]
$NO^- + NO^+ + M \rightarrow NO + NO + M$	$2.0 \cdot 10^{-25}(300/T)^{2.5}$	[95]
$NO^- + N^+ + M \rightarrow NO + N + M$	$2.0 \cdot 10^{-25}(300/T)^{2.5}$	[95]
$NO^- + O^+ + M \rightarrow NO + O + M$	$2.0 \cdot 10^{-25}(300/T)^{2.5}$	[95]

Dissociation-recombination of N_2

$N_2 + N_2 \rightarrow N + N + N_2$	$5.4 \cdot 10^{-8}(1 - \exp(-3354/T)) \exp(-113200/T)$	[25]
$N_2 + O_2 \rightarrow N + N + O_2$	$5.4 \cdot 10^{-8}(1 - \exp(-3354/T)) \exp(-113200/T)$	[25]
$N_2 + NO \rightarrow N + N + NO$	$5.4 \cdot 10^{-8}(1 - \exp(-3354/T)) \exp(-113200/T)$	[25]
$N_2 + N \rightarrow N + N + N$	$6.6[5.4 \cdot 10^{-8}(1 - \exp(-3354/T)) \exp(-113200/T)]$	[25]
$N_2 + O \rightarrow N + N + O$	$6.6[5.4 \cdot 10^{-8}(1 - \exp(-3354/T)) \exp(-113200/T)]$	[25]
$N + N + N_2 \rightarrow N_2 + N_2$	$8.3 \cdot 10^{-34} \exp(500/T) \cdot (T \leq 600) \quad , 1.91 \cdot 10^{-33} \cdot (T > 600)$	[25]
$N + N + O_2 \rightarrow N_2 + O_2$	$1.8 \cdot 10^{-33} \exp(435/T)$	[25]
$N + N + NO \rightarrow N_2 + NO$	$1.8 \cdot 10^{-33} \exp(435/T)$	[25]
$N + N + N \rightarrow N_2 + N$	$3.0[1.8 \cdot 10^{-33} \exp(435/T)]$	[25]
$N + N + O \rightarrow N_2 + O$	$3.0[1.8 \cdot 10^{-33} \exp(435/T)]$	[25]

Dissociation-recombination of O_2

$O_2 + N_2 \rightarrow O + O + N_2$	$6.1 \cdot 10^{-9}(1 - \exp(-2240/T)) \exp(-59380/T)$	[25]
$O_2 + O_2 \rightarrow O + O + O_2$	$5.9[6.1 \cdot 10^{-9}(1 - \exp(-2240/T)) \exp(-59380/T)$	[25]
$O_2 + NO \rightarrow O + O + NO$	$[6.1 \cdot 10^{-9}(1 - \exp(-2240/T)) \exp(-59380/T)$	[25]
$O_2 + N \rightarrow O + O + N$	$[6.1 \cdot 10^{-9}(1 - \exp(-2240/T)) \exp(-59380/T)$	[25]
$O_2 + O \rightarrow O + O + O$	$21.0[6.1 \cdot 10^{-9}(1 - \exp(-2240/T)) \exp(-59380/T)$	[25]
$O + O + N_2 \rightarrow O_2 + N_2$	$8.3 \cdot 10^{-34} \exp\left(\frac{720}{T}\right) \cdot (T \leq 500)\,, 1.0 \cdot 10^{-33} \left(\frac{300}{T}\right)^{0.41} \cdot (T > 500)$	[25]
$O + O + O_2 \rightarrow O_2 + O_2$	$4.0 \cdot 10^{-33}(300/T)^{0.41}$	[25]
$O + O + NO \rightarrow O_2 + NO$	$0.17[4.0 \cdot 10^{-33}(300/T)^{0.41}]$	[25]
$O + O + N \rightarrow O_2 + N$	$0.8[4.0 \cdot 10^{-33}(300/T)^{0.41}]$	[25]
$O + O + O \rightarrow O_2 + O$	$3.6[4.0 \cdot 10^{-33}(300/T)^{0.41}]$	[25]

Dissociation-recombination of NO

$NO + N_2 \rightarrow N + O + N_2$	$8.7 \cdot 10^{-9} \exp(-75994/T)$	[25]
$NO + O_2 \rightarrow N + O + O_2$	$6.1 \cdot 10^{-9} \exp(-75994/T)$	[25]
$NO + NO \rightarrow N + O + NO$	$20.0[6.1 \cdot 10^{-9} \exp(-75994/T)]$	[25]
$NO + N \rightarrow N + O + N$	$20.0[6.1 \cdot 10^{-9} \exp(-75994/T)]$	[25]

$NO + O \rightarrow N + O + O$	$20.0[6.1 \cdot 10^{-9} \exp(-75994/T)]$	[25]
$N + O + N_2 \rightarrow NO + N_2$	$1.0 \cdot 10^{-32}(300/T)^{0.5}$	[25]
$N + O + O_2 \rightarrow NO + O_2$	$1.0 \cdot 10^{-32}(300/T)^{0.5}$	[25]
$N + O + NO \rightarrow NO + NO$	$1.0 \cdot 10^{-31}(300/T)$	[25]
$N + O + N \rightarrow NO + N$	$1.0 \cdot 10^{-31}(300/T)$	[25]
$N + O + O \rightarrow NO + O$	$1.0 \cdot 10^{-31}(300/T)$	[25]
Dissociation-recombination of N_2O		
$N_2O + N_2O \rightarrow N + O + N_2$	$4.0[1.2 \cdot 10^{-8}(300/T) \exp(-29000/T)]$	[25]
$N + O + N_2O \rightarrow N_2O + N_2O$	Reversed	
$N_2O + N_2 \rightarrow N + O + O_2$	$1.2 \cdot 10^{-8}(300/T) \exp(-29000/T)$	[25]
$N + O + N_2 \rightarrow N_2O + N_2$	Reversed	
$N_2O + O_2 \rightarrow N + O + NO$	$1.2 \cdot 10^{-8}(300/T) \exp(-29000/T)$	[25]
$N + O + O_2 \rightarrow N_2O + O_2$	Reversed	
$N_2O + NO \rightarrow N + O + N$	$2.0[1.2 \cdot 10^{-8}(300/T) \exp(-29000/T)]$	[25]
$N + O + NO \rightarrow N_2O + NO$	Reversed	
Gas phase reactions		
$NO + N \rightarrow O + N_2$	$1.8 \cdot 10^{-11}(T/300)^{0.5}$	[25]
$O + N_2 \rightarrow NO + N$	$3.0 \cdot 10^{-10} \exp(-38370/T)$	[25]
$NO + O \rightarrow N + O_2$	$7.5 \cdot 10^{-12}(T/300) \exp(-19500/T)$	[25]
$N + O_2 \rightarrow O + NO$	$3.2 \cdot 10^{-12}(T/300) \exp(-3150/T)$	[25]
$N_2O + O \rightarrow N_2 + O_2$	$6.13 \cdot 10^{-12} \exp(-8020/T)$	[109]
$N_2 + O_2 \rightarrow O + N_2O$	Reversed	
$N_2O + O \rightarrow NO + NO$	$1.52 \cdot 10^{-10} \exp(-13930/T)$	[109]
$NO + NO \rightarrow O + N_2O$	Reversed	
$NO + NO \rightarrow N_2 + O_2$	$5.1 \cdot 10^{-13} \exp(-33660/T)$	[25]
$N_2 + O_2 \rightarrow NO + NO$	Reversed	

Surface reactions	Recombination factor (s^{-1})	
$N_2O^+ \rightarrow N_2O$	$\gamma = 1$	
$N_2^+ \rightarrow N_2$	$\gamma = 1$	
$O_2^+ \rightarrow O_2$	$\gamma = 1$	
$NO^+ \rightarrow NO$	$\gamma = 1$	
$O^+ \rightarrow O$	$\gamma = 1$	
$N^+ \rightarrow O$	$\gamma = 1$	
$O(_1D) \rightarrow O$	$\gamma = 1$	
$2\,O \rightarrow O_2$	$\gamma = 2.0 \cdot 10^{-4}$	[93]
$2\,N \rightarrow N_2$	$\gamma = 8.0 \cdot 10^{-4}$	[93]

1. T and $T_e(K)$ are expressed both in K, T_e is expressed in eV.
2. Excited states not tracked as distinct species: electronic (*), (*v) vibrational.
3. M is third body reaction partner M = N_2, O_2.

Appendix B

Non-Equilibrium Reaction Factors

Kuznetsov model

The non equilibrium factor is expressed as

$$\Phi(T, T_v) = \frac{\prod_1^m Q_j(T)}{\prod_1^m Q_j(T_{vj})} \exp\left[-E_v^* \left(\frac{m}{\sum T_{vj}} - \frac{1}{T}\right)\right]$$

$$\begin{cases} m = 3N - 5 - \sum_j^t (d_j - 1) & \text{linear molecules} \\ m = 3N - 6 - \sum_j^t (d_j - 1) & \text{non linear molecules} \end{cases} \tag{B.1}$$

$$Q_j(T_f) = [1 - \exp(-\theta_j / T_f)]^{-d_j} \quad T_f = T \quad \text{or} \quad T_v \tag{B.2}$$

Notation:

Q_j is the vibrational partition function of the jth vibrational mode

d_j is the degeneracy of the jth mode

t is the number of degenerate modes

N is the number of atoms in a molecule

m is the number of vibrational modes including degeneracy

θ_j is the characteristic vibrational temperature of the jth mode

E_v^* is a model parameter

E_v^* is a characteristic molecular vibrational energy, that corresponds to the boundary between the region of rapid intramode VV exchange, and the region where the VT exchange and rapid intermode VV' exchange dominate; the parameter can be determined empirically or estimated theoretically. A theoretical estimation for polyatomic molecules, made by Nikitin and reported in[1, 25, 110], gives:

$$E_v^* = \bar{\theta}\left[\left(\frac{D^0\bar{\theta}}{\theta_r^2}\right)^{1/(3+s)} \cdot \exp\left(\frac{1-s}{3+s}\right) - \frac{1}{2}\right] \tag{B.3}$$

Here $\bar{\theta}$ is the characteristic vibrational temperature averaged (arithmetically) over all vibrational modes of the decomposing molecule; θ_r is the characteristic rotational temperature; s is the total number of vibrational modes in the molecule; D^0 is the dissociation energy for decomposition into given fragments. Parameters for N_2O are reported in table[B.1].

TABLE B.1: Parameters, in eV, for N_2O decomposition into N_2+O, in non equilibrium conditions.

	D^0	θ_r	θ_j	$\bar{\theta}$	E_v^*
N_2O	1.67(N_2-O)	$5.21{\cdot}10^{-5}$	θ_1 0.159 θ_2 0.073 θ_3 0.276	0.145	1.22

For N_2O dissociation ($m = 3$), the summation $\sum T_{vj}$ results $\sum T_{vj} = 2T + T_v$. In the case of dissociation of a diatomic ($m = 1$) molecule AB, by collision with a third body M, the parameter E_v^* takes into account also the anharmonicity effects, and it is determined as follow:

$$E_v^* = n^*\theta, \quad n^* = \frac{1}{2\chi_e}(1 - y_n^*) \tag{B.4}$$

The value of the quantity y_n^* is determined from the transcendental equation, to be solved each time step:

$$\begin{aligned}
&\exp\left[-0.6\sqrt{\pi}(1-y_n^*)\chi_0^{3/2}\right] - \frac{1}{4\pi^2\lambda^2\chi_{AB}}\,\frac{\mu}{M_R}\chi_0^3(3-z)z = 0 \\
&z = \exp\left(-\frac{2}{3}\chi_0^3\, y_n^*\right), \quad \chi_0 = \left(\frac{\pi^2\nu_0^2 M_R}{2\alpha k_b T}\right)^{1/3}, \quad \lambda^2 = \frac{1}{2}\,\frac{m_A^2 + m_B^2}{(m_A+m_B)^2} \\
&M_R = \frac{m_M(m_A+m_B)}{m_M+m_A+m_B}, \quad \mu = \frac{m_A\, m_B}{m_A+m_B}
\end{aligned} \tag{B.5}$$

Notation:

θ is the characteristic vibrational temperature of the mode

n^* quantum number corresponding to the E_v^* energy level

χ_e anharmonicity of the diatomic molecule

ν_0 fundamental vibrational frequency of the molecule

ν_n n-level vibrational frequency of the molecule, in the Morse potential approximation

y_n fundamental to n-level vibrational frequency ratio ν_n/ν_0

y_n^* critical y_n at level n^*

m_A, m_B, m_M masses of atoms comprising a molecule AB and of a particle M

μ reduced mass of the molecule AB system

M_R reduced mass of the molecule AB + M colliding system

χ_0 adiabaticity parameter

α Born-Mayer inverse range of interaction

χ_{AB} molar fraction of dissociating AB molecules in the medium

The value of χ_{AB} can range from a maximum of 1 to a minimum accepted value of $\chi_{AB}(min)$; below this value, no modification of the thermal rate is considered for the molecule AB. The minimum value is obtained setting $y_n^* = 1$ in the transcendental equation(B.5):

$$[\chi_{AB}]_{min} = \frac{1}{4\pi^2\lambda^2}\frac{\mu}{M_R}\chi_0^3(3 - z(1))z(1) \tag{B.6}$$

The effect of the Born-Mayer potential parameter α, on the non equilibrium factor $\Phi((T, T_v)$ is small[1]. In the absence of the appropriate data, it can be assumed a value of $\alpha = 3.2\mathring{A}^{-1}$ for all diatomic molecules.

Alpha - model

The model of the efficiency of vibrational energy utilization, addresses bimolecular chemical reactions in thermal non equilibrium; it is based on the concept of decrease in the reaction threshold when a reactant possesses an excess vibrational energy. The vibrational energy E_v of the reactant, reduces the reaction threshold (i.e. activation energy E_a), by a quantity αE_v. The factor α is independent of E_v and is called the coefficient of utilization of vibrational energy in overcoming the reaction activation barrier[1, 48].

Under the assumption of harmonic approximation with $T_v \geq T$ and $0 < \alpha < 1$, the non equilibrium factor $\Phi(T, T_v)$ for diatomic molecules, in the case of $T_v \leq \theta$ is:

$$\Phi(T,T_v)=\frac{1-\exp(\theta/T_v)}{1-\exp(\theta/T)}\cdot\frac{\frac{\exp\left(-\frac{E_a}{\alpha T_v}\right)-\exp\left(-\frac{E_a}{T}\right)}{\exp\left(\frac{\alpha\theta}{T}-\frac{\theta}{T_v}\right)-1}+\frac{\exp\left(-\frac{E_a}{\alpha T_v}\right)}{1-\exp\left(-\frac{\theta}{T_v}\right)}}{\frac{\exp\left(-\frac{E_a}{T}\right)-\exp\left(-\frac{E_a}{\alpha T}\right)}{1-\exp\left[-\frac{(1-\alpha)\theta}{T}\right]}+\frac{\exp\left(-\frac{E_a}{\alpha T}\right)}{1-\exp\left(-\frac{\theta}{T}\right)}} \tag{B.7}$$

The non equilibrium factor $\Phi(T,T_v)$ for diatomic molecules, in the case of $T_v > \theta$, and for polyatomic molecules, in general, is:

$$\Phi(T,T_v)=\frac{1-\alpha}{\frac{\alpha T_v}{T}-1}\cdot\frac{\frac{\alpha T_v}{T}\exp\left(-\frac{E_a}{\alpha T_v}\right)-\exp\left(-\frac{E_a}{T}\right)}{\exp\left(-\frac{E_a}{T}\right)-\alpha\cdot\exp\left(-\frac{E_a}{\alpha T}\right)} \tag{B.8}$$

Bibliography

[1] G G Chernyi, S A Losev, S O Macheret, and B V Potapkin. *Physical and Chemical Processes in Gas Dynamics: Cross sections and rate constants. Volume I*, volume 1. AIAA, 2002.

[2] R. Winglee, T. Ziemba, L. Giersch, J. Prager, J. Carscadden, and B.R. Roberson. Simulation and laboratory validation of magnetic nozzle effects for high power helicon thruster. *Physics of Plasmas*, 14(6):063501–14, June 2007.

[3] C. Charles, R.W. Boswell, R. Lane, and P. MacLellan. An experimental investigation of alternative propellants for the helicon double layer thruster. *Journal of Physics D: Applied Physics*, 41:175213 (6pp), 2008.

[4] D. Pavarin, F. Ferri, and M. Manente. Helicon plasma hydrazine.combined-micro. In *XX AIAA Congress*, Milan, Italy, June 29 - July 3 2009.

[5] K Takahashi, T Lafleur, C Charles, P Alexander, RW Boswell, M Perren, R Laine, S Pottinger, V Lappas, T Harle, et al. Direct thrust measurement of a permanent magnet helicon double layer thruster. *Applied Physics Letters*, 98(14):141503, 2011.

[6] Chloe Berenguer and Konstantinos Katsonis. Global modeling of CO_2 discharges with aerospace applications. *Advances in Aerospace Engineering*, 2014, 2014.

[7] M A Lieberman and A J Lichtenberg. *Principles of plasma discharges and materials processing*. John Wiley & Sons, 2005.

[8] C Lee and M A Lieberman. Global model of Ar, O_2, Cl_2, and Ar/O_2 high-density plasma discharges. *Journal of Vacuum Science & Technology A: Vacuum, Surfaces, and Films*, 13(2):368–380, 1995.

[9] T De los Arcos, C Domingo, VJ Herrero, MM Sanz, Astrid Schulz, and I Tanarro. Diagnostics and kinetic modeling of a hollow cathode N_2O discharge. *The Journal of Physical Chemistry A*, 102(31):6282–6291, 1998.

[10] Y Ikeda, JP Verboncoeur, PJ Christenson, and CK Birdsall. Global modeling of a dielectric barrier discharge in Ne-Xe mixtures for an alternating current plasma display panel. *Journal of applied physics*, 86(5):2431–2441, 1999.

[11] F Bosi, G Parissenti, M Pessana, and D Pavarin. Modelling of plasma-chemical propellant interaction in electrodeless helicon plasma thruster. In *Proceedings of 5th Eucass - European Conference for Aerospace Sciences - Munich, Germany, 2013*, July 2013.

[12] D Steitz. Nasa goes green: Nasa selects green propellant technology demonstration mission, http://www.nasa.gov/home/hqnews/2012/aug/hq_12-281_green_propellants.html.

[13] Vadim Zakirov, Martin Sweeting, Timothy Lawrence, and Jerry Sellers. Nitrous oxide as a rocket propellant. *Acta Astronautica*, 48(5):353–362, 2001.

[14] Pratik Saripalli and Raymond J Sedwick. Development of a green propellant station-keeping thruster using a dielectric barrier discharge.

[15] Andrea Lucca Fabris. Experimental characterization of plasma sources for space propulsion. Master's thesis, University of Padova, 2014.

[16] S R Turns et al. *An introduction to combustion*, volume 287. McGraw-hill New York, 1996.

[17] Franco Bosi. Analisys of N_2O plasma induced decomposition. Master's thesis, University of Padova, October 2011.

[18] Alexander Fridman. *Plasma chemistry*. Cambridge University Press, 2008.

[19] T Hori, M Kogano, M D Bowden, K Uchino, and K Muraoka. A study of electron energy distributions in an inductively coupled plasma by laser thomson scattering. *Journal of applied physics*, 83(4):1909–1916, 1998.

[20] V A Godyak. *Soviet radio frequency discharge research*. Delphic Associates Falls Church, VA, 1986.

[21] AV Phelps. The diffusion of charged particles in collisional plasmas: free and ambipolar diffusion at low and moderate pressures. *Journal of Research of the National Institute of Standards and Technol*, pages 407–431, 1990.

[22] E Kawamura, AJ Lichtenberg, and MA Lieberman. Two-dimensional particle-in-cell simulations of transport in a magnetized electronegative plasma. *Journal of Applied Physics*, 108(10):103305, 2010.

[23] G Leray, P Chabert, AJ Lichtenberg, and MA Lieberman. Fluid model of an electronegative discharge with magnetized electrons and unmagnetized ions. *Journal of Physics D: Applied Physics*, 42(19):194020, 2009.

[24] François Vidal, Tudor Wyatt Johnston, Joëlle Margot, Mohamed Chaker, and Olivier Pauna. Diffusion modeling of an hf argon plasma discharge in a magnetic field. *Plasma Science, IEEE Transactions on*, 27(3):727–745, 1999.

[25] M Capitelli, C M Ferreira, A I Osipov, and F Gordiets, Boris. *Plasma kinetics in atmospheric gases*. Springer, 2000.

[26] P J Chantry. A simple formula for diffusion calculations involving wall reflection and low density. *Journal of applied physics*, 62(4):1141–1148, 1987.

[27] Bruce E Poling, John M Prausnitz, John P O'connell, et al. *The properties of gases and liquids*, volume 5. McGraw-Hill New York, 2001.

[28] D. Pavarin, F. Ferri, M. Manente, D. Curreli, D. Melazzi, D. Rondini, and A. Cardinali. Development of plasma codes for the design of mini-helicon thrusters. In *Proceedings of the 32nd International Electric Propulsion Conference*, page 240, Wiesbaden, Germany, 2011.

[29] Andrea L. Fabris, Chris. V. Young, Marco Manente, Daniele Pavarin, and Mark A. Cappelli. Ion velocimetry measurements and particle-in-cell simulation of a cylindrical cusped plasma accelerator. *Plasma Science, IEEE Transactions on*, 43(1):54–63, Jan 2015.

[30] C Geuzaine and J Fçois Remacle. Gmsh: A $3d$ finite element mesh generator with built-in pre-and post-processing facilities. *International Journal for Numerical Methods in Engineering*, 79(11):1309–1331, 2009.

[31] C. Geuzaine. Getdp: a general finite-element solver for the de rham complex. In *PAMM Volume 7 Issue 1. Special Issue: Sixth International Congress on Industrial Applied Mathematics (ICIAM07) and GAMM Annual Meeting, Zürich 2007*, volume 7, pages 1010603–1010604. Wiley, 2008.

[32] P. Dular, C. Geuzaine, F. Henrotte, and W. Legros. A general environment for the treatment of discrete problems and its application to the finite element method. *IEEE Transactions on Magnetics*, 34(5):3395–3398, sep 1998.

[33] M Manente, F Trezzolani, A Lucca Fabris, D Melazzi, F Bosi, K Katsonis, and D Pavarin. Thruster trade off analysis report ($tn3$). Technical report, ESA, 2013.

[34] Daniele Pavarin, Fernando Ferri, M Manente, D Curreli, Y Guclu, D Melazzi, D Rondini, S Suman, J Carlsson, Cristina Bramanti, et al. Design of 50 W helicon plasma thruster. In *31st Int. Electric Propulsion Conf., Ann Arbor, MI*, pages 2009–205, 2009.

[35] F Trezzolani, A Lucca Fabris, D Pavarin, A Selmo, and M Manente. Low power radio-frequency plasma thruster development and testing. In *Proceedings of 33nd International Electric Propulsion Conference, Washington, D.C. USA*, October 2013. IEPC-2013-153.

[36] V Vahedi and M Surendra. A monte carlo collision model for the particle-in-cell method: applications to argon and oxygen discharges. *Computer Physics Communications*, 87(1):179–198, 1995.

[37] T Lafleur, C Charles, and RW Boswell. Characterization of a helicon plasma source in low diverging magnetic fields. *Journal of Physics D: Applied Physics*, 44(5):055202, 2011.

[38] Francis F Chen. Performance of a permanent-magnet helicon source at 27 and 13 mhz. *Physics of Plasmas (1994-present)*, 19(9):093509, 2012.

[39] V Kaeppelin, M Carrere, and JB Faure. Different operational regimes in a helicon plasma source. *Review of scientific instruments*, 72(12):4377–4382, 2001.

[40] Shane M Tysk, C Mark Denning, John E Scharer, and Kamran Akhtar. Optical, wave measurements, and modeling of helicon plasmas for a wide range of magnetic fields. *Physics of Plasmas (1994-present)*, 11(3):878–887, 2004.

[41] Arnab Rai Choudhuri. *The physics of fluids and plasmas: an introduction for astrophysicists*. Cambridge University Press, 1998.

[42] S Pancheshnyi, B Eismann, G J M Hagelaar, and L C Pitchford. Computer code *zdplaskin*, LAPLACE, CNRS-UPS-INP, Toulouse, France, 2008.

[43] *lxcat* - plasma data exchange project, http://nl.lxcat.net/home/, LXcat.

[44] A Flitti and S Pancheshnyi. Gas heating in fast pulsed discharges in N_2-O_2 mixtures. *The European Physical Journal Applied Physics*, 45(02):21001, 2009.

[45] RE Beverly III. Ion aging effects on the dissociative-attachment instability in CO_2 lasers. *Optical and quantum electronics*, 14(6):501–513, 1982.

[46] Hirokazu Hokazono and Haruo Fujimoto. Theoretical analysis of the CO_2 molecule decomposition and contaminants yield in transversely excited atmospheric CO_2 laser discharge. *Journal of applied physics*, 62(5):1585–1594, 1987.

[47] Thomas G Beuthe and Jen-Shih Chang. Chemical kinetic modelling of non-equilibrium Ar-CO_2 thermal plasmas. *Japanese Journal of applied physics*, 36(7S):4997, 1997.

[48] VD Rusanov, AA Fridman, and GV Sholin. The physics of a chemically active plasma with nonequilibrium vibrational excitation of molecules. *Soviet Physics Uspekhi*, 24(6):447, 1981.

[49] Tomáš Kozák and Annemie Bogaerts. Splitting of CO_2 by vibrational excitation in non-equilibrium plasmas: a reaction kinetics model. *Plasma Sources Science and Technology*, 23(4):045004, 2014.

[50] Robby Aerts, Tom Martens, and Annemie Bogaerts. Influence of vibrational states on CO_2 splitting by dielectric barrier discharges. *The Journal of Physical Chemistry C*, 116(44):23257–23273, 2012.

[51] JJ Lowke, AV Phelps, and BW Irwin. Predicted electron transport coefficients and operating characteristics of CO_2-N_2-He laser mixtures. *Journal of Applied Physics*, 44(10):4664–4671, 1973.

[52] Weihong Liu and GA Victor. Electron energy deposition in carbon monoxide gas. *The Astrophysical Journal*, 435:909–919, 1994.

[53] R Locht and M Davister. The dissociative electroionization of carbon dioxide by low-energy electron impact. the C^+, O^+ and CO dissociation channels. *International journal of mass spectrometry and ion processes*, 144(1):105–129, 1995.

[54] Yukikazu Itikawa. Cross sections for electron collisions with carbon dioxide. *Journal of Physical and Chemical Reference Data*, 31(3):749–768, 2002.

[55] NIST. Nist chemical kinetics database, http://kinetics.nist.gov/kinetics/index.jsp.

[56] Sanford Gordon and Bonnie J McBride. *Computer program for calculation of complex chemical equilibrium compositions and applications*. National Aeronautics and Space Administration, Office of Management, Scientific and Technical Information Program, 1996.

[57] D Pavarin et al. Thruster development set-up for the helicon plasma hydrazine combined micro research project. In *Proceedings of 32nd International Electric Propulsion Conference, Wiesbaden, Germany*, September 2011. IEPC-2011-241.

[58] O Tudisco, A Lucca Fabris, C Falcetta, L Accatino, R De Angelis, M Manente, F Ferri, M Florean, C Neri, C Mazzotta, et al. A microwave interferometer for small and tenuous plasma density measurements. *Review of Scientific Instruments*, 84(3):033505, 2013.

[59] NIST. Nist atomic spectra database, http://www.nist.gov/pml/data/asd.cfm.

[60] John B Boffard, RO Jung, Chun C Lin, LE Aneskavich, and AE Wendt. Argon 420.1–419.8 nm emission line ratio for measuring plasma effective electron temperatures. *Journal of Physics D: Applied Physics*, 45(4):045201, 2012.

[61] H J Kunze. *Introduction to plasma spectroscopy*, volume 56. Springer, 2009.

[62] Sergey G Belostotskiy, Tola Ouk, Vincent M Donnelly, Demetre J Economou, and Nader Sadeghi. Gas temperature and electron density profiles in an argon dc microdischarge measured by optical emission spectroscopy. *Journal of applied physics*, 107(5):053305, 2010.

[63] Muyang Qian, Chunsheng Ren, Dezhen Wang, Jialiang Zhang, and Guodong Wei. Stark broadening measurement of the electron density in an atmospheric pressure argon plasma jet with double-power electrodes. *Journal of Applied Physics*, 107(6):063303, 2010.

[64] Reginald William Blake Pearse, Alfred Gordon Gaydon, Reginald William Blake Pearse, and Alfred Gordon Gaydon. *The identification of molecular spectra*, volume 297. Chapman and Hall London, 1976.

[65] Joseph M Ajello. Emission cross sections of CO_2 by electron impact in the interval 1260–4500 å. ii. *The Journal of Chemical Physics*, 55(7):3169–3177, 1971.

[66] Fabienne Poncin-Epaillard and Mohammed Aouinti. Characterization of CO_2 plasma and interactions with polypropylene film. *Plasmas and polymers*, 7(1):1–17, 2002.

[67] Santolo De Benedictis, Riccardo D'Agostino, and Francesco Cramarossa. Spectroscopic analysis of the vibrational distributions in dissociative CO-He rf discharges. *Chemical Physics*, 71(2):247–256, 1982.

[68] GW Fox, OS Duffendack, and EF Barker. The spectrum of CO_2. *Proceedings of the National Academy of Sciences of the United States of America*, 13(5):302, 1927.

[69] Paul H Krupenie. The band spectrum of carbon monoxide. Technical report, DTIC Document, 1966.

[70] Seiji Tsurubuchi and Tsuruji Iwai. Simultaneous ionization and excitation of CO_2 by electron-impact. *Journal of the Physical Society of Japan*, 37(4):1077–1081, 1974.

[71] Timothy J Lawrence, Martin Sweeting, Malcolm Paul, JJ Sellers, JR LeDuc, JB Malak, GG Spanjers, RA Spores, and J Schilling. *Performance testing of a resistojet thruster for small satellite applications*. Defense Technical Information Center, 1998.

[72] Vadim Zakirov, Martin Sweeting, and Timothy Lawrence. An update on surrey nitrous oxide catalytic decomposition research. 2001.

[73] K Krawczyk and M Wieczorkowski. Studies of nitrous oxide conversion in gliding arc discharges. In *HAKONE 8: International Symposium on High Pressure, Low Temperature Plasma Chemistry. Proceedings. Vol. 1 and 2*, 2002.

[74] T Nunnally, Kirill Gutsol, Alexander Rabinovich, Alexander Fridman, A Gutsol, and A Kemoun. Dissociation of CO_2 in a low current gliding arc plasmatron. *Journal of Physics D: Applied Physics*, 44(27):274009, 2011.

[75] Dipl Physiker Georg Rollmann. Calculation of correction factors for variable area flow meters at deviating working conditions.

[76] David Staack, Bakhtier Farouk, Alexander F Gutsol, and Alexander A Fridman. Spectroscopic studies and rotational and vibrational temperature measurements of atmospheric pressure normal glow plasma discharges in air. *Plasma sources science and technology*, 15(4):818, 2006.

[77] Laurence S Rothman, CP Rinsland, A Goldman, ST Massie, DP Edwards, JM Flaud, A Perrin, C Camy-Peyret, V Dana, J-Y Mandin, et al. The hitran molecular spectroscopic database and hawks (hitran atmospheric workstation): 1996 edition. *Journal of Quantitative Spectroscopy and Radiative Transfer*, 60(5):665–710, 1998.

[78] D G Goodwin, H K Moffat, and R L Speth. Cantera: An object- oriented software toolkit for chemical kinetics, thermodynamics, and transport processes.

[79] A Yanguas-Gil, J Cotrino, and AR González-Elipe. Global model of a low pressure ecr microwave plasma applied to the pecvd of SiO_2 thin films. *Journal of Physics D: Applied Physics*, 40(11):3411, 2007.

[80] K Hassouni, A Gicquel, M Capitelli, and J Loureiro. Chemical kinetics and energy transfer in moderate pressure H_2 plasmas used in diamond mpacvd processes. *Plasma Sources Science and Technology*, 8(3):494, 1999.

[81] Sang Ki Nam and John P Verboncoeur. Global model for high power microwave breakdown at high pressure. In *IEEE International Power Modulators and High Voltage Conference, Proceedings of the 2008*, pages 564–566. IEEE, 2008.

[82] Carl D Scott, Samir Farhat, Alix Gicquel, and Khaled Hassouni. Determining electron temperature and density in a hydrogen microwave plasma. *Journal of thermophysics and heat transfer*, 10(3):426–435, 1996.

[83] Marek A Wojtowicz, Francis P Miknis, RW Grimes, Wayne W Smith, and Michael A Serio. Control of nitric oxide, nitrous oxide, and ammonia emissions using microwave plasmas. *Journal of Hazardous Materials*, 74(1):81–89, 2000.

[84] Krzysztof Krawczyk, Michal Drozdowski, and Katarzyna Naperty. Nitrous oxide processing by a combination of gliding and microwave discharges. *Catalysis today*, 119(1):239–242, 2007.

[85] M Jasinski, D Czylkowski, Z Zakrzewski, and J Mizeraczyk. Treatment of N_2O in pulsed microwave torch discharge. *Czechoslovak Journal of Physics*, 54(3):C859–C865, 2004.

[86] AS Biryukov, A Yu Volkov, AI Demin, EM Kudryavtsev, Yu A Kulagin, NN Sobolev, and LA Shelepin. Investigation of a gas-dynamic N_2O laser. *Zh. Eksp. Tekh. Fiz*, 688:1664, 1975.

[87] John D Anderson Jr. Modern compressible flow with historical. *Perspective*, 1982.

[88] Takashi Kimura and Hiroki Kasugai. Properties of inductively coupled rf Ar/H_2 plasmas: Experiment and global model. *Journal of Applied Physics*, 107(8):083308, 2010.

[89] L Pitchford, G J M Hagelaar, S Pancheshnyi, M C Bordage, L L Alves, C M Ferreira, S F Biagi, Y Itikawa, and A V Phelps. Comparisons of sets of electron-neutral scattering cross sections and calculated swarm parameters in N_2 and H_2. In *APS Meeting Abstracts*, volume 1, page 1087, 2012.

[90] Ramesh A Arakoni, Ananth N Bhoj, and Mark J Kushner. H_2 generation in Ar/NH_3 microdischarges. *Journal of Physics D: Applied Physics*, 40(8):2476, 2007.

[91] Isabel Méndez, Francisco J Gordillo-Vázquez, Víctor J Herrero, and Isabel Tanarro. Atom and ion chemistry in low pressure hydrogen dc plasmas. *The Journal of Physical Chemistry A*, 110(18):6060–6066, 2006.

[92] B F Gordiets, C M Ferreira, V L Guerra, J M Loureiro, J Nahorny, D Pagnon, M Touzeau, and M Vialle. Kinetic model of a low-pressure N_2-O_2 flowing glow discharge. *Plasma Science, IEEE Transactions on*, 23(4):750–768, 1995.

[93] D A Shutov, S Y Kang, K H Baek, K S Suh, and K H Kwon. Inductively-coupled nitrous-oxide plasma etching of parylene-c films. *Journal of the Korean Physical Society*, 55(5):1836–1840, 2009.

[94] L Pitchford, M C Bordage, G J M Hagelaar, A Pancheshnyi, and A V Phelps. Comparisons of sets of electron-neutral scattering cross sections and calculated swarm parameters in O_2. In *APS Meeting Abstracts*, volume 1, page 1088, 2012.

[95] IA Kossyi, A Yu Kostinsky, AA Matveyev, and VP Silakov. Kinetic scheme of the non-equilibrium discharge in nitrogen-oxygen mixtures. *Plasma Sources Science and Technology*, 1(3):207, 1992.

[96] CNEP. Centre for non-equilibrium processes.

[97] L Date, K Radouane, B Despax, M Yousfi, H Caquineau, and A Hennad. Analysis of the N_2O dissociation in a rf discharge reactor. *Journal of Physics D: Applied Physics*, 32(13):1478, 1999.

[98] A.V. Phelps. Phelps *a.v.* compilation of atomic and molecular data, http://jilawww.colorado.edu/ avp/.

[99] Morgan. database, http://www.lxcat.net.

[100] D McElroy, C Walsh, AJ Markwick, MA Cordiner, K Smith, and TJ Millar. The *umist* database for astrochemistry 2012. *Astronomy & Astrophysics*, 550:A36, 2013.

[101] Mahsa Setareh, Morteza Farnia, Ali Maghari, and Annemie Bogaerts. CF_4 decomposition in a low-pressure icp: influence of applied power and O_2 content. *Journal of Physics D: Applied Physics*, 47(35):355205, 2014.

[102] J C Tully. Reactions of $O(_1D)$ with atmospheric molecules. *The Journal of Chemical Physics*, 62(5):1893–1898, 1975.

[103] Yukikazu Itikawa. Cross sections for electron collisions with nitrogen molecules. *Journal of Physical and Chemical Reference Data*, 35(1):31–53, 2006.

[104] KA Berrington, PG Burke, and WD Robb. The scattering of electrons by atomic nitrogen. *Journal of Physics B: Atomic and molecular physics*, 8(15):2500, 1975.

[105] Makoto Hayashi. Electron collision cross-sections for molecules determined from beam and swarm data. In *Swarm Studies and Inelastic Electron-Molecule Collisions*, pages 167–187. Springer, 1987.

[106] PJ Chantry. Temperature dependence of dissociative attachment in N_2O. *The Journal of Chemical Physics*, 51(8):3369–3379, 1969.

[107] Miguel Gonzalez, R Sayos, and Rosendo Valero. Ab initio and kinetics study of the ground ^{1}a" potential energy surface of the $O(_1D)+N_2O \rightarrow 2\,NO$, $N_2+O_2(a^1\Delta_g)$ reactions. *Chemical Physics Letters*, 355:123–132, 2002.

[108] Miguel Gonzalez, Rosendo Valero, Josep Maria Anglada, and R Sayos. Ab initio 1a' ground potential energy surface and transition state theory kinetics study of the $O(_1D) + N_2O \rightarrow 2\,NO$, $N_2 + O_2(a^1\Delta_g)$ reactions. *The Journal of Chemical Physics*, 115(15):7015–7031, 2001.

[109] Nancy E Meagher and William R Anderson. Kinetics of the $O(_3P)^+N_2O$ reaction. 2. interpretation and recommended rate coefficients. *The Journal of Physical Chemistry A*, 104(25):6013–6031, 2000.

[110] S Losev, A Sergievskaya, A Starik, and N Titova. Modeling of thermal nonequilibrium multicomponent kinetics in gas dynamics and combustion. *AIAA Paper*, (97-2532), 1997.